SÃO PAULO STATE UNIVERSITY - UNESP

SCHOOL OF ENGINEERING

CAMPUS AT ILHA SOLTEIRA

ELÓY ESTEVES GASPARIN

SENSITIVITY ANALYSIS AND OPTIMIZATION OF CENTRIFUGAL COMPRESSORS TRAIN WORKING WITH SUPERCRITICAL CO_2

Ilha Solteira

2023

ELÓY ESTEVES GASPARIN

SENSITIVITY ANALYSIS AND OPTIMIZATION OF CENTRIFUGAL COMPRESSORS TRAIN WORKING WITH SUPERCRITICAL CO_2

Thesis presented to the School of Engineering at Ilha Solteira – UNESP as part of the requirements for obtaining the title of Doctor in Mechanical Engineering. Area: Thermal Sciences.

Prof. Dr. Leandro Oliveira Salviano
Advisor

Ilha Solteira

2023

FICHA CATALOGRÁFICA
Desenvolvido pelo Serviço Técnico de Biblioteca e Documentação

UNIVERSIDADE ESTADUAL PAULISTA

Câmpus de Ilha Solteira

CERTIFICADO DE APROVAÇÃO

TÍTULO DA TESE: SENSITIVITY ANALYSIS AND OPTIMIZATION OF CENTRIFUGAL COMPRESSOR TRAIN WORKING WITH SUPERCRITICAL CO2
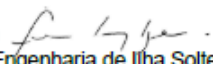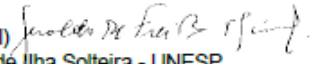
AUTOR: ELÓY ESTEVES GASPARIN
ORIENTADOR: LEANDRO OLIVEIRA SALVIANO
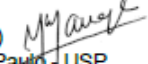
Aprovado como parte das exigências para obtenção do Título de Doutor em Engenharia Mecânica, área: Ciências Térmicas pela Comissão Examinadora:

Prof. Dr. LEANDRO OLIVEIRA SALVIANO (Participaçao Presencial)
Departamento de Engenharia Mecanica / Faculdade de Engenharia de Ilha Solteira - UNESP

Prof. Dr. JOSE LUIZ GASCHE (Participaçao Presencial)
Departamento de Engenharia Mecânica / Faculdade de Engenharia de Ilha Solteira - UNESP

Prof. Dr. GERALDO DE FREITAS MACIEL (Participaçao Virtual)
Departamento de Engenharia Civil / Faculdade de Engenharia de Ilha Solteira - UNESP

Prof. Dr. JURANDIR ITIZO YANAGIHARA (Participaçao Virtual)
Departamento de Engenharia Mecânica / Universidade de São Paulo - USP

Prof. Dr. EMÍLIO CARLOS NELLI SILVA (Participaçao Virtual)
Departamento de Engenharia Mecatrônica e Sistemas Mecânicos / Universidade de São Paulo - USP

Ilha Solteira, 16 de junho de 2023

Faculdade de Engenharia - Câmpus de Ilha Solteira -
Avenida Brasil, 56, 15385000, Ilha Solteira - São Paulo
www.ppgem.feis.unesp.brCNPJ: 48.031.918/0015-20.

ACKNOWLEDGMENTS

"Normal people… believe that if it ain't broke, don't fix it. Engineers believe that if it ain't broke, it doesn't have enough features yet".

Scott Adams

RESUMO

A crescente importância da indústria de captura, utilização e armazenamento de carbono (CCUS) devido ao aquecimento global tem demandado novas tecnologias de equipamentos. Entre os mais relevantes, nota-se o ciclo de potência de Brayton que reporta aumento na eficiência térmica de seu sistema ao utilizar o CO_2 em estado supercrítico devido ao menor trabalho de compressão quando comparado ao ar. Além desse, sistemas de armazenamento de energia que utilizavam ar comprimido também demonstraram melhora em seu desempenho ao trabalhar com CO_2. Sendo assim, a tecnologia de CCUS com maior viabilidade econômica devido ao seu produto final de alto valor agregado é o processo conhecido como *Enhanced Oil Recovery* (EOR), que utiliza um trem de compressores centrífugos para realizar o armazenamento de CO_2 supercrítico em poços de extração de petróleo, e que foi objeto de estudo do presente trabalho. Normalmente, a abordagem utilizada em um projeto de sistema de compressão é simplesmente investigada por aspectos termodinâmicos, sem considerar fenômenos fluidodinâmicos que podem inviabilizar o sistema como um todo. Portanto, a metodologia desenvolvida nesta tese é composta por um modelo de compressor centrífugo de CO_2 supercrítico e difusor sem palhetas unidimensional (1D), capaz de prever alguns aspectos do escoamento do fluido que não são modelados por meio de análise termodinâmica direta, seguido por uma Análise de Sensibilidade (SA) e estratégia de otimização. Posteriormente, a modelagem individual de dois compressores utilizando *Computational Fluid Dynamics* (CFD) fez-se necessária para corroboração dos resultados anteriores e para entregar melhorias adicionais aos equipamentos a partir da meta-modelagem por superfície de resposta (RS) destes modelos computacionalmente custosos e realização de otimização indireta. Associada a estratégia de otimização, uma restrição chamada *Gas Behaviour Margin* (GBM) é proposta para evitar grandes variações das propriedades termodinâmicas no processo de compressão próximo à linha de *Widom*, o que pode dificultar a convergência do modelo numérico (por CFD) ou ainda causar danos ao equipamento durante seu processo de operação. Os principais resultados da obtidos a partir da metodologia descrita neste trabalho mostram que o trem de compressores centrífugos com quatro estágios considerado no processo de otimização teve sua potência total reduzida em 14,09% quando comparado à configuração inicial, e garantindo uma configuração de compressores viável, já que as restrições: Margem de Aceleração para Condensação (AMC), GBM e o número de Mach na garganta foram atendidas.

Além disso, a solução do modelo CFD para o quarto compressor demonstrou boa concordância com a modelagem 1D e dados experimentais, corroborando a validade e robustez da metodologia aqui desenvolvida. Além disso, esta abordagem é considerada como uma maneira rápida e de baixo custo para obter uma geometria preliminar para sistemas de trem de compressores centrífugos. Finalmente, os modelos CFD do primeiro e quarto estágios de compressão foram submetidos a estratégia de SA e otimização, aumentando ainda mais a eficiência politrópica destes dois estágios, essa modelagem permitiu a análise fenomenológica baseada em variação entrópica que foi conduzida para o processo de avaliação fluidodinâmica do escoamento dentro dos compressores centrífugos A estratégia aqui adotada pode ser aplicada a outros modelos de CFD considerados grandes e altamente dimensionais para reduzir o custo computacional do procedimento de otimização e acelerar a análise fenomenológica do escoamento.

Palavras-chave: sistema de compressão; otimização; margem de comportamento gasoso; captura e armazenamento de carbono; compressor centrífugo s-CO2; análise de sensibilidade.

ABSTRACT

The rising importance of carbon capture, utilization and storage (CCUS) industry due to global warming has increased the development of new technologies. Among the most relevant, note the Brayton power cycle, which reported an increase in the thermal efficiency of its system when using CO_2 in a supercritical state due to the lower compression work when compared to air. Furthermore, energy storage systems that utilized compressed air also improved their performance when working with CO_2. Therefore, the CCUS technology with greater economic viability due to its final product with high added value is the process known as Enhanced Oil Recovery (EOR), which uses a train of centrifugal compressors to store supercritical CO2 in oil wells, which was the object of study of the present work. Normally, the approach used in a compression system design is the simple thermodynamic investigation, without considering fluid dynamic phenomena that can deliver an unfeasible system. Therefore, the methodology developed in this thesis is composed by an optimization methodology based on an one-dimensional (1D) centrifugal compressor model, capable to predict a few fluid flow aspects that are not modeled through direct thermodynamic analysis, followed by a sensitivity analysis (SA) and optimization strategy. Subsequently, the individual modeling of two compressors using Computational Fluid Dynamics (CFD) was necessary to corroborate the previous results and to deliver additional improvements to the equipment from the metamodeling by response surface (RS) of these computationally expensive models and performing an indirect optimization. Associated to the optimization strategy, a constraint called Gas-like Behavior Margin (GBM) is presented to avoid high variations of thermodynamic properties on the compression process close to the Widom-line, which can difficult the numerical model convergence (By CFD) or also can cause damage to the equipment during its operation. The main results obtained throughout the described methodology shows that the train of centrifugal compressors with four stages considered in the optimization process had its total power reduced in 14.09% when compared to the initial configuration, and ensuring a feasible set of compressors, once the constraints: Acceleration Margin to Condensation (AMC), GBM and the Mach number at the throat were met. Moreover, a CFD model for the fourth stage demonstrated good agreement with 1D modeling and experimental data, proving the validity and robustness of the methodology developed herein. Besides, this approach is considered a fast and low-cost way to obtain a

preliminary geometry for centrifugal compressors train systems. Finally, the first and fourth compression stages CFD models were submitted to the SA and optimization, further increasing the polytropic efficiency of both stages, this modeling allowed a phenomenological analysis based on entropic variation to perform the fluid dynamic behavior assessment inside centrifugal compressors. The strategy adopted herein could be applied to other CFD models considered large and high dimensional to reduce the computational cost of optimization procedure and speed-up the phenomenological analysis of fluid flow,

THESIS OUTLINE

Initially, a contextualization of Carbon, Capture Utilization and Storage (CCUS) technologies, including Enhanced Oil Recovery (EOR) strategy is provided, highlighting the advantages of using supercritical CO_2 as working fluid in its compression system. A train of centrifugal compressors for that application is the object of study of this Thesis, that identified some literature gaps in the effort to develop a highly efficient design approach.

In order to achieve highly efficient equipment, four main tools and their physical model and/or mathematical representation were implemented/used: 1) a one-dimensional model of centrifugal compressors was implemented and validated through experimental data, allowing the construction of preliminary geometries that were further investigated by more accurate physical models afterwards, 2) Sensitivity Analysis (SA) and surrogate model training strategy for large and high-dimensional computational models was developed to identify design variables that had low impact on system performance, which speeds up equipment design optimization, 3) Two CFD models for centrifugal compressors were set accordingly to their specific stage of compression, which permits both, thorough phenomenological analysis of the complex fluid flow present in the machine and additional optimization procedures using indirect methods and, 4) Different optimization strategies were applied on the 1D and CFD models, always aiming to improve the thermal performance of the compression system.

The optimization of the compression system as a whole, using the 1D model, delivered a power consumption reduction of 14.08% and provided the preliminary geometries that were further investigated through CFD modeling. The application of screening SA on large CFD models for speed up the design of each centrifugal compressor allowed the surrogate model training that was used on further optimization procedure to additionally increase the performance of the equipment. Furthermore, the 'entropy-guided' phenomenology assessment has identified regions in the computation domain where the sources of losses were prominent in the fluid flow, which explained the improvements on polytropic efficiency. The innovative contributions of this thesis were summarized as follows:

- First to perform an optimization of a compression train that considers geometric and fluid flow phenomena as constraints, ensuring the resulting compression system is feasible;

- Development of the Gas-like Behavior Margin (GBM), ensuring the compression does not reach the transcritical region;

- Development of a low-cost Sensitivity Analysis (SA) strategy capable of properly screening the sample space using only a few model executions and providing both, insights on the model's physical behavior and good data for surrogate model training of large and high-dimensional CFD models, such as turbomachinery;

- Thorough phenomenology assessment of low-flow-coefficient s-CO_2 centrifugal compressor through CFD model and SA, providing physical background for the reduction of power consumption and increase of machine's efficiency found by the optimization procedure.

NOMENCLATURE

Symbols	Description	Units
μ_i^*	Absolute sensitivity measures of Morris' Method	*Depends*
AMC	*Acceleration Margin to Condensation*	*Dimensionless*
ASHOA	Adaptative Sampling Hybrid Optimization Algorithm	-
A-CAES	*Adiabatic Compressed Air Energy Storage*	-
ΔZ	Axial Height	*m*
t	Blade thickness	*m*
CCUS	*Carbon Capture, Utilization and Storage*	-
S_{cfg}	*Centrifugal forces on turbomachinery CFX equations*	-
CFD	*Computational Fluid Dynamics*	-
π_k	*Contribution indices of SS-ANOVA method*	*%*
C_p	Constant-pressure specific heat	*J/kg.K*
S_{cor}	Coriolis acceleration on turbomachinery CFX equations	-
f_c	Correction factor	*Dimensionless*
DoE	Design of Experiment	-
b_3	Diffuser inlet height	*m*
r_3	Diffuser inlet radius	*m*
$P_{t,3}$	Diffuser inlet total pressure	*Pa*
b_4	Diffuser outlet height	*m*
r_4	Diffuser outlet radius	*m*
P_4	Diffuser outlet static pressure	*Pa*
$P_{t,4}$	Diffuser outlet total pressure	*Pa*
K_{dif}	Diffuser total pressure loss coefficient	*Dimensionless*
λ	Distortion factor	*Dimensionless*
EOR	*Enhanced Oil Recovery*	-
EOS	*Equation of State*	-
h_{in}	Enthalpy at the compressor inlet	*J/kg*
μ	Enthalpy head coefficient	*Dimensionless*
h_{sat}	Enthalpy of the isentropic process at saturation	*J/kg*
s_{in}	Entropy at the compressor inlet	*J/kg.K*
s_{sat}	Entropy of the isentropic process at saturation	*J/kg.K*
φ	Flow coefficient	*Dimensionless*
GBM	*Gas-like Behavior Margin*	*Dimensionless*
GGI	General Grid Interface	-
GHGs	*Greenhouse Gases*	-

Symbol	Description	Unit
GCI	Grid Convergence Index	-
C_1	Impeller inlet absolute velocity	m/s
U_1	Impeller inlet tangential velocity	m/s
β_1	Impeller leading-edge Blade Angle	$^\circ$
A_1	Impeller leading-edge incidence area	m^2
r_{1h}	Impeller leading-edge radius at hub	m
r_{1s}	Impeller leading-edge radius at shroud	m
P_1	Impeller leading-edge static pressure	Pa
$U_{1,s}$	Impeller leading-edge tangential velocity at shroud	m/s
$h_{t,1}$	Impeller leading-edge total enthalpy	J/kg
$h'_{t,1}$	Impeller leading-edge total enthalpy - rotating frame	J/kg
$P_{t,1}$	Impeller leading-edge total pressure	Pa
$P'_{t,1}$	Impeller leading-edge total pressure - rotating frame	Pa
d_2/r_2	Impeller outlet diameter/radius	m
U_2	Impeller outlet tangential velocity	m/s
β_2	Impeller trailing-edge blade angle	$^\circ$
b_2	Impeller trailing-edge blade height	m
$\beta_{1,m}$	Inlet blade angle at middle position	$^\circ$
θ_1	Inlet polar angle	$^\circ$
P_{in}	*Inlet static pressure of the EOR system*	bar
T_{in}	*Inlet temperature of the EOR system*	$^\circ C$
$P_{t,in}$	*Inlet total pressure of the EOR system*	Pa
Δh_s	Isentropic enthalpy raise	J/kg
λ_l	Lagrange Multiplier	-
M_{th}	*Mach number at machine's throat*	*Dimensionless*
$\dot{m}$	Mass flow rate	kg/s
v_{sat}	Maximum allowed velocity before condensation	m/s
EE_i	Morris' Elementary Effects	*Depends*
Δ	Morris' method step on discretized sample space	*Dimensionless*
MRF	Multiple Frames of Reference	-
NSGA-II	Non-sorted dominated genetic algorithm II	-
Z_{fb}	Number of impeller's full blades	*Dimensionless*
k	Number of independent variables	-
r	Number of sample space trajectories	-
OAT	One-at-a-time	-
1D	*One-dimensional*	-

θ_2	Outlet polar angle	°
P_{out}	*Outlet static pressure of the EOR system*	*bar*
T_{out}	*Outlet temperature of the EOR system*	*°C*
$\dot{W}_i$	Power required of each compression stage	*W*
ΔP	*Pressure drop in the intercoolers*	*bar*
PR	*Pressure Ratio*	*Dimensionless*
T	Pure torque loading	*N.m*
RBNN	Radial basis neural network	-
RGP	Real Gas Properties	-
RANS	Reynolds Averaged Navier-Stokes	-
RS	Response surface	-
n	*Rotational speed*	*Rpm*
ω	Rotational speed	*Rad/s*
I	Rothalpy on turbomachinery CFX equations	-
RFR	Rotating frame of reference	-
SA	Sensitivity Analysis	-
SP_{targ}	Sizing parameter target of Volute	*Dimensionless*
σ	Slip coefficient	*Dimensionless*
SS-ANOVA	Smoothing Spline Analysis of Variance	-
a_{out}	Sound velocity at EOR system's outlet	*m/s*
a_{sat}	Sound velocity at saturation line	*m/s*
a_{widom}	Sound velocity of Widom line for the outlet temperature	*m/s*
D_s	Specific diameter	*Dimensionless*
ρ_{in}	Specific mass	*kg/m³*
N_s	Specific speed	*Dimensionless*
L_{sf}	Splitter length compared to the main blade	*%*
$s\text{-}CO_2$	*Supercritical CO₂*	-
SC-CCES	Supercritical compressed CO_2 energy storage	-
s-CO2 EOR	Supercritical CO_2 Enhanced Oil Recovery	
$C_{U,1}$	Tangential absolute velocity at impeller leading edge	*m/s*
A_{th}	Throat flow area	*m²*
$M_{th,s}$	Throat Mach number at shroud	*Dimensionless*
$h_{t,th}$	Throat total enthalpy	*J/kg*
$P_{t,th}$	Throat total pressure	*Pa*
T	Torque transmitted	*kPa/rpm*
$\overline{\omega}_i$	Total pressure loss coefficient	*Dimensionless*
$K_{dif-vol}$	Total pressure loss coefficient of diffuser and volute	*Dimensionless*

|		
$\eta_{s,tt}$	Total-to-total isentropic efficiency	*%*
b_2	Trailing-edge blade height	*m*
$s_{t,2}$	Trailing-edge entropy	*J/kg.K*
$P'_{t,2s}$	Trailing-edge isentropic total pressure - rotating frame	*Pa*
$h_{t,2}$	Trailing-edge total enthalpy	*J/kg*
$h'_{t,2}$	Trailing-edge total enthalpy - rotating frame of reference	*J/kg*
$h_{t,2S}$	Trailing-edge total enthalpy of isentropic process	*J/kg*
$P'_{t,2}$	Trailing-edge total pressure - rotating frame of reference	*Pa*
$\dot{W}_p$	Transmitting shaft power	*[kPa]*
ULHS	Uniform Latin Hypercube Sampling	*-*
$\dot{V}$	Volumetric flow rate	*m³/s*
r_5	Volute inlet radius	*m*
$C_{U,5}$	Volute inlet tangential absolute velocity	*m/s*
$P_{t,5}$	Volute inlet total pressure	*Pa*
r_6	Volute outlet radius	*m*
$C_{U,6}$	Volute outlet tangential absolute velocity	*m/s*
$P_{t,6}$	Volute outlet total pressure	*Pa*
K_{vol}	Volute total pressure loss coefficient	*Dimensionless*
τ_{yield}	Yield Strength	*N/m²*

CONTENTS

1 INTRODUCTION

The impact of Greenhouse Gases (GHGs) on the world's environment has driven the scientific community to pursue a reduction of emissions. Renewable energy sources, energy efficiency improvements and atmosphere mitigation of CO_2 are promising alternatives to that purpose. Mitigation of CO_2 can deliver important reductions in the world's total emissions through Carbon Capture, Utilization and Storage (CCUS) technologies, which can reach negative emissions (KOOHESTANIAN *et al*., 2017). For instance, the Adiabatic Compressed Air Energy Storage Systems (A-CAES) strategy (LUO *et al*., 2016) can be applied to mitigate CO_2. Several countries are engaged to assess their CO_2 storage capacities as opportunities for storage and utilization arises. For example, China's geological capacity of CO_2 storage is estimated in 1841 Gt (saline aquifers, coal beds and oil reservoirs), which represents 190 years of their country's emissions, considering 2015's levels (SUN *et al*., 2018). Brazil is also considered an important player for CCUS industry as it has an estimated capacity of CO_2 storage of around 2000 Gt (ROCKETT *et al*., 2013). Of course, not all capacity can be readily used due to available technology and cost limitations.

Supercritical CO_2 usage as a working fluid has increased in the last few years since several advantages are reported. For instance, the increased power generation of Brayton's Cycle compared with an ideal gas, once its low compression work leads to higher thermal efficiency (AHN *et al*., 2015; LIU; WANG; HUANG, 2019). Recent development of 'supercritical compressed CO_2 energy storage' (SC-CCES) system has provided a higher exergy efficiency when compared with a conventional air system, mostly due to higher performance of system components (including centrifugal compressors) (HE *et al*., 2018; XU *et al*., 2021), and the supercritical CO_2 Enhanced Oil Recovery (s-CO2 EOR) strategy that increases oil extraction and the lifetime of the wells (GODOI; DOS SANTOS MATAI, 2021), which is the most economically viable type of geological storage of CO_2 used by the oil and gas industry composed by centrifugal compressors (Figure 1). This last strategy presents a large capability to store CO_2 (140 to 320 billion metric tons) and it can be financially suitable with state incentives, although it is still underused (GODEC *et al*., 2011).

Figure 1 – Centrifugal compressor overview
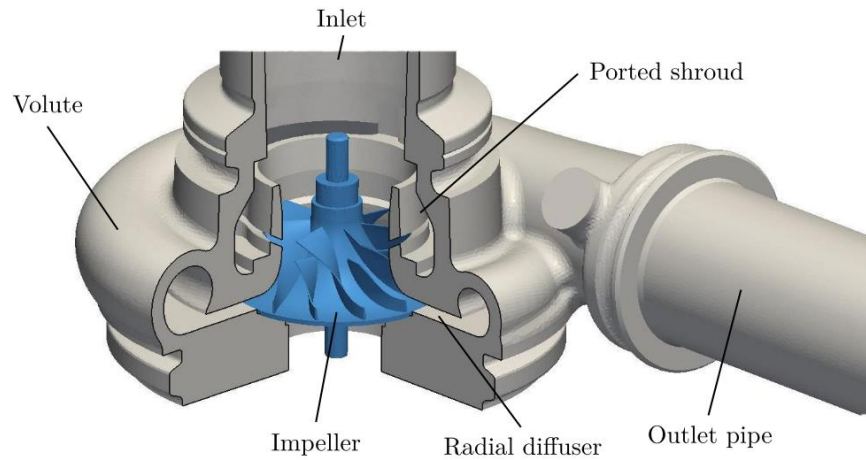
Source: Heinrich (2016).

Compression systems used in EOR are often multi-staged with intercoolers between them to avoid high temperatures. As compressors require most of the energy in the chain, they must be highly efficient, consuming as low as possible power to deliver the desired outlet pressure. Besides the higher efficiency and more compact turbomachinery required for supercritical CO_2, the global warming safety limits are quickly being surpassed; which demands more carbon capture, utilization and storage (CCUS) technologies (CALADO, 2012; GODEC *et al*., 2011). The EOR compression system design is a challenge for engineers, as it can be composed for numerical modeling under different approaches such as one-dimensional models, two-dimensional boundary layer investigations, quasi-three-dimensional flow analysis, or three-dimensional CFD models.

This thesis proposes a methodology for the development of supercritical CO_2 compression trains of EOR systems (Four stages of compression) that combines a one-dimensional model and CFD simulations associated to sensitivity analysis methods and indirect optimization approach, providing reliable results. Also, a new constraint called GBM (Gas Behavior Margin) has been proposed for optimization of the fourth stage of compression.

1.1. Review of one-dimensional modeling for centrifugal compressor train systems

The optimization of performance of the compression train system is essential for ensuring higher efficiencies of each compression stage, diminishing the overall power consumption whilst it turns the EOR system financially more viable. Compression system designs started to rely less on engineers' intuition after optimization started to be performed to determine the number of compression stages in each application (ALLAHYARZADEH-BIDGOLI *et al.*, 2019a, 2021; CALADO, 2012; CHEN *et al.*, 2008; EKRADI; MADADI, 2020; MARTYNOV *et al.*, 2016; MERONI *et al.*, 2018), which was extended for a sort of thermodynamic design variables such as inlet temperature, thermal effectiveness of the intercooler and flow rate (AZIZIFAR; BANOONI, 2016). Multi-staged compression systems optimization led to better thermodynamic performance for supercritical CO_2 as well (AGRAWAL; BHATTACHARYYA; SARKAR, 2007). However, the conventional and direct thermodynamic analysis of compression train systems is perhaps inaccurate to predict the real power required by the system (MODEKURTI *et al.*, 2017; OKEZUE; KUVSHINOV, 2017), since it uses only the isentropic or polytropic efficiencies of the inlet/outlet states to assess losses (NIMTZ *et al.*, 2010), neglecting total pressure loss of internal equipment components. Moreover, compression system optimizations present in literature until now do not consider geometrical constraints and fluid flow phenomena in the equipment as shock waves, flow blockage and condensation. Thus, a well-established one-dimensional (1D) model was implemented in this work, using Python programming language, to assess several important fluid flow phenomena to design an adequate centrifugal compressor train.

A 1D methodology based on loss models of Aungier (2000) and the set of Oh; Yoon; Chung (1997) and implementation based on Monje *et al.* (2014) is defined, which provides good equipment assessment and it is considered a well-developed methodology (KLAUSNER; GAMPE, 2014; XIA *et al.*, 2021), ensuring a proper representation of the centrifugal compressor fluid flow aspects at the impeller, vaneless-diffuser and volute. This 1D model is utilized in several supercritical CO_2 compressors modeled for a Brayton cycle optimization (DU *et al.*, 2021), which has improved its total efficiency. Most of the applications of s-CO_2 compression are related to Brayton cycles, which have low-pressure ratios (AMELI *et al.*, 2017; AMELI; TURUNEN-SAARESTI; BACKMAN, 2018; BALTADJIEV; LETTIERI; SPAKOVSZKY, 2014; DU *et al.*, 2020; LIU; WANG; HUANG, 2019; SHAO *et al.*, 2016). The choice of a set of

losses of a 1D model is due to the internal and external losses that are responsible for assessing fluid flow phenomena that are inherent from operation of the machine, which is crucial for properly predicting flow restrictions and physical constraints of the equipment, regardless the working fluid (Air or CO2, each one with its own equation of state). Consequently, the set of losses of the widely used optimum set (OH; YOON; CHUNG, 1997) was established and can be used for other fluids as well. Even though Cho *et al*. (2021) evaluates Lee's configuration to be slightly better specifically for s-CO2, it recognizes that their greater difference is on disk friction loss model, which depends on facility installation as well. Thus, the set of losses in a 1D model is as good as its experimental validation, which must be enough for ensuring validity for the presented designer application.

In the compression train systems of EOR systems, the pressure ratios are higher in order to achieve the desired reinjection pressure. Actually, the last stage must be higher than 3, which implies a low-flow coefficient for these types of machines, indicating higher losses due to friction at the impeller exit channel and resulting in a significant reduction in the machine efficiency (AUNGIER, 2000). Such high-pressure ratios combined with low-flow coefficients have not been widely investigated yet. Furthermore, the centrifugal compressor for CO_2 reinjection works in a supercritical state, near the critical point, which may difficult the Computational Fluid Dynamics (CFD) model convergence due to high variations of thermodynamic properties (LEE *et al*., 2016). The phenomenon of the transcritical region is still not fully understood by the scientific community (LETTIERI; YANG; SPAKOVSZKY, 2015). For example, Bae *et al*. (2015) reported a noticeable difference between their model prediction and experimental data, at the compressor outlet, due to the uncertainties of CO_2 properties variation near the critical point, some uncertainties on isentropic efficiency measurements presented in literature are as high as 125% (LEE *et al*., 2016). The experimental data at this level of pressure led the researchers to circumvent that issue without well-defined criteria. The most accessible s-CO_2 centrifugal compressor's experiment is in SANDIA's report (WRIGHT *et al*., 2010), but it has a much lower pressure ratio (1.5) than the used in this work. Others s-CO_2 test data on literature have reported crucial information as compressor geometry/operational aspects which allows a validation process for the 1D model (CHA *et al*., 2021; PARK; CHA; LEE, 2022; ZHU *et al*., 2023).

Therefore, a one-dimensional modelling is an essential tool for properly designing centrifugal compressors. Its usage provides a proper preliminary geometry for the impeller, respecting

physical and spatial constraints that are common on practical applications. Of course, this initial geometry is further investigated by more accurate models as in CFD methodology since three-dimensional phenomena are highly relevant for ensuring adequate compressor operation near critical point.

1.2. Review Of Sensitivity Analysis (SA) And Optimization for CFD Models of Centrifugal Compressors

Centrifugal compressors are rotating machines that operate at very high velocities and have their performance and fluid flow impacted by geometry variables such as blade angles and thicknesses, which leads to complex turbulent flows with swirl and shock waves, making the design of high-performance turbomachinery a great challenge for engineers. In general, as presented in section 1.1, a centrifugal compressor design starts with one-dimensional approach, such as the Meanline (BLANCHETTE *et al*., 2016), streamline curvature (CASEY; ROBINSON, 2008a) or the aforementioned Aungier (2000) methods. More recently, these models have been complemented by modern three-dimensional CFD models that provide a better description of the physical phenomena, higher accuracy and robustness to the design.

From CFD analysis, Marconcini *et al*. (2008) and Ibaraki *et al*. (2002) previously identified two main physical phenomena that cause severe losses in centrifugal compressors: shockwaves at the leading edge caused by high velocities of the blade and swirl throughout the passage volume. Kim *et al*. (2010) parameterized two intermediate meridional flow path points of an air centrifugal compressor impeller and performed an optimization based on a radial basis neural network (RBNN), improving the efficiency of the reference impeller (85.98%) by 1.0% at the design point. Javed *et al*. (2016) performed multi-objective optimization using impeller and diffuser design variables improving the efficiency (81.11%) by 0.68% to 2.03% at the design point. Li *et al*. (2019) introduce the Adaptative Sampling Hybrid Optimization Algorithm (ASHOA) to deal with the high costs of turbomachinery CFD models improving efficiency by 1.61%.

Although improvements in the efficiency of air compressors have been found by previous optimizations in turbomachinery, there is still a lack of Sensitivity Analysis (SA) tools usage in order to improve the design of such equipment. Overall, SA is a statistical tool that studies how

the model input variables affect the interest outputs, describing the importance of each input on the variability of the output. There are a large number of SA methods available from qualitative screening to quantitative variance-based methods (CAMPOLONGO; SALTELLI; CARIBONI, 2011). The Elementary Effects (EE) method introduced by Morris (1991) and refined by Campolongo *et al*. (2007) is considered good practice in qualitative SA for CFD models with a high computational cost. This screening method seeks to identify non-influential input variables for high-dimensional and computationally expensive models using a relatively small number of original model evaluations. Moreover, it provides a good initial sense of the problem, which contributes to diminishing the number of input variables for an optimization procedure, decreasing computational cost before the analyst proceeds to a quantitative method (CAMPOLONGO; SALTELLI; CARIBONI, 2011).

Otherwise, quantitative methods estimate a representative sensitivity index as the percentage of the output variance due each variable. However, these methods require numerous assessments in model evaluations, which becomes prohibitive for large CFD models. A promising approach to sensitivity analysis and the optimization of high dimensional and computationally expensive models is the combination of qualitative screening methods followed by Response Surface Methodology (RS) with a good fitness that can be used to approximate the model's behavior at a determined sample space region. Most efforts are dedicated to developing and calibrating an RS that is dependent on the number of variables contained in the model (dimensionality). Furthermore, when the model itself is high-dimensional and the interactions among the variables are not negligible, it is difficult to achieve good fitness for the RS (GE; CIUFFO; MENENDEZ, 2014). Once the RS is trained and tested, the estimations of quantitative sensitivity indices are very fast. For example, Dezan *et al*. (2018) used the smoothing spline ANOVA model (SS-ANOVA) as a quantitative SA method to access the influence of the geometrical variables on two different physical outputs of a compact heat exchanger, corroborating the robustness of this quantitative method. Ciuffo *et al*. (2013), confirmed the reliability of sensitivity indices calculations using RS, showing variance-based indices practically identical to those estimated by the original model.

Therefore, the development of a proper SA methodology that combines a low-cost of EE method with the reliability of SS-ANOVA method is a promising approach for the turbomachinery CFD model's design since it can reduce the computational effort of an

optimization procedure using its data to train Response Surfaces (RS), provide phenomenology insights for the designer and reduce the number of geometric design variables through a factor fixing procedure.

1.3.   S-CO$_2$ compression system setup and constraints

In order to detail the object of study of the present work, Table 1 shows inlet and outlet conditions of the sCO$_2$-EOR compression system studied. The inlet pressure is above atmosphere's due to the process in which CO$_2$ is obtained in platform operation. Thus, the main goal is to increase the fluid pressure from 4 to 250 bar, which is a typical pressure range operation for CO$_2$ on EOR compression systems (ALLAHYARZADEH-BIDGOLI *et al*., 2021) and cannot be done in a single compression stage due to machine limitations and high temperatures. For this, intercoolers have been considered between the compression stages (Figure 2), based on space availability and performance discussed by Allahyarzadeh-Bidgoli *et al*. (2019). Moreover, a purely thermodynamic analysis conducted previously (ALLAHYARZADEH-BIDGOLI *et al*., 2021) has determined the number of stages (four) for the compression system studied herein, which has reduced the expected total power consumption in 5.8%, in comparison to a three-staged system.

Table 1 – CO$_2$-EOR compression system inlet/outlet conditions.

Operational Variable	Inlet Conditions	Outlet Conditions
Static Pressure	4 bar	250 bar
Temperature	40°C	40°C
Mass flow	55.56 kg/s	55.56 kg/s

Source: Author.

The intercoolers are responsible for decreasing the outlet temperature of each compression stage, delivering to the next compressor CO$_2$ at 40°C. Moreover, a pressure drop is also considered and, for simplicity purposes, is equal to 0.5 bar for each intercooler device. The compression stages are independent, meaning that each equipment can have its rotational speed

(*n*) and pressure ratio (PR). Thus, several PR combinations can deliver the desired outlet pressure. However, some configurations of the train system could be unfeasible, since the machine restrictions and fluid flow phenomena cannot meet the 1D model constraints.

Figure 2 - Compression system of CO_2-EOR diagram.
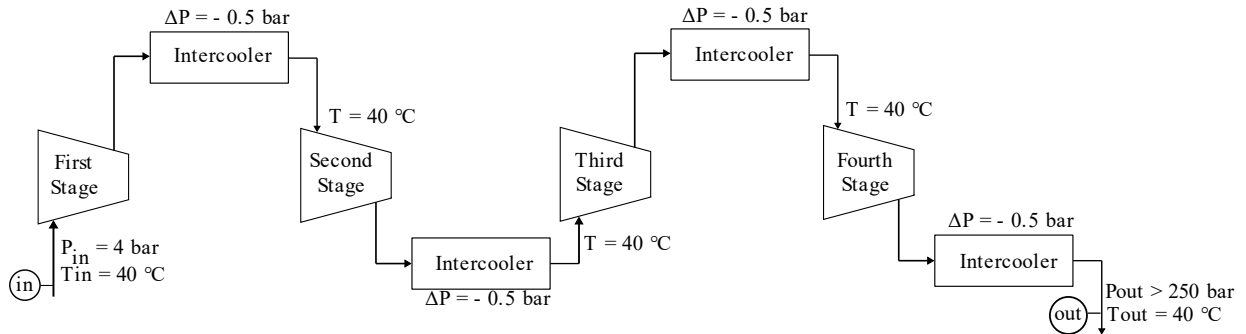
Source: Author.

The several constraints can be divided into two groups: Single-stage restrictions for each stage compression, and system restrictions due to the whole system setup (Table 2).

Table 2 – Constraint for the compression system.

Group	Restriction	Limit
Single Stage	Throat Mach number	< 1 (IBARAKI *et al*., 2007)
	Outlet Temperature	< 200 °C
	Rotational Speed	< 30000 RPM (FULLER; PREUSS; NOALL, 2012)
System	Acceleration Margin to Condensation ($M_{th,4}$/AMC)	< 1 (MONJE *et al*., 2014)
	Gas-like Behavior Margin (*GBM*)	< 1

Source: Author.

The most significant single-stage machine restriction is the maximum Mach number at the impeller leading-edge. If shock waves are generated at that point, there is an increase in efficiency loss and a decrease in the stable operational range (IBARAKI *et al*., 2007). To avoid that issue, the Mach number at the impeller throat must be under unity. Moreover, a limit of 200

°C was set at the outlet temperature for each stage since there is not much space available in oil-gas platforms and heat exchanger sizes and weights are quite limited. Another important constraint is the rotational speed since high shaft speeds (over 30000 rpm) can reduce the life of the seals and gears of the system (FULLER; PREUSS; NOALL, 2012). Two system restrictions have been related to the fluid flow phenomena at the last stage of compression. The Acceleration Margin to Condensation (AMC) (MONJE *et al*., 2014) was considered to avoid condensation at the inlet and a novel Gas-like Behavior Margin (GBM) is firstly proposed herein to ensure the s-CO_2 operates in the gas-like region to avoid CFD convergence issues in the near-critical point region. If GBM is not considered as a constraint, the compressor inlet or parts of the compression process would be allowed to happen at a high variation of properties region, in which transcritical practical problems would occur. Therefore, the GBM constraint is not only preventing the outlet to enter the transcritical region but the entire compression process of the last stage, which is extremely necessary for a feasible compression system design. The temperature/entropy diagram shown in Figure 3 illustrates both restriction margins.

Figure 3 – AMC and GBM represented in the T-s diagram for supercritical CO_2.
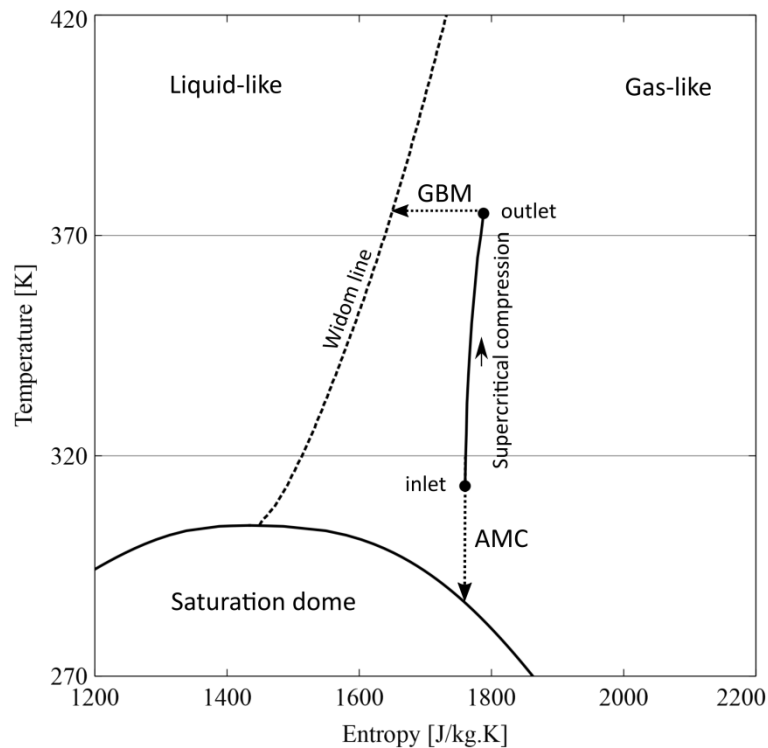
Source: Author.

The AMC is referred to as the maximum allowed Mach number at the impeller throat to ensure that condensation would not take place (MONJE *et al.*, 2014). For better elucidation, the energy conservation (definition of total enthalpy: $h_{in} = h_{sat} + v_{sat}²$) between the thermodynamic state of the compressor inlet and the saturation line of an isentropic expansion gives:

$$v_{sat} = \sqrt{2(h_{in} - h_{sat})} \tag{1}$$

$$s_{sat} = s_{in} \tag{2}$$

in which v_{sat} is the maximum allowed velocity before condensation occurs, h_{in} and s_{in} are the enthalpy and entropy at the compressor inlet, respectively. The h_{sat} and s_{sat} are the enthalpy and entropy at the saturation line of the isentropic process, respectively.

Using a proper Equation of State (EOS) it is possible to calculate the sound velocity (a_{sat}) at the saturation state, since $a_{sat} = f(h_{sat}, s_{sat})$. Thus, AMC can be defined as:

$$AMC = \frac{v_{sat}}{a_{sat}} \tag{3}$$

Therefore, the restriction to avoid condensation due to fluid acceleration at the compressor inlet is that the real absolute Mach number at the impeller throat (M_{th}) cannot be higher than the AMC (AMC > M_{th}), which means the velocity achieved at the equipment throat is not high enough to take the static thermodynamic state to enter the saturation dome. Direct thermodynamic analysis of the compression system would not predict this kind of restriction as it does not have geometry and operational data of the centrifugal compressor to calculate the real flow velocities, which is only possible after 1D modeling estimates the preliminary 1D fluid flow.

Similarly, the present study has proposed a new criterion called GBM (Gas-like Behavior Margin) to ensure a gas-like behavior for supercritical fluids. The points of the maximum value of constant-pressure specific heat (C_p) above the critical point define the Widom Line (SIMEONI

et al., 2010), which is due to experimental observation of thermodynamic properties behavior above the critical point. It was noticed two distinct regions, the gas-like region (low values of density) and the liquid-like region (high values of density) and a transitional region (where high properties variation are present) often called as transcritical region that starts on the vicinity of the Widom line. This line was used herein as a limit for high property variations.

Furthermore, gas-like behavior is essential for the adequate operation of centrifugal compressors since several issues are reported at the near-critical point as non-linear properties changes causing very high uncertainties (LEE *et al.*, 2016) and CFD simulations instabilities even for low-pressure ratio (AMELI *et al.*, 2017). The compression process is designed to not cross the Widom Line, ensuring better accuracy in thermophysical properties and CFD convergence. Thus, the compressor outlet state needs to be at the gas-like behavior region as shown in Figure 3. For it, the (GBM) is proposed as an isothermal ratio of the sound velocities between the compressor outlet and the Widom line:

$$GBM = \frac{a_{out}(T_{out})}{a_{widom}(T_{out})} \tag{4}$$

in which T_{out} and a_{out} are the temperature and sound velocity at the compressor outlet, respectively. The a_{widom} is the sound velocity at the Widom line evaluated at the same temperature.

Sound velocity was chosen as the thermodynamic property to perform the GBM since its value at the Widom line is always higher than the gas-like region, meaning that the GBM value must be always less than unity (GBM < 1) to guarantee gas-like behavior and avoid undesirable transcritical flow phenomena, ensuring that the s-CO2 compressor operates at the gas-like region. Also, the total power consumption of the multi-staged compression system will be minimized, taking the whole train into account. For that, the one-dimensional model of the impeller, vaneless-diffuser and volute will be considered for each compression stage and submitted to a constrained-optimization procedure taking into account thermodynamic, geometry and fluid flow aspects of all four compression stages.

Afterwards, a CFD analysis of the last stage of compression was performed to ensure model accuracy and also to check the GBM constraint. Thus, the next step to design a s-CO$_2$ compression system is the optimization of each stage using the more accurate CFD model, which

is a computationally expensive procedure. Thus, this work aims to develop a high-dimensional design optimization strategy for very low-flow coefficient centrifugal compressors that are required on EOR compression systems, combining the SA methods and RS training with a CFD model phenomenology evaluation.

1.4. Objective of the Thesis

Summing up, the main objective of this thesis can be highlighted as:

- Develop a design methodology for a higher efficient centrifugal compressor train of s-CO2 for EOR systems (as presented in the flowchart of Figure 4).

Each step of the flowchart of Figure 1.4 is further addressed in the appropriated section. In short, a one-dimensional optimization is performed to reduce total power consumption and provides the preliminary geometry for the four stages of the compression train. Two CFD models were constructed, one for the first and other for the last stage, to be further improved by 3D analysis. The first stage was optimized to gain model 'knowhow' and evaluate the SA methodology. The last stage optimization assessed the influence of high number of interacting variables and fluid flow phenomena in low-flow-coefficient compressors operating with supercritical CO2.

Figure 4 – Overall Design Strategy for Sensitivity Analysis and Optimization.
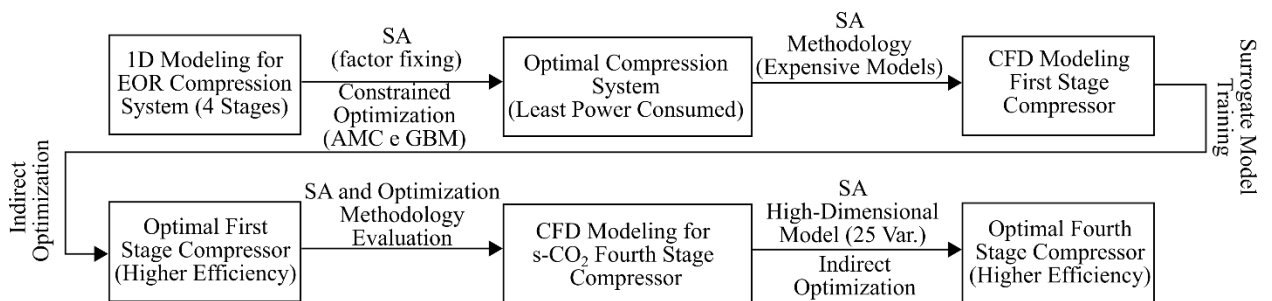
Source: Author.

Also, the relevant scientific contributions presented by this thesis can be listed as:

- First to perform an optimization of a compression train that considers geometric and fluid flow phenomena as constraints, ensuring the resulting compression system is feasible;

- Development of the Gas-like Behavior Margin (GBM), ensuring the compression does not reach the transcritical region;

- Development of a low-cost Sensitivity Analysis (SA) strategy capable of properly screening the sample space using only a few model executions and providing both, insights on the model's physical behavior and good data for surrogate model training of large and high-dimensional CFD models, such as turbomachinery;

- Thorough phenomenology assessment of low-flow-coefficient s-CO_2 centrifugal compressor through CFD model and SA, providing physical background for the reduction of power consumption and increase of machine's efficiency found by the optimization procedure.

2   METHODOLOGY

This section presents the four tools utilized to develop this thesis:

- The implementation of the one-dimensional model of centrifugal compressors in Python programming language, which turned possible to include geometric and fluid flow constraints in the optimization procedure;
- The SA strategy defined to decrease the computational cost of large CFD model's optimization, which includes the Elementary Effects method that was implemented in R programming language (Quasi-optimal sampling procedure to generate de Design of Experiment (DoE) and the sensitivity measures computation) and the SS-ANOVA method that was already implemented in ModeFrontier software.
- The appropriate setup of s-CO_2 CFD models for centrifugal compressors in CFX software, including the Real Gas Properties (RGP) table study required for proper representation of thermodynamic properties at supercritical condition.
- The development of an optimization strategy for the EOR train of compression using the Non-Sorted-Dominated Genetic Algorithm (NSGA-II) already implemented in ModeFrontier software.

As already mentioned, the Enhanced Oil Recovery (EOR) process requires a multi-staged compression system to operate using s-CO_2. The commercially available 1D models responsible for providing preliminary geometry for designers do not comprehend supercritical conditions due to the limitations of its Equation of State (EoS). Therefore, a 1D model is developed herein to provide preliminary geometries of a multi-staged compression system working with s-CO_2.

2.1 D model for compression train design

The one-dimensional (1D) design method implemented in this study is based on Aungier (2000) and Monje *et al*. (2014). Centrifugal compressors are divided into three main parts:

Impeller, diffuser and volute (Figure 5). Each of these components have been evaluated as described below for the four stages of the compression chain.

Figure 5 – Meridional representation of the centrifugal compressor for 1D methodology.
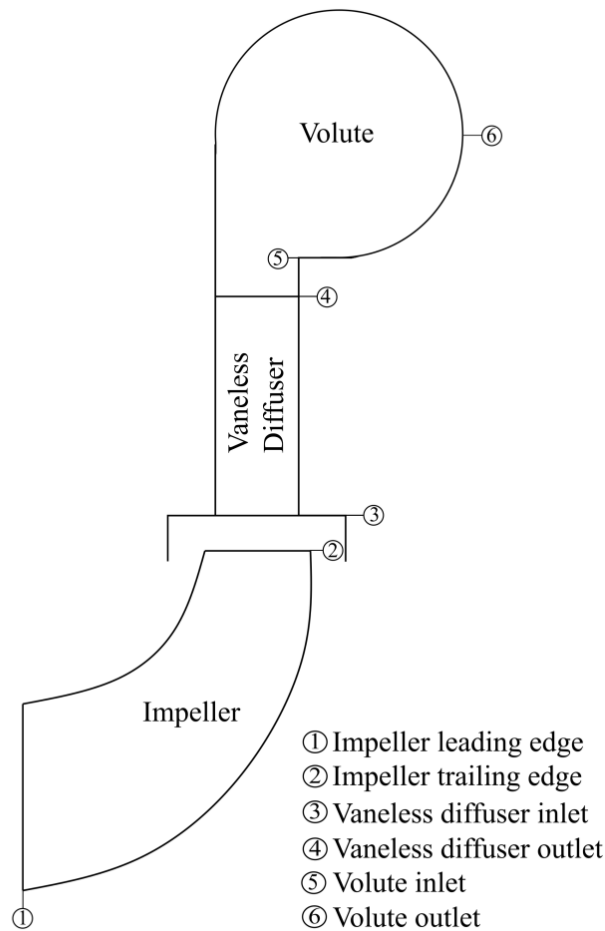
Source: Author.

The total thermodynamic conditions at the inlet of each compressor (Figure 2) are determined due to system inlet conditions and to previous stage calculation, which allows the designer to define relevant compressor features such as pressure ratio and the number of blades. Of course, inlet conditions of subsequent stages depend on the PR combination for the four stages of the compression system. Moreover, the rotational speed and trailing edge diameter are based on specific speed (N_s) and specific diameter (D_s), according to Balje (1981):

$$N_s = \frac{\omega \dot{V}^{\frac{1}{2}}}{\Delta h_s^{\frac{3}{4}}} \tag{5}$$

$$D_s = \frac{d_2 \Delta h_s^{\frac{1}{4}}}{\dot{V}^{\frac{1}{2}}} \tag{6}$$

in which ω is the rotational speed in radians per second, $\dot{V}$ is the volumetric flow rate, d_2 is the impeller outlet diameter and Δh_s is the isentropic enthalpy raise.

Their choice depends on the flow coefficient (φ) and enthalpy head coefficient (μ) (RODGERS, 1997), presented in equations (7) and (8), and on rotational speed and throat Mach number restrictions (AUNGIER, 2000).

$$\varphi = \frac{\dot{m}}{\rho_{in} \pi r_2^{\,2} U_2} \tag{7}$$

$$\mu = \frac{\Delta h_s}{U_2^2} \tag{8}$$

in which $\dot{m}$ is the mass flow rate, ρ_{in} is the specific mass at the inlet total conditions, r_2 is the impeller outlet radius and U_2 is the impeller outlet tangential velocity.

Thus, each stage of compression was chosen to satisfy the constraints resulting in Table 3 values. To avoid high rotational speed and condensation at the impeller throat, low-flow coefficient compressors are often employed for the last stage of compression of EOR systems, resulting in narrower flow channels than usual, which leads to higher friction losses (LETTIERI *et al*., 2014).

Table 3 – Specific speed, specific diameter, flow coefficient, enthalpy head, rotational speed and trailing edge diameter of each compression stage.

Compression stage	First stage	Second stage	Third stage	Fourth stage
Specific speed (N_s)	0.52	0.52	0.52	0.3
Specific diameter (D_s)	5	5	5	9
Flow coefficient (φ)	0.039	0.039	0.039	0.012
Enthalpy head (μ)	0.592	0.592	0.592	0.549

Source: Author.

2.1.1 Impeller

The impeller is the rotating part of the equipment where the fluid is accelerated. The majority of the machine losses are in this section and its design is divided into two parts: leading and trailing edges. First, a structural evaluation of the minimum inlet hub radius is performed to ensure shaft mechanical integrity using the typical values of yield strength (τ_{yield}) and pure torque loading (LOEWENTHAL, 1984):

$$r_{1h,min} = \left(\frac{2T}{\pi(0.7\tau_{yield})}\right)^{1/3} \tag{9}$$

in which: $\tau_{yield} = 1050$, $r_{1h,min}$ is the minimum allowed hub radius and T is the torque transmitted:

$$T = 9550\frac{\dot{W}_p[kPa]}{n\,[rpm]} \tag{10}$$

where $\dot{W}_p$ is the transmitting shaft power and n is the rotational speed. The inlet hub radius (r_{1h}) is selected using a chosen safety factor of 1.2 ($r_{1h} = 1.2r_{1h,min}$). Moreover, the inlet shroud radius (r_{1s}) requires a complete evaluation of the leading-edge design since its choice has a great impact on throat Mach number. Values between 30 and 50% of the impeller outlet radius (r_2) usually results in an acceptable throat Mach number (AUNGIER, 2000).

The leading-edge evaluation is to perform the incidence and throat velocity triangles (Figure 6) and, consequently, the inlet blade angles at different leading-edge spam positions.

Figure 6 – Leading-edge and throat velocity triangles.
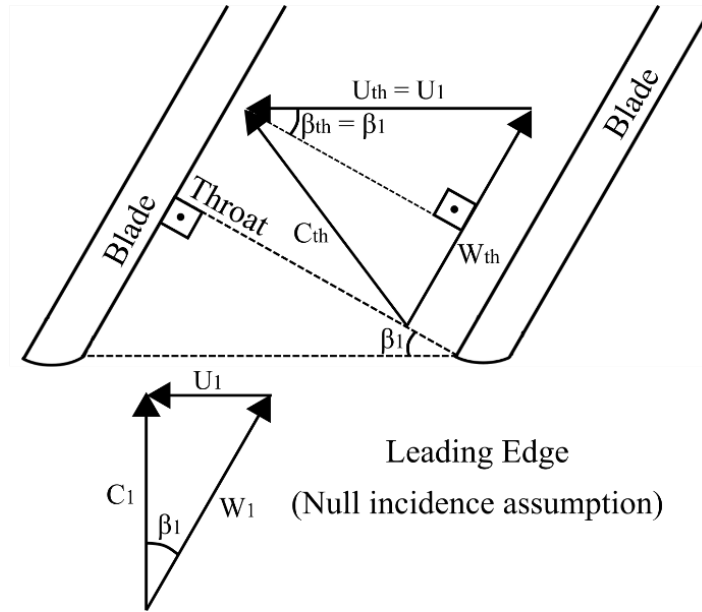
Blade thickness is considered constant ($t_{1,s} = t_{1,h} = t_2$) and values between 2% and 3% of impeller diameter were chosen. The null incidence assumption ($C_{1,U} = 0$) implies that the leading-edge velocity triangle shown in Figure 6, in which the leading-edge incidence flow area (A_1) is:

$$A_1 = \pi(r_{1s}{}^2 - r_{1h}{}^2) - (r_{1s} - r_{1h})t_1 Z_{fb} \tag{11}$$

and the tangential velocity has to be evaluated at the radius section where the analysis is taking place (hub, mid or shroud spam position):

$$U_{1,s} = \omega\, r_{1s} \tag{12}$$

Evidently, the maximum tangential velocity value is verified at the highest value of radius (r_{1s}) since ω is constant, which results in the highest throat Mach ($M_{th,s}$) number of the leading edge. The leading-edge definition requires an iterative procedure at the hub, mid and shroud positions, as indicated by the flowchart shown in Figure 7, which summarizes the whole leading-edge iterative solution explained next.

Figure 7 – Flowchart of the leading-edge iterative solution.
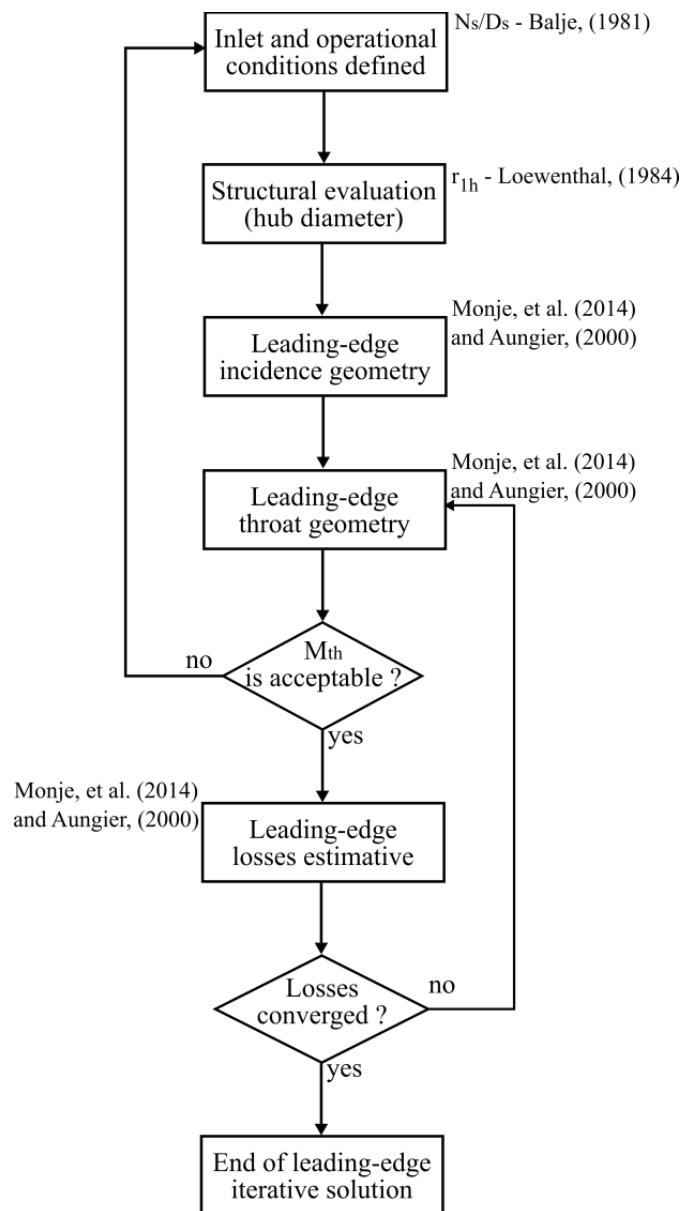
Source: Author.

Thermodynamic properties at the leading edge are assumed to be equal to the compressor inlet as an initial guess. Thus, a looping between continuity (Equation 13), energy conservation (Equation 14), velocity triangle (Equation 15) and EoS (R.SPAN; W.WAGNER, 1994) is performed until the absolute velocity is converged. The leading-edge incidence geometry is completely determined once hub, mid and shroud incidence angles are calculated. However, the Mach number can reach higher values at the throat causing shockwaves and/or condensation (MONJE *et al*., 2014). Therefore, the Mach number at the throat needs to be considered before the impeller outlet design.

$$C_1 = \dot{m}/(\rho_1 A_1) \tag{13}$$

$$H_1 = H_{in} - \frac{C_1{}^2}{2} \tag{14}$$

$$\beta_1 = tan^{-1}(U_1/C_1) \tag{15}$$

The initial guess for the thermodynamic state at the throat is previously calculated for the leading-edge incidence state and the throat flow area is estimated as $A_{th} = A_1 \cos(\beta_1)$ (AUNGIER, 2000). Then, the same loop of equations is applied to the throat, using correlations shown in Figure 6. Once the Mach number at the throat is computed at the hub, mid and shroud radius, the leading-edge analysis is completed. If one finds prohibitive Mach numbers at the throat, the design must be restarted: changes in shroud radius, flow coefficient, specific speed or any other impacting design variables should be performed.

After the leading-edge definition, its losses can be assessed (AUNGIER, 2000; MONJE *et al*., 2014). The leading-edge losses are summed and an iterative thermodynamic state correction is initiated since there is a dependency between flow velocity triangles and the thermodynamic state. The throat-corrected state is defined by energy conservation and total pressure loss estimative ($\bar{\omega}_i$):

$$\begin{aligned} h_{t,1} &= h_{t,th} \\ P_{t,th} &= P_{t,1} - (P_{t,1} - P_1)\sum_1^{th} \bar{\omega}_i \end{aligned} \tag{16}$$

After the throat state is updated, the velocity triangles and leading-edge losses are computed iteratively until those losses' values are converged. A sudden contraction area loss was proposed:

$$\bar{\omega}_{cont} = \frac{r_{1h}{}^4}{r_{1s}{}^4} \tag{17}$$

Moreover, three other losses are estimated on the leading edge (Aungier 2000). Incidence loss, due to differences between flow and blade angles and the reduction of flow area:

$$\bar{\omega}_{inc} = 0.8 \left(1 - \frac{C_{1,m}}{w_1 \cos(\beta_1)}\right)^2 + \left(\frac{Z_{fb} t_1}{2\pi r_1 \cos(\beta_1)}\right)^2 \tag{18}$$

in which the effective loss is the weighted average computed in hub, mid-span and shroud in proportion of 1, 10 and 1, respectively. Diffusion loss term is estimated for impellers that the diffusion of flow between the leading edge and the throat is more significant than the incidence loss,

$$\bar{\omega}_{DIF} = 0.8 \left(1 - \frac{w_{th}}{w_1}\right)^2 - \bar{\omega}_{inc} \tag{19}$$

in which a stall criterion is suggested as $\frac{w_{1,s}}{w_{th}} \geq 1.75$. If stall is predicted, a limit for diffusion loss is $\bar{\omega}_{DIF} = \left((w_{1,s} - 1.75 w_{th})/w_1\right)^2 - \bar{\omega}_{inc}$. If sonic conditions are found in impeller throat, an additional loss has to be estimated, the choking loss:

$$\bar{\omega}_{CH} = 0.5(0.05X + X^7), if\ X > 0 \tag{20}$$
$$\bar{\omega}_{CH} = 0, if\ X \leq 0$$

in which $X = 11 - 10 C_r A_{th}/A^*$, the contraction ratio correlation is $C_r = \sqrt{A_1 \cos(\beta_1)/A_{th}}$) and the sonic throat area is $A^* = \frac{\dot{m}}{\rho_{th} a_{th}}$.

The impeller trailing-edge design is based on a velocity triangle (Figure 8), which provides the impeller trailing-edge angle (β_2) and blade height (b_2). Of course, as the velocity field

impacts the thermodynamic state an iterative procedure is required as well. The impeller trailing edge needs to achieve a total pressure that compensates for the losses on the diffuser and volute ($K_{dif-vol}$), as well as the total-to-total isentropic efficiency ($\eta_{s,tt}$) on the impeller itself. Therefore, an initial guess is required for both terms ($K_{dif-vol} = 10\%$ and $\eta_{s,tt} = 80\%$).

Figure 8 – Trailing-edge velocity triangle considering slip (σ) and distortion factor (λ).
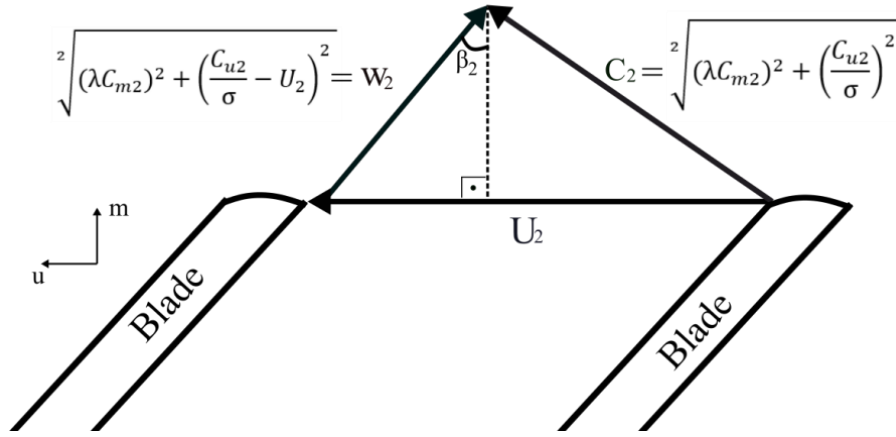
Source: Author.

Moreover, an ideal performance is also guessed initially ($\sigma = 1$; $\lambda = 1$ and $\sum_1^2 \overline{\omega}_i = 0$) and a three-level impeller trailing-edge loop (Figure 9) is initiated as proposed by (MONJE *et al.*, 2014). The impeller losses are assessed by the models of (AUNGIER, 2000; OH; YOON; CHUNG, 1997), recalculating the values of σ, λ and $\sum_1^2 \overline{\omega}_i$.

Friction losses were assessed with the friction coefficient (C_f) of the Boundary Layer Theory in (SCHLICHTING, 1979) and its pressure loss coefficient is defined as

$$\overline{\omega}_{fr} = 4C_f \frac{L_B}{\bar{d}_H} \left(\frac{\bar{w}}{w_1}\right)^2 \tag{21}$$

in which L_B is the impeller channel length (AMELI *et al.*, 2019), $L_B = \frac{\pi}{8}(2r_2 - 2r_1 - b_2 + 2\Delta Z)\left(\frac{4}{\cos\beta_{1s} + \cos\beta_{1h} + 2\cos\beta_2}\right)$; $\bar{d}_H$ is the mean hydraulic diameter between throat and trailing edge;

$\overline{w}$ is the mean relative velocity at the impeller, $\overline{w} = \sqrt{\frac{(w_1^2 + w_2^2)}{2}}$; and $Z = r_2 * \left(0.014 + 0.023 * \left(\frac{r_2}{r_{1h}}\right) + 1.58\varphi\right)$, is the axial length.

Pressure gradient on the impeller causes blade loading losses and are estimated in two directions: blade-to-blade and hub-to-shroud.

- Blade-to-blade coefficient:

$$\overline{\omega}_{Bl} = \frac{1}{24}\left(\frac{\Delta w}{w_1}\right)^2 \tag{22}$$

in which $\Delta w = \frac{2\pi d_2 U_2 I_B}{Z_{eff} L_B}$ is the maximum velocity difference, $Z_{eff} = Z_{FB} + Z_{SB}\left(\frac{L_{SB}}{L_{FB}}\right)$ is the effective number of blades due to splitters; and $I_B = \sigma\left(1 - \frac{\dot{m}\,\lambda\,\tan\beta_2}{\rho_2 A_2 U_2}\right) - \frac{U_1 C_{U1}}{U_2^2}$ is the work input coefficient, where the slip factor (σ) is estimated as in Wiesner (1967).

- Hub-to-shroud coefficient:

$$\overline{\omega}_{HS} = \frac{1}{6}\left(\frac{\overline{k}_m\,\overline{b}\,\overline{w}}{w_1}\right)^2 \tag{23}$$

in which $\overline{k}_m = \frac{\alpha_{C1} - \alpha_{C2}}{L_B}$ is the stream line curvature, $\overline{b} = \frac{(r_{1s} - r_{1h}) + b_2}{2}$ is the mean channel width and $\overline{w} = \frac{w_1 + w_2}{2}$ is the mean relative velocity at the impeller.

The complex mixing of flow zones at the impeller channel requires the modeling of mixing losses due to the abrupt expansion (BENEDICT; CARLUCCI; SWETZ, 1966) of the distorted main flow encountering the impeller outlet blockage and the flow wakening after impeller trailing edge. The abrupt expansion and the wake mixing loss coefficients are defined as:

$$\overline{\omega}_\lambda = \left(\frac{(\lambda - 1)C_{m2}}{w_1}\right)^2 \tag{24}$$

$$\overline{\omega}_{wake} = \left(\frac{C_{m2,wake} - C_{m2,mix}}{w_1}\right)^2 \tag{25}$$

in which the well-known distortion factor is $\lambda = \frac{1}{1-B_2}$ and the blockage estimative is defined as

$B_2 = \overline{\omega}_{fr} \frac{P_{t,1}-P_1}{P_{t,2}-P_2} \sqrt{\frac{w_1 \overline{d}_H}{w_2 b_2}} + \left(0.3 + \frac{b_2^2}{L_B^2}\right) \frac{A_R^2 \rho_2 b_2}{\rho_1 L_B} + \frac{\delta_{CL}}{2b_2}$; where $A_R = \frac{A_2 cos\beta_2}{A_1 cos\beta_{th}}$ and δ_{CL} is the clearance

gap size. Also, $C_{m2,wake} = \sqrt{w_2^2 - w_{U,2}^2}$ and $C_{m2,mix} = \frac{C_{m2} A_2}{\pi d_2 b_2}$.

The clearance gap on blade tip implies pressure differences and mass flow between blade sides near the shroud. Thus, a clearance loss coefficient has to be considered:

$$\overline{\omega}_{CL} = \frac{2\, \dot{m}_{CL} \Delta P_{CL}}{\dot{m}\, \rho_1 w_1^2} \tag{26}$$

in which the clearance gap mass flow is $\dot{m}_{CL} = \rho_2\, Z_{eff}\, s\, L_B\, C_{CL}$, the pressure difference between blade sides is $\Delta P_{CL} = \frac{\dot{m}\, (r_2 C_{U,2} - r_1 C_{U,1})}{Z_{eff}\, \overline{r}\, \overline{b} L_B}$ and the clearance absolute velocity is $C_{CL} = 0.816\sqrt{2\Delta P_{CL}/\rho_2}$.

Total pressure loss assessment at the impeller is conducted at the reference rotating frame, in which inlet and outlet states depend on its total states and absolute velocities:

$$\begin{aligned}
h'_{t,1} &= h_{t,1} - U_1 C_{U,1} + \frac{U_1^2}{2} \\
h'_{t,2} &= h'_{t,1} + \frac{(U_2^2 - U_1^2)}{2} \\
P'_{t,2} &= P'_{t,2s} - f_c(P'_{t,1} - P_1)\sum_1^2 \overline{\omega}_i
\end{aligned} \tag{27}$$

in which $P'_{t,2s} = f(h'_{t,2}, s_1)$ and $P'_{t,1} = f(h'_{t,1}, s_1)$ are obtained through the EoS (R.SPAN; W.WAGNER, 1994), assuming an isentropic compression process; and $f_c = \frac{P'_{t,2}}{P'_{t,1}}$ is the correction factor since the loss coefficients are based on the inlet conditions. f_c and $P'_{t,2}$ are iteratively evaluated until f_c is converged.

After the rotational frame of the reference states is performed, the absolute total states are corrected using the appropriated EoS, i.e., $s_{t,2} = f(h'_{t,2}, P'_{t,2})$ and $h_{t,2} = f(s_{t,2}, P_{t,2})$. The total-to-total isentropic efficiency is updated until convergence, finalizing the outer loop of the trailing edge iterative solution.

$$\eta_{t-t} = \frac{h_{t,2s} - h_{t,1}}{h_{t,2} - h_{t,1}} \tag{28}$$

in which $h_{t,2s} = f(s_1, P_{t,out})$ is the compressor outlet enthalpy due to an isentropic compression process. The impeller one-dimensional geometry is defined since all necessary inputs for the three-dimensional geometry construction tool (Ansys BladeGen) are estimated.

Figure 9 – Three-level impeller trailing-edge iterative solution.
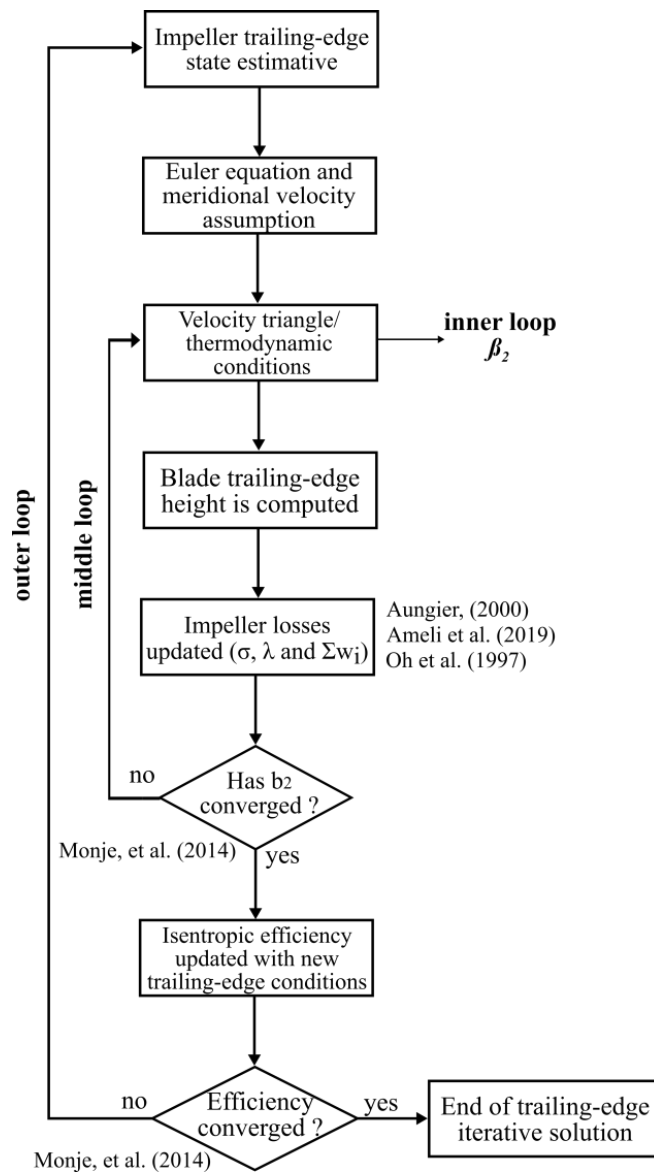
Fonte: Monje *et al.* (2014).

2.1.2 Vaneless Diffuser

In order to provide a suitable estimative of the losses due to vaneless diffuser (K_{dif}), this one-dimensional model uses the correlations presented by (OH; YOON; CHUNG, 1997). The impeller trailing-edge blade height is maintained along with the diffuser ($b_4 = b_3 = b_2$), as shown in Figure 10, and the thermodynamic state at the diffuser inlet is assumed equal to the impeller trailing edge.

Figure 10 – Impeller/Diffuser interface at the meridional view.
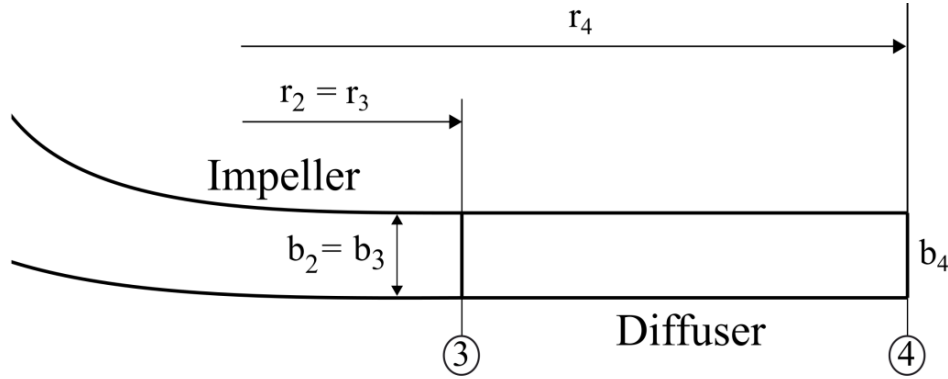
Source: Author.

An iterative solution is also required (Figure 11), and the diffuser exit radius (r_4) is initiated as equal to r_2 and incremented until the exit static pressure (P_4) is unchanged, meaning that the maximum possible pressure recovery is achieved by the vaneless diffuser.

$$\Delta h_{diff} = C_p T_{t,3} \left(\left(\frac{P_4}{P_{t,4}} \right)^{\frac{\gamma-1}{\gamma}} - \left(\frac{P_4}{P_{t,3}} \right)^{\frac{\gamma-1}{\gamma}} \right) \tag{29}$$

The vaneless-diffuser enthalpy loss calculation (STANITZ, 1952) is reevaluated until static pressure convergence and then K_{dif} is computed:

$$K_{dif} = 1 - \frac{P_{t,4}}{P_{t,3}} \tag{30}$$

Figure 11 – Diffuser iterative solution flowchart.
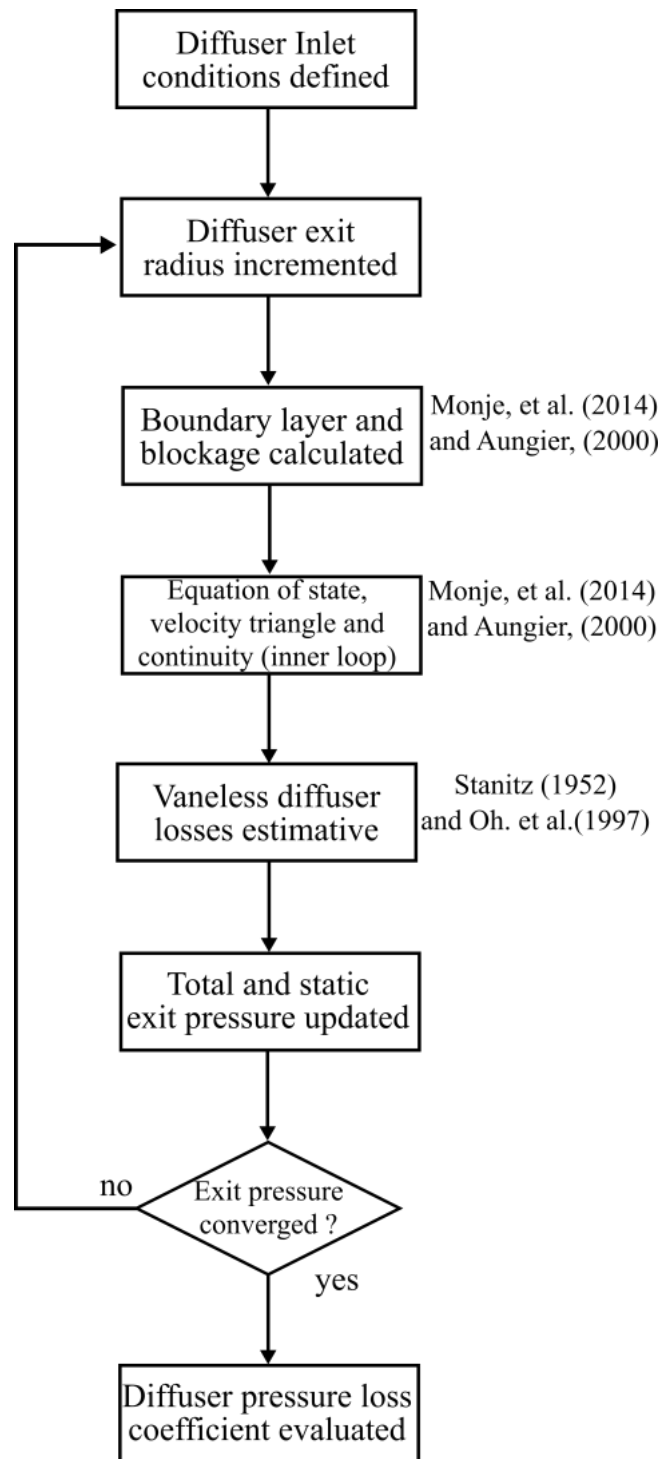
Source: Author.

2.1.3   Volute

The one-dimensional model for the volute is also based on Aungier (2000) and Monje *et al.* (2014). This modeling allows for calculating the total pressure loss coefficient (K_{vol}) needed for the solution of the whole compressor. The volute thermodynamic state and triangle velocity at the inlet is defined as equal to the diffuser outlet state. The iterative solution (Figure 12) is based on a sizing parameter (*SP*) target, defined between 1 and 1.2 (AUNGIER, 2000).

Figure 12 – Volute iterative solution flowchart.
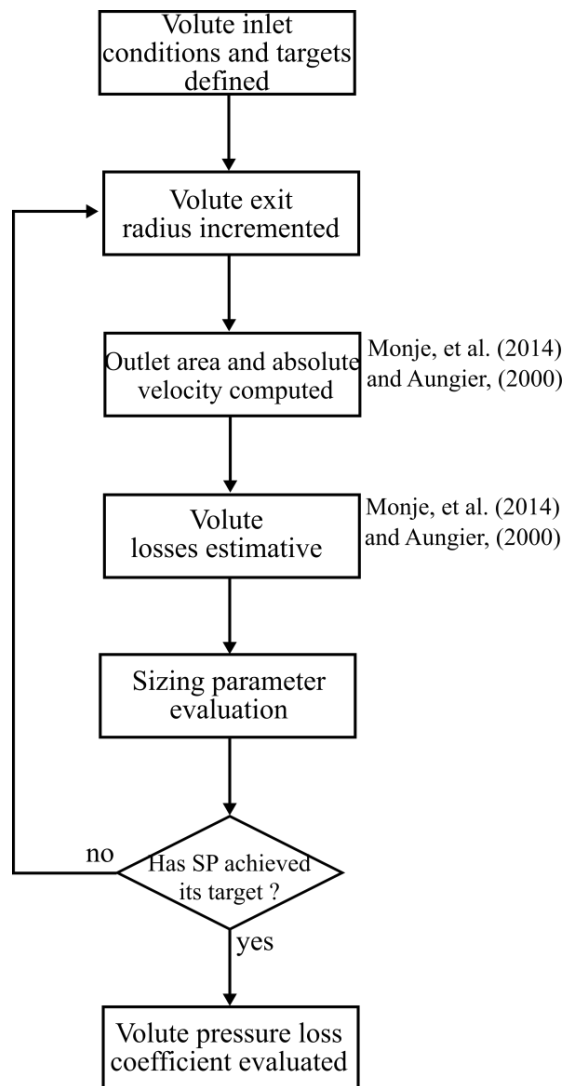
Source: Author.

$$SP = \frac{r_5 C_{U,5}}{r_6 C_{U,6}} \tag{31}$$

This procedure is repeated until the SP target is converged and, therefore, the total pressure coefficient (K_{vol}) of the volute can be performed:

$$P_{t,6} = P_{t,5} - (P_{t,5} - P_5)\sum_5^6 \overline{\omega}_i$$

$$\tag{32}$$

$$K_{vol} = 1 - \frac{P_{t,6}}{P_{t,5}}$$

Finally, the new estimative of total pressure losses ($K_{dif-vol}$) is taken to the impeller and the whole one-dimensional model is updated iteratively until losses and isentropic efficiency are converged.

2.1.4   1D model validation and calibration procedure

The available data on open literature related to CO_2 compressors under supercritical conditions for performing a proper validation of the code predictions was done by the assessment of the volute exit total pressure ($P_{t,6}$) using the experimental results from Wright *et al*. (2010). The code validation is conducted through comparison with '*Spin test 22*' and '*CBC_081202_1003 test*' data presented in Table 4.

Evidently, the errors on total pressure were less than 2% at the volute outlet, which validates that the predicted values of the 1D code, implemented in the present work, is similar to those reported by Wright *et al*. (2010). Moreover, four test points were reported in s-CO_2 power generation system of KAERI (CHA *et al*., 2021; PARK; CHA; LEE, 2022) and also were used for the assessment of the 1D model through total-to-total efficiency, as shown in Table 5.

Table 4 – One-dimensional code validation using total pressure.

Rotational Speed (n) [rpm]	Mass Flow ($\dot{m}$) [kg/s]	Inlet Pressure ($P_{t,in}$) [MPa]	Outlet Pressure ($P_{t,out}$) [MPa]		Error [%]
			Experimental (WRIGHT *et al.*, 2010)	1D Code (Present Work)	
29000	1.09	7.38	8.24	8.26	0.29
39000	1.50	7.51	8.96	9.00	0.46
49000	1.81	7.69	10.20	10.26	0.54
56000	2.04	7.76	11.24	11.31	0.64
60000	2.22	7.86	11.79	11.87	0.65
65000	2.40	7.96	12.55	12.64	0.69
55000	3.969	7.722	9.101	9.273	1.89
55000	3.719	8.067	10.135	10.283	1.46
55000	3.402	8.136	10.687	10.794	1.00
55000	2.540	8.170	11.583	11.683	0.86
55000	1.670	8.205	12.066	12.104	0.31

Source: Author.

Table 5 – One-dimensional code validation using compressor performance.

Rotational Speed (n) [rpm]	Mass Flow ($\dot{m}$) [kg/s]	Pressure Ratio (PR)	$\eta_{t\text{-}t}$ [%]		Diff. [%]
			Experimental (PARK; CHA; LEE, 2022)	1D Code (Present Work)	
34200	12.61	1.75	83.5	85.1	1.6
33000	12.13	1.68	83	84.7	1.7
33500	12.24	1.71	84.5	85.2	0.7
33000	12.76	1.73	84	85.2	1.2

Source: Author.

Considering the low differences reported on the validation tables presented herein, the 1D code could be considered validated for our purposes. Also, as will be seen, the CFD results corroborate the results of 1D model.

Figure 13 shows that the outputs of 1D model are inserted into Ansys BladeGen software to build a radial impeller and vaneless diffuser, in which the meridional profile and blade angle distribution along the compressor are set according to 1D Code outputs.

Figure 13 – Geometry construction and calibration procedure flowchart.
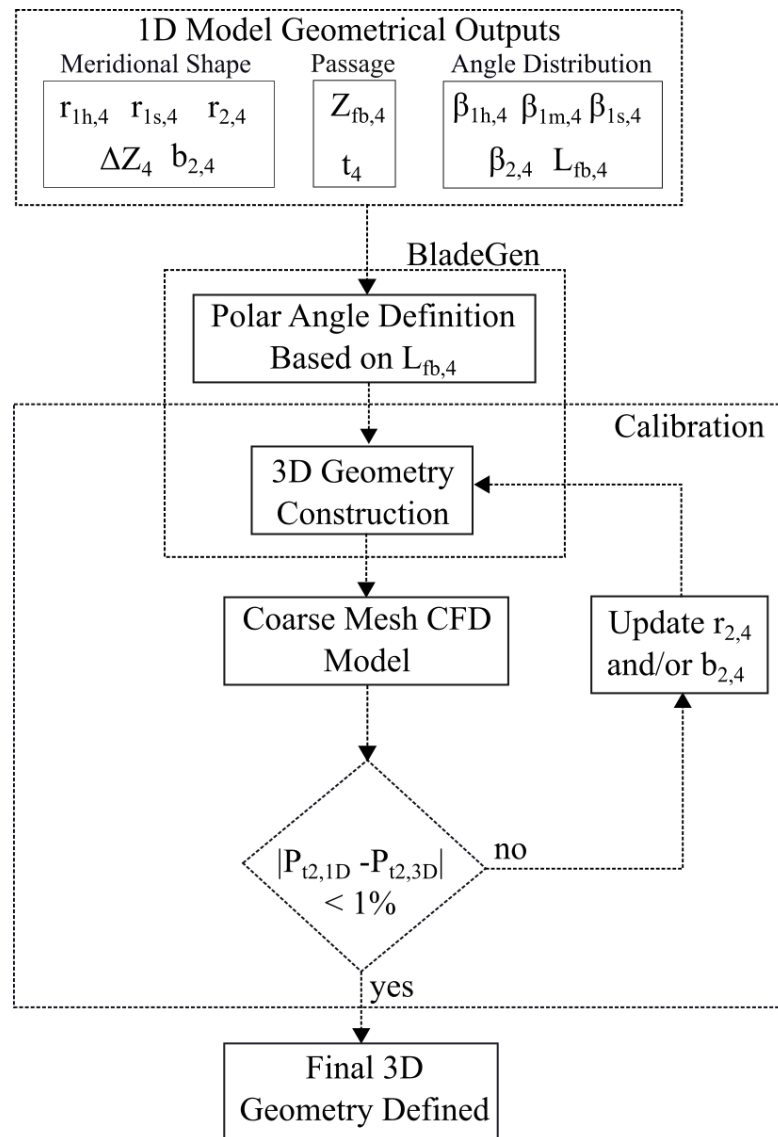
Source: Author.

The polar angle is defined by assessing which outlet angle would provide the 3D meridional blade length (L_{fb}) derived from the 1D Code. However, there are some differences between 1D and 3D models that are adjusted for the final geometry definition, which is known as 'Calibration Procedure' (YANG *et al.*, 2021) and shown in Figure 2.9. A preliminary CFD model is updated (small changes in r₂ and b₂) until the outlet total pressure meets the criteria $|P_{t2,1D} - P_{t2,3D}| < 1\%$. Finally, the 3D preliminary geometry obtained by the presented strategy can be taken to an SA and indirect optimization for further performance improvements in the equipment as will be discussed later.

2.2   Sensitivity analysis and response surface training for high-dimensional models

Associated with CFD optimization, the sensitivity analysis of engineering projects has become a popular tool to evaluate the variation of outputs by modifying the input variables (KLEIJNEN, 2009; XU *et al.*, 2019). In the design of a centrifugal compressor, outputs can change significantly depending on geometrical and operational design variables (BILAL, 2014). In this context, several sensitivity analysis methods and techniques have emerged to reduce the number of input variables reliably, allowing a faster and more assertive optimization procedure.

To ensure the reliability of SA, this work uses an approach (Figure 14) composed of two well-known methods: Morris' screening method (also known as the elementary effects (EE) method), which is computationally cheap and provides robust results for factor fixing purposes and SS-ANOVA method that provides representative sensitivity measures, allowing proper ranking of input design variables to better understand the physics of the dynamic flow. In order to save computational effort, the same DoE used in Morris' method can be used for RS training. After testing the RS reliability, a Uniform Latin Hypercube Sampling (ULHS)(MCKAY; BECKMAN; CONOVER, 1979) DoE could be generated to proceed with the SS-ANOVA method.

This strategy can reduce the computational cost of optimization procedures using Genetic Algorithms, which are known for providing suitable optimized cases for several engineering applications. On the other hand, gradient-based methods could be used for providing an optimized geometry using less model executions. Of course, these methods have much less potential for finding proper optimized geometries and were not considered herein.

Figure 14. Flowchart of the CFD, Sequential Sensitivity Analysis and Optimization methodology.
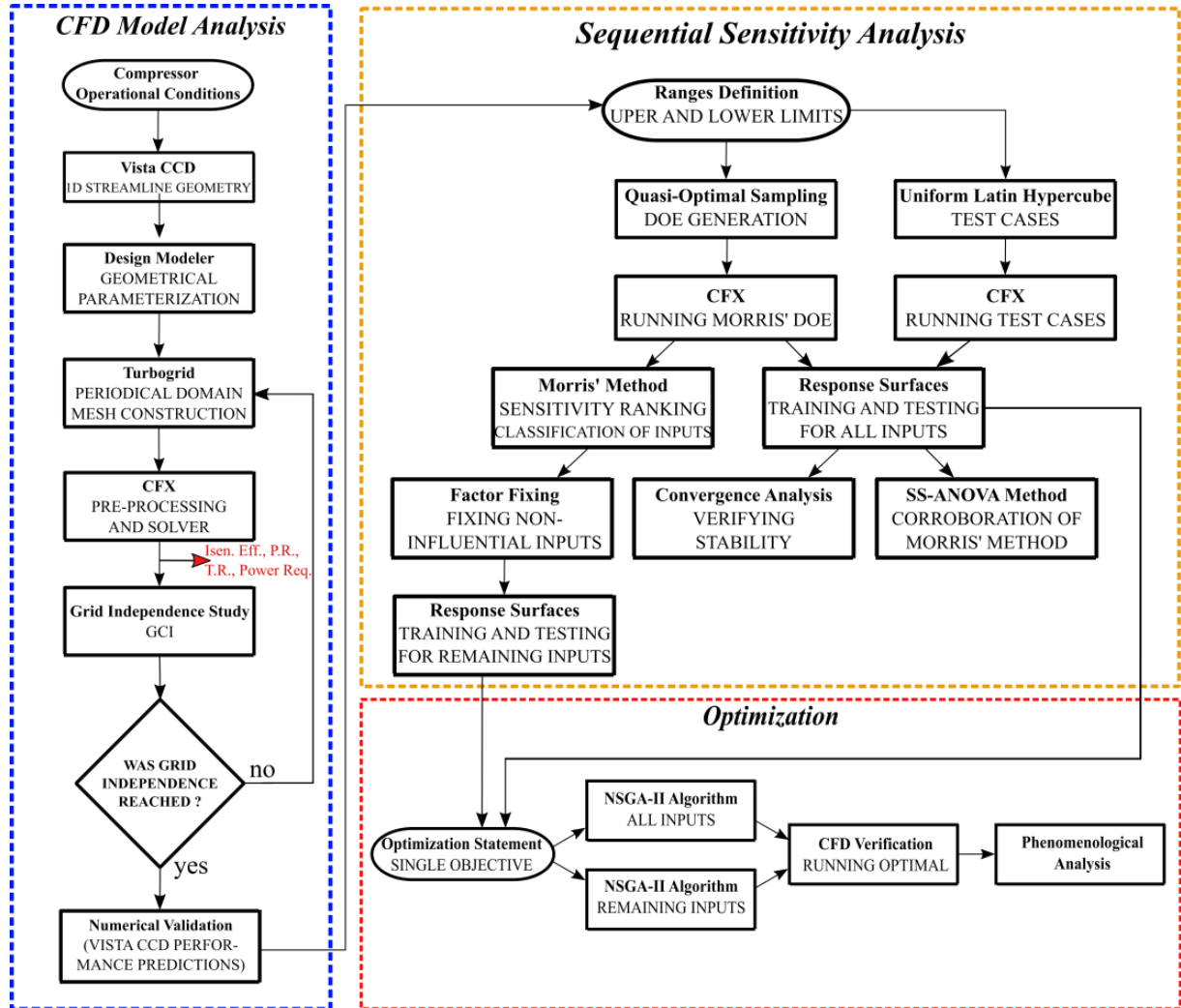
Source: Author.

Three different approaches were applied to analyze the problem (Figure 14): First, the CFD model was built based on a one-dimensional (1D) model that provided a preliminary impeller geometry to be imported by ANSYS Design Modeler software for the parameterization of geometrical variables. ANSYS Turbogrid software is used to build a periodical mesh domain. A grid independence study is performed following the grid convergence index (GCI) method (CELIK *et al*., 2008), which is a robust method to ensure mesh density analysis. The 3D CFD

results are then validated by comparison with the results provided by 1D predictions based on experimental values.

At the sequential SA step, the validated CFD model undergoes through the sequential sensitivity analysis starting by defining the input variability ranges. A quasi-optimal sampling (GE; CIUFFO; MENENDEZ, 2014) Design of Experiment (DoE) is built to provide adequate screening of the sample space for the Elementary Effect (EE) method (MORRIS, 1991) and also for RS training. Additional cases are created by uniform Latin Hypercube Sampling (LHS) method (MCKAY; BECKMAN; CONOVER, 1979) for RS testing. Morris' sensitivity measures were taken for factor fixing, which can eliminate non-influential input variables. Thus, a quantitative sensitivity analysis method (SS-ANOVA (GU, 2002)) and a convergence study (VANROLLEGHEM *et al*., 2015) can be fulfilled through response surfaces. The results of SA are used to identify physical phenomena responsible for diminish the machine's efficiency and the impact of geometrical design variables on those phenomena, which can improve the performance of the equipment.

Finally, at the optimization step, the response surfaces trained with the input variables classified as important were used to perform a single objective optimization using the Non-dominated Sorting Genetic Algorithm (NSGA-II) (DEB *et al*., 2002), aiming to maximize objective functions under several constraints. To verify the quality of the factor fixing procedure, the RS trained with all input variables are submitted to the same optimization procedure. The different optimized geometries were verified by the CFD model and the improvements in compressor phenomenology were discussed in detail.

2.2.1 *The elementary effects method*

Morris (1991) developed a sensitivity analysis method to determine which input variables would have important effects on the output variables. This method is known as the elementary effects (EE) method and is recognized as a simple but effective method of screening a few input variables among the many that can be contained in a model. If a model has k independent inputs $X_i, (i = 1, .., k)$, for a given value of X, the elementary effect is defined by Eq. (33).

$$EE_i = \frac{Y(X_1, X_2, ..., X_i + \Delta, ..., X_k) - Y(X_1, X_2, ..., X_k)}{\Delta} \tag{33}$$

where: Δ is the step for the discretized input space of value 2/3 (which is a normalized step for the range of variation for each design variable).

Morris (1991) suggests sampling r elementary effects for each input variable by constructing r trajectories of $(k + 1)$ points in the input sample space. Thus, the total cost of the method is $r(k + 1)$, which is relatively cheap compared to quantitative methods. The purpose of using the EE method is to determine which input variables may be considered negligible, linear and additive, or non-linear and involved in interactions with other factors. To obtain this information, two sensitivity measures were proposed, the average of each input EE distribution (μ), which assesses the overall influence of the variable, and the deviation of each input EE distribution (σ), which estimates the interactions with other factors. These two design variables are calculated according to Eq. (34) and Eq. (35), respectively.

$$\mu_i = \frac{1}{r}\sum_{j=1}^{r} EE_i^j \tag{34}$$

$$\sigma_i = \frac{1}{r-1}\sum_{j=1}^{r}(EE_i^j - \mu_i)^2 \tag{35}$$

Campolongo *et al.* (2007) proposed a revised version of the measure μ, called μ^*, that can provide a reliable ranking of variables. The parameter μ^* (Eq. (36)) is the average of the EE distribution in absolute values, solving the problem of effects having opposite signs, which occurs when the model is non-monotonic.

$$\mu_i^* = \frac{1}{r}\sum_{j=1}^{r}\left|EE_i^j\right| \tag{36}$$

The use of μ^* is convenient as it solves the problem of failing to identify a variable with considerable influence on the model, this can occur due to positive and negative effects canceling each other out when computing μ (SALTELLI *et al.*, 2008). Campolongo *et al.* (2007) also proposed an improvement to the sampling strategy that aims for better scanning of the input domain without increasing the needed number of model executions. The r trajectories were selected in such a way as to maximize their dispersion in the sample space. First, it generates a

high number of Morris' trajectories ($M = 500 \: to \: 1000$) and then it selects r trajectories with the highest 'spread', based on the following definition of 'distance' (d_{ml}) between a couple of trajectories m and l:

$$d_{ml} = \begin{cases} \sum_{i=1}^{k+1} \sum_{j=1}^{k+1} \sqrt{\sum_{z=1}^{k+1} \left[X_i^m(z) - X_j^l(z) \right]^2}, & m \neq l \\ 0, & otherwise \end{cases} \qquad (37)$$

where: k is the number of input variables and $X_i^m(z)$ indicates the zth coordinate of the ith point of the mth Morris' trajectory. Thus, it considers the quantity D for each possible combination of r trajectories, which is the quadratic sum of all the distances between couples of trajectories belonging to that combination. In other words, it selects the combination of r trajectories with the highest value of D. This sampling method is called optimal sampling as it checks all possible combinations of trajectories.

However, as the total number of combinations considered for an optimal approach is $M! / [r! (M - r)!]$, for high dimensional and large models, the combinatorial optimization problem makes the sampling process unfeasible for current computers. To overcome this problem, Ge *et al*. (2014) propose that instead of picking r optimal trajectories (OT) directly from the original set of M, the set of $(M - 1)$ trajectories with the highest total distance is picked first; in the second step, the set of $(M - 2)$ trajectories with maximum dispersion is chosen. The process is repeated until a set with only r trajectories is left. These r trajectories are called quasi-optimal trajectories (quasi-OT). The total number of combinations considered in this approach is $(M + n)(M - n + 1)/2$. Validation tests indicate that quasi-OT are very close to OT sampling and ensures that the quasi-OT approach can identify influential design variables from a complex simulation model with accuracy (GE; CIUFFO; MENENDEZ, 2014).

To fix non-important factors, model input variables need to be classified. Vanrolleghem *et al*. (2015) proposed terminology for the classification of variables as important/non-important and influential/non-influential using the EE method. A cut-off threshold could be determined, distinguishing three different types of variables concerning the absolute mean (μ^*) and the standard deviation (σ) of the sensitivity measure. In Figure 15, the line corresponding to $\mu_i^* = 2SEM_i$, where SEM_i represents the standard error of the mean which is used to establish the types

of variables (MORRIS, 1991). SEM_i is equal to $\sigma_i r^{-1/2}$, where r is the number of repetitions. Variables that lie outside the wedge formed by the line corresponding to the established CT_{Morris} and the line $\mu_i^* = 2SEM_i$, have a linear effect on the model outputs. Otherwise, the variables that lie inside this area have a non-linear effect.

Figure 15 - Differentiation of variables of the Morris screening method.
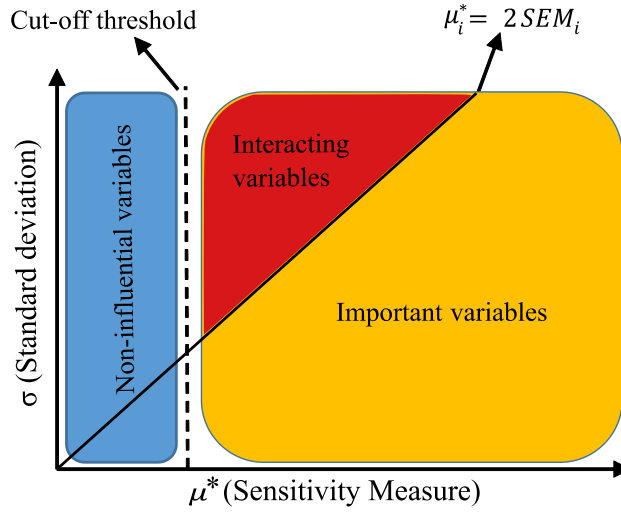
Source: Vanrolleghem *et al*. (2015).

To classify the model input variables in this work, the cut-off threshold for the Morris screening method (CT_{Morris}) was defined as the value of μ^* that takes into account more than 80% of the variations of the output. Thus, the important factors are those that have $\mu_i^* > CT_{Morris}$, the interacting factors have $\mu_i^* > CT_{Morris}$ and $\sigma_i > \mu_i^*\sqrt{r}/2$ while the non-influential factors have $\mu_i^* < CT_{Morris}$. Finally, to ensure the reliability and robustness of the EE method, a convergence study was performed. The methodology of convergence analysis proposed by Vanrolleghem *et al*. (2015) was performed by increasing the number of model executions until there was no significant change in the sensitivity measure. However, for large CFD models, this may be too time-consuming or prohibitive. Thus, the RS trained for the SS-ANOVA method has also been used to evaluate the EE convergence study.

2.2.2 Smoothing spline ANOVA (SS-ANOVA)

After screening and selecting the most influential variables, a quantitative sensitivity analysis was conducted with less computational costs, which relies mainly on how many variables remain from screening and how computationally expensive the numerical model is. If it is determined that a direct quantitative SA may become unfeasible, a surrogate model is used.

After training and testing a surrogate model, SS-ANOVA implemented in ModeFRONTIER software (GU, 2002) was chosen as a quantitative SA tool. Usually, the computation cost for smoothing splines analysis is k^3, where k is the number of input variables. This statistical modeling algorithm, based on classical analysis of variance (ANOVA), works with the decomposition of main effects and two-variable interactions, measuring the percentage of its contribution to the global variance (RIGONI; RICCO, 2011), defined by Ratto and Pagano (2010) as:

$$f(X) = f_0 + \sum_{j=1}^{n} f_j(x_j) + \sum_{j<i}^{n} f_{j,i}(x_j, x_i) \tag{38}$$

where the procedure developed by Kim and Gu (2004) is adopted, in which a more scalable computation of smoothing spline regression is used. SS-ANOVA decomposition can be built as a minimization of the usual least square functional (estimates the fitness of the model f) subjected to the constraint J (controlling the smoothness of the model and avoiding overfitting). The contribution indices (π_k) of each variable is defined as:

$$\pi_k = \frac{f_k^T \cdot \sum_{j=1}^{n} f_j}{\left(\sqrt{\sum_{j=1}^{n} f_j \cdot \sum_{j=1}^{n} f_j}\right)^2} \tag{39}$$

in which f_k^T is the column vector with lines representing variables individual decompositions and $\sum_{j=1}^{n} f_j$ is the summation of all sampling points decompositions. As π_k can be interpreted as the percentage decomposition of model's variance, the difference between the individual contribution summation and the unity represents the summation of all interaction effects (RIGONI; RICCO, 2011).

2.3   Three-dimensional CFD models for CO$_2$ centrifugal compressors

Two different centrifugal compressor's CFD models were constructed. Initially, the first stage of compression was considered to gain experience on centrifugal compressor modeling and to evaluate the developed low-cost SA methodology for large CFD models. Then, in order to attend one of this work goals and operate at the supercritical region of CO$_2$, the last compression stage model was developed working with s-CO$_2$ and a high number of variables (25 on total). Benini *et al*. (2006) suggest the use of a steady-state flow model for impellers since fluctuations in the flow of a centrifugal compressor are important only at the impeller vanned-diffuser gap, which is not verified for the impeller vaneless-diffuser evaluated herein. Furthermore, flow has high three-dimensional fluctuations, using CO$_2$ as a working fluid modeled by Redlich-Kwong for a real gas Equation of State (EoS) modified by (AUNGIER, 1995) in the first stage model and the (R.SPAN; W.WAGNER, 1994) in the last stage, since each EoS is better indicated for each region of compression considered. Hence, for a rotating domain, continuity, *momentum* and energy equations are given by:

$$\nabla \cdot (\rho U) = 0 \tag{40}$$

$$\nabla \cdot (\rho U \otimes U) = -\nabla p + \nabla \cdot \tau + S_M \tag{41}$$

$$\nabla \cdot (\rho U I) = \nabla \cdot (\lambda \nabla T) + \nabla \cdot (U \cdot \tau) + U \cdot S_M + S_E \tag{42}$$

which are solved by the finite volume-based commercial software ANSYS CFX 19.0, where τ is the stress tensor and the turbomachinery rotation terms such as centrifugal forces (S_{cfg}), Coriolis acceleration (S_{cor}), relative velocities and rothalpy (I) are taken into account by the rotating frame of reference (RFR) equations of ANSYS CFX®, as:

$$S_M = S_{M,rot} = S_{cor} + S_{cfg} \tag{43}$$

$$S_{cor} = -2\rho \left(\omega \times U\right) \tag{44}$$

$$S_{cfg} = -\rho\, \omega \times (\,\omega \times r) \tag{45}$$

$$I = h_{stat} + 1/2\, U^2 - \omega^2 R^2 \tag{46}$$

The turbulence model used was k-ω shear-stress transport (k-ω SST), which switches from the classical k-ω model for the inner part of the boundary layer to standard k-ε for the outer part of the boundary layer and the free flow, accounting for the effect of turbulent shear stress (MENTER, 1994). These characteristics make this model more robust and accurate for applications with high adverse pressure gradients such as those in centrifugal compressors (ROBINSON *et al*., 2012), and therefore is widely used in centrifugal compressor's CFD models (AMELI *et al*., 2019; BOURGEOIS *et al*., 2011; KIM *et al*., 2010).

2.3.1   *CFD setup for the first-stage compressor*

In order to assess the sequential SA proposed, the first stage of the CO_2 centrifugal compressor geometry is built in ANSYS Vista CCD, since its EoS can attend thermodynamic state of the fluid passage through the entire impeller-vaneless diffuser which is used as starting point for three-dimensional geometry (Figure 16a). Due to the periodic characteristics and geometrical symmetry, only one periodical part of the impeller-vaneless diffuser was computed (Figure 16b) and the results were extrapolated to the remainder of the turbomachinery, decreasing the number of elements on the total grid and, consequently, the computational cost.

The impeller part of the periodic domain was treated by the rotating frame of reference implemented in the ANSYS CFX solver as detailed in equations (40) to (46) and the diffuser was treated as a stationary frame of reference, which requires a domain interface modeling known as Multiple Frames of Reference (MRF) to couple both parts of the solution. This method is based on the General Grid Interface (GGI) connection, present in the stage mixing plane model that uses a circumferential average of fluxes on the interface and then obtains steady state solutions for each frame of reference. This interface model is successfully used on centrifugal compressors steady state solutions (ROMEI; GAETANI; PERSICO, 2022).

Figure 16 - Three-dimensional shape of CO2 centrifugal compressor impeller and diffuser (a) and the periodic computational domain (b).

(a)　　　　　　　　　　　　　　(b)
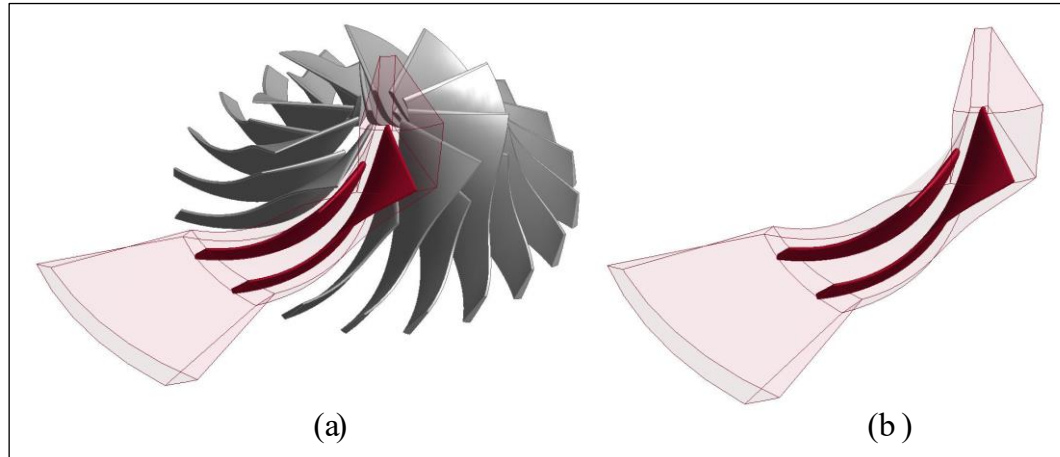
Source: Author.

A steady-state, three-dimensional, and turbulent flow of CO_2 was assumed and the walls were considered smooth and adiabatic with no-slip conditions. Table 6 summarizes the main boundary conditions applied to the pre-processing setup and some geometrical features of the rotor.

Table 6 - Boundary conditions and geometrical features.

Rotation speed	12500 rpm
Mass flow rate	55.56 kg/s
Machine's Mach number	1.26
Inlet pressure	400 kPa
Inlet temperature	320 K
Inlet turbulence	5%
Clearance gap	1 mm
Wall condition	No-slip
Roughness	Smooth
Number of blades	10
Impeller exit diameter	529.3mm

Source: Author.

There are operational conditions defined by design requirements, as the mass flow rate and thermodynamic inlet conditions. On the other hand, some of them are consequence of the 1D

optimization performed, allowing fluid flow constraints to be attended, such as the rotational speed, Mach number, number of blades and rotor exit diameter. The clearance gap is the spanwise distance between the blade and the shroud wall, highlighted in green on the top of the blade in Figure 17, which is present along the streamwise length. Rotational periodic surfaces were determined for the extrapolation of the symmetric part. The inlet is provided with static pressure and the outlet with mass flow rate, ensuring the compression ratio calculated is a consequence of simulation.

Figure 17 - Boundaries of the impeller-vaneless diffuser for a CFD periodic domain
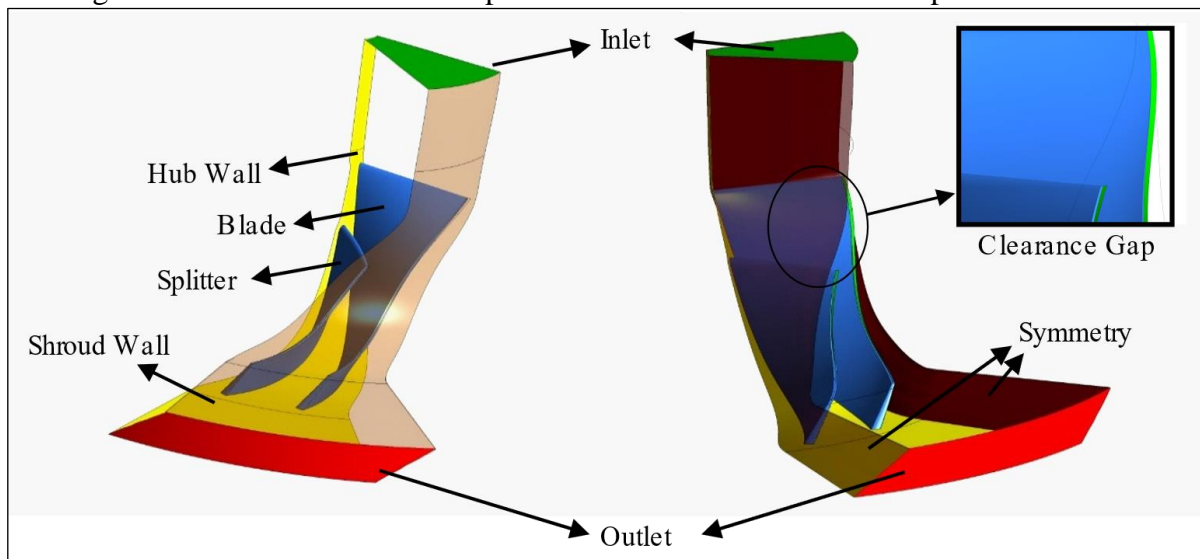
Source: Author.

2.3.1.1 Geometry Parameterization

The geometry of the impeller-vaneless diffuser was parameterized through ANSYS Blade Editor software, which is a free-hand tool that facilitates the generation of different blade models for turbomachinery through design variables such as blade streamline angles, thicknesses, and meridional shape. To proceed with the sensitivity analysis, the geometrical parameterization of the input variables was implemented, which allows the geometry to automatically change along the DoE. The meridional view of the blade presented in Figure 18a, has a purple and green line representing the leading edge and the trailing edge of the blade, respectively, while the other lines represent the fluid passage domain. The hub and shroud polar angles are a function of their

streamwise position (leading edge to trailing edge). Therefore, four points equally spaced in each layer referencing the variables in the stream direction were parameterized, as shown in Figure 18b.

Figure 18 - Meridional view of the fluid-flow domain (a) and angles along the stream (b).
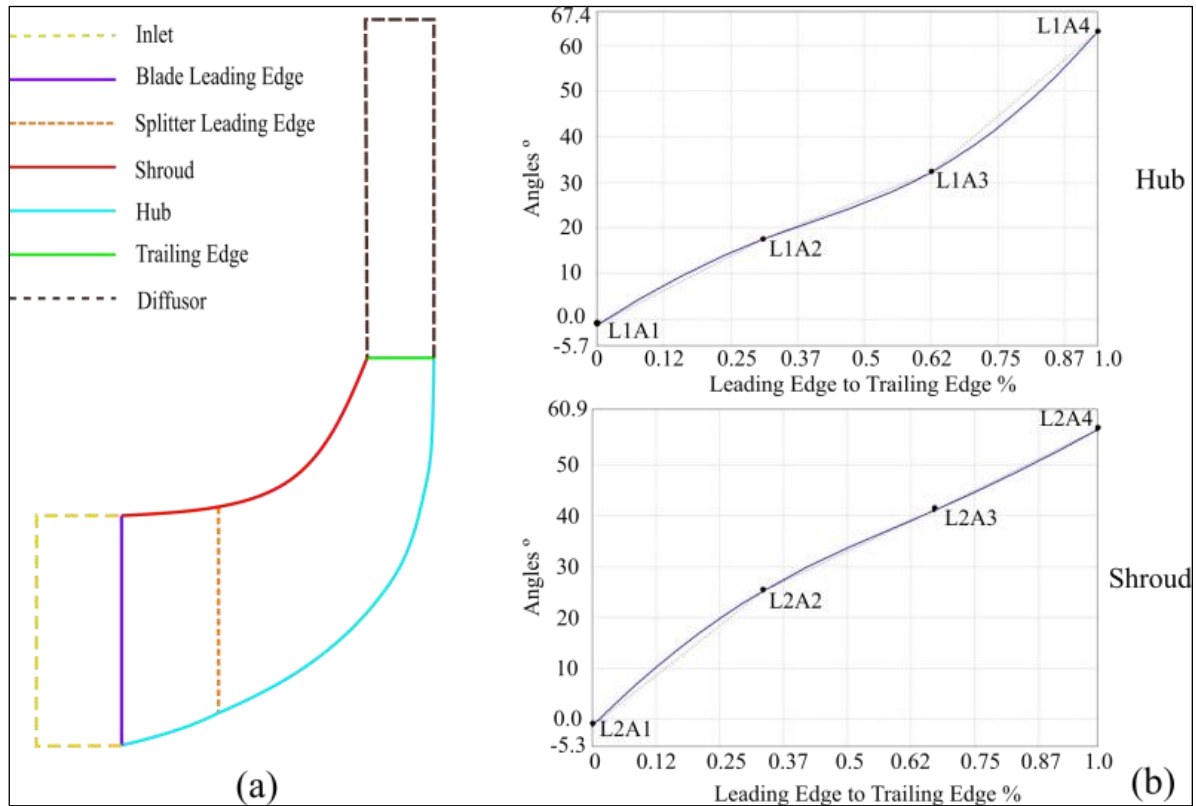
Source: Author.

The angles for each of these points vary only in the y-axis (angle value) of Figure 18b, allowing an independent change of the polar angles at the hub and shroud layers. Overall, eight variables were parameterized to be changed during sensitivity analysis and optimization procedures. They were denominated in the format L_xA_y, in which x is the spanwise layer of the variable, 1 for the hub and 2 for the shroud; and y is the angle streamwise position, 1 for the inlet, 2 and 3 for the middle positions, and 4 for the outlet.

The one-dimensional analysis takes into account the leading-edge blade angles of the hub and shroud, as well as the back sweep and rake angles but does not consider polar angles at intermediate positions of the blade (A2 and A3). Therefore, the 3D CFD model in the present

work could not be assessed by one-dimensional analysis, providing flexibility for the analyst to explore additional optimization options.

2.3.1.2 Mesh quality criteria

The computational domain discretization may impair convergence and accuracy. The commercial software, ANSYS Turbogrid, was chosen for this task as it has been successfully used for turbomachinery design, proving to be robust and fast (KULKARNI; BEACH; SKOCH, 2013; MONJE *et al*., 2014). Four criteria to ensure the mesh quality were analyzed: orthogonal angle, expansion factor, aspect ratio, and y^+. Figure 19a shows the entire mesh domain with near-wall refinements. Only 4.7% of the elements have an aspect ratio above the suggested level (lower than 1000) as highlighted in red in Figure 19b. The expansion factor and orthogonal angle met specifications. An automatic near-wall treatment applied in regions where the value of y^+ was greater than one was implemented by Knopp *et al*. (2006) and Menter (2009). The researchers claim that these equations help the turbulence model find accurate results, even with the condition of low near-wall distance not being fulfilled. Their approach suggests the results are reliable for values of y^+ up to about 10 for the k-ω SST turbulence model.
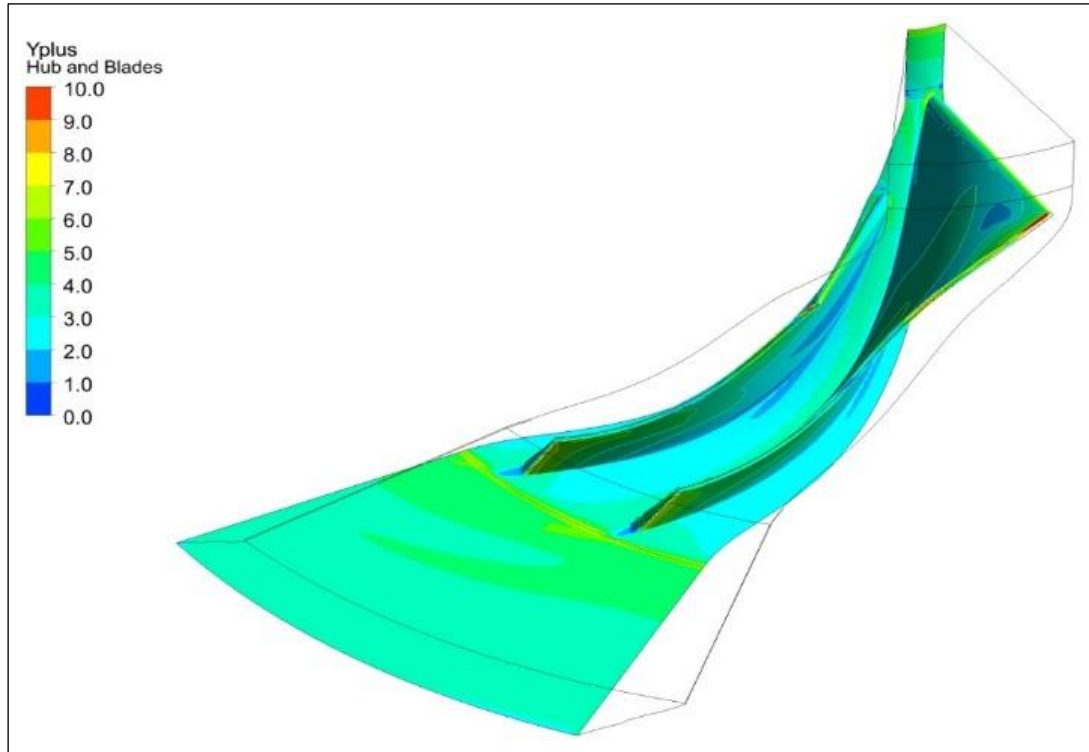
Figure 19 - Meshed domain with high aspect ratio elements for the medium grid
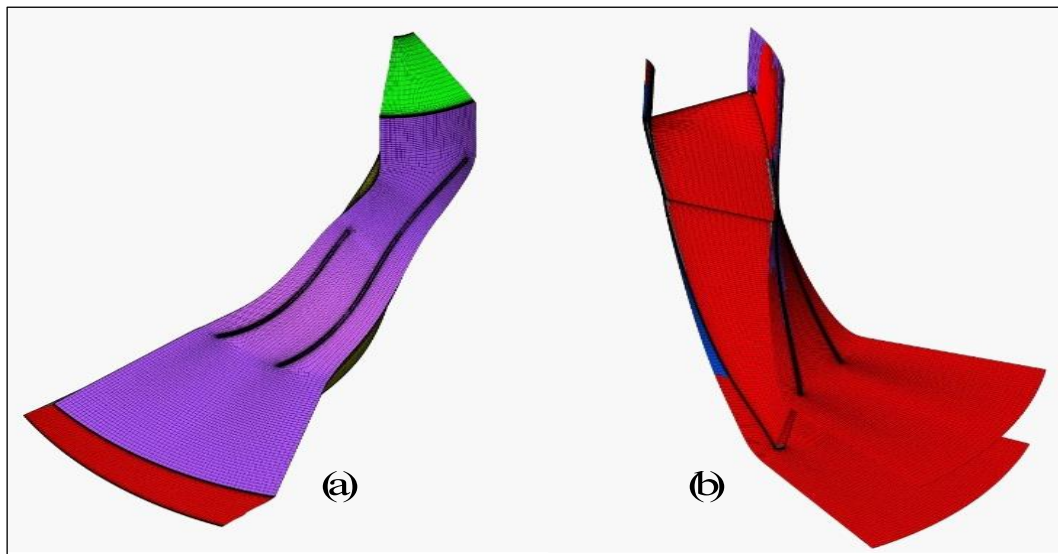
Source: Author.

Figure 20 shows the y$^+$ values of the elements, where only 0.34% of the mesh elements of the impeller-vaneless diffuser present y$^+$ higher than 10, which is considered satisfactory for the present work.

Figure 20 - y$^+$ quality criteria for k-ω SST – turbulence model

Source: Author.

2.3.1.3 Grid independence study

Grid convergence index (GCI) is an acceptable and recommended method that compares three mesh densities. Three grids based on this approach were created and their features are shown in Table 7. Notice that the refinement factors, r, are greater than or equal to 1.3 as recommended by Celik *et al*. (2008). Thus, the procedure to determine the GCI for polytropic efficiency, pressure ratio, the power required and temperature ratio could be applied. The results presented in Table 7 demonstrate that numerical uncertainties were very small which indicates that the grid independence is reached, and the medium grid can be used for this research.

Table 7 - Main results for the GCI method

	Coarse grid	**Medium grid**	**Fine grid**
Cells number, n	1.337×10^6	2.967×10^6	6.538×10^6
Refinement factor, r	-	1.31	1.30
	Polytropic efficiency	Pressure ratio	Temperature ratio	Power Required.
GCI$_{32}$ (%)	**0.0017**	**0.2238**	**0.6291**	**0.9850**

Source: Author.

2.3.1.4 Numerical validation

Due to the lack of experimental data for CO_2 centrifugal compressors working at the operating conditions specified in this study (Tables 4 and 5), the one-dimensional approach by (CASEY; ROBINSON, 2008b) was used for validation purposes. Their 1D streamline curvature method has demonstrated extremely good agreement with the 3D CFD method and their efficiency prediction equations (CASEY; ROBINSON, 2013) were consistent with more than 45 different experimental compressor stages with typical efficiency errors in the range of ±2%. They argue that, as their method uses non-dimensional performance coefficients and specific experimental data, it can be adapted to several gases (including CO_2) and applications. Table 8 presents the results of Casey and Robinson's equation predictions using ANSYS Vista CCD software compared to the CFD medium grid results of the present work. results are quite similar and the model is considered reliable.

Table 8 - Numerical validation results

Model	Polytropic efficiency	%	Pressure ratio	%	Power required (MW)	%
VISTA CCD (Casey and Robinson 1D)	86.40%	-	2.85 (input)	-	4.71	-
3D CFD medium grid (Present work)	85.41%	1.14	2.89	1.4	4.77	1.27

Source: Author.

2.3.2 CFD setup for the fourth-stage compressor

A 3D numerical simulation is performed for the 4th compression stage to evaluate the optimized geometry found by optimization of the compression system through the implemented 1D model and the geometry is adjusted by the calibration procedure. On this last stage compressor, the constraints AMC and GBM are critically close to the saturation and Widom-line (Figure 2). The preliminary geometry parameter values are presented in Table 9.

The CFD model can characterize the main dynamic flow phenomena such as turbulence, backflow and vortical structures (SUNDSTRÖM; SEMLITSCH; MIHĂESCU, 2018). Similarly, as presented in section 2.3.1, the commercial software ANSYS Turbogrid and CFX were used for mesh construction, boundary conditions and solver setup through the Finite-Volume Method (FVM) Methodology.

Table 9 – Preliminary geometry design variables values of fourth stage compressor

Geometrical design variables	Values
Inlet Hub Radius ($r_{1,h}$)	17 mm
Inlet Shroud Radius ($r_{1,s}$)	46.3 mm
Inlet Blade Angle at Hub ($\beta_{1,h}$)	31.58°
Inlet Blade Angle at Midspan ($\beta_{1,m}$)	48.93°
Inlet Blade Angle at Shroud ($\beta_{1,s}$)	59.24°
Inlet Polar Angle (θ_1)	0°
Outlet Radius (r_2)	132.2 mm
Outlet Height (b_2)	3.5 mm
Outlet Blade Angle (β_2)	-1.61°
Outlet Polar Angle (θ_2)	45°
Axial Height (ΔZ)	46.3 mm
Blade Thickness	2.5 mm
Full Blade Length	146.1 mm
Number of Blades	12

Source: Author.

The 3D numerical approach used herein is similar to our previous work (SALVIANO *et al.*, 2021). A steady-state and compressible flow is modeled with a linear-linear interpolation for diffusion terms, central differences for the pressure gradient term and the high-resolution second-order scheme discretization for advection terms of the coupled solver of CFX for the Reynolds-Averaged Navier-Stokes (RANS), using the $k - \omega$ SST turbulence model for closure. The Span and Wagner Equation of State (S&W EOS) of the sCO_2 through Real Gas Properties (RGP) table.

A periodical computational domain has been modeled as part of the whole compressor to save computational resources (Figure 21). The inlet boundary was set with constant static pressure and the outlet a constant mass flow rate, leaving the total-to-total pressure ratio and isentropic efficiency as a consequence of the converged solution.

Figure 21 – Compressor periodical domain and boundaries.
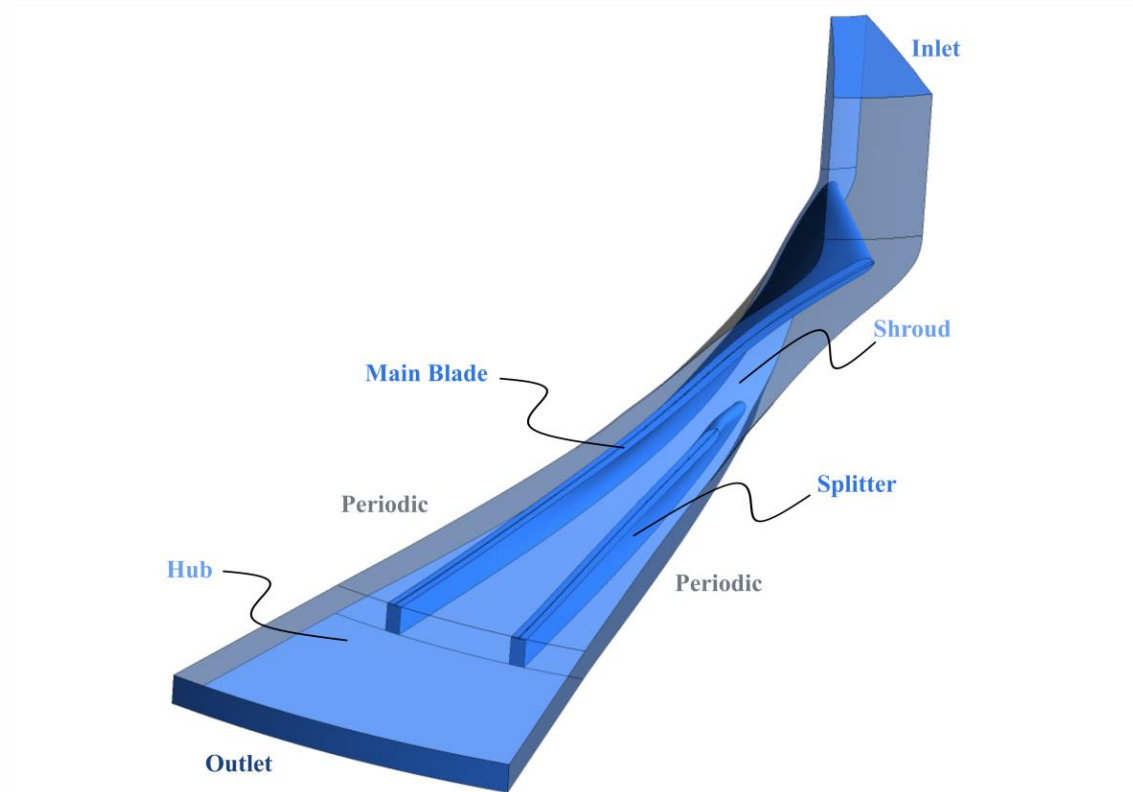
Source: Author.

Boundary and operational conditions are summarized in Table 10. Again, the walls were assumed as no-slip and smooth conditions since proper numerical validation was already performed using this setup (ALLISON *et al*., 2019; AMELI *et al*., 2018; HOSANGADI *et al*., 2018). The convergence criteria adopted are based on the Root Mean Squared (RMS) residuals of all equations and the average of the standard deviation of isentropic efficiency. The solver stops if RMS residuals reach 10^{-6} or if the standard deviation of the last 20 accumulated iterations reaches 10^{-4}.

Table 10 – Boundary and operational conditions for the fourth stage

Boundary/Operational Conditions	Values
Rotational speed*	19540 rpm
Mass flow rate	55.56 kg/s
Inlet Pressure*	7.42 MPa
Inlet Temperature	313.2 K
Turbulence Intensity (Inlet)	5 %
Clearance Gap	3% of blade height
Walls Condition	No-slip and smooth

Note: * Defined from 1D optimization procedure.
Source: Author.

Moreover, a CFD optimization was performed on the fourth-stage compressor. The parameterization was conducted in the software Ansys Design Modeler. A total of 25 geometric design variables were chosen as inputs for the SA and optimization process. They can be divided into three major groups: polar angles, meridional profile and diffuser. The polar angles are assessed in three different layers in the hub-to-shroud direction. Each layer has four angles equally spaced on the streamwise position as in Figure 22. The angles at the leading edge are set equal on the three layers (L1A1 = L2A1 = L3A1) due to the geometry construction through 1D model that fixed the polar angles at the leading edge and modified the trailing edge polar angles until the blade length is satisfied. Therefore, the trailing edge angles are also equal (L1A4 = L2A4 = L3A4). Thus, considering the intermediate angles (L1A2, L1A3, L2A2, L2A3, L3A2 and L3A3), 8 polar angles are set as variables.

Figure 22 – Blade polar angles.
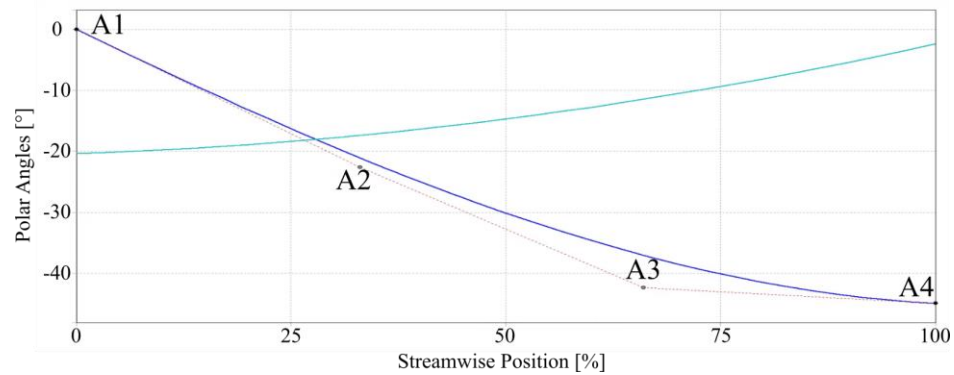
The meridional profile shown in Figure 23 presents 4 points for controlling the meridional profile through splines (P1, P2, P3 and P4). Each of these points has two degrees of freedom (X and Z), which results in 8 variables ($P1_x$, $P1_z$, $P2_x$, $P2_z$, $P3_x$, $P3_z$, $P4_x$, $P4_z$). Moreover, SP1 and SP2 are the streamwise positions of the splitter's leading-edge, completing 10 meridional variables.

Figure 23 – Meridional profile control points.
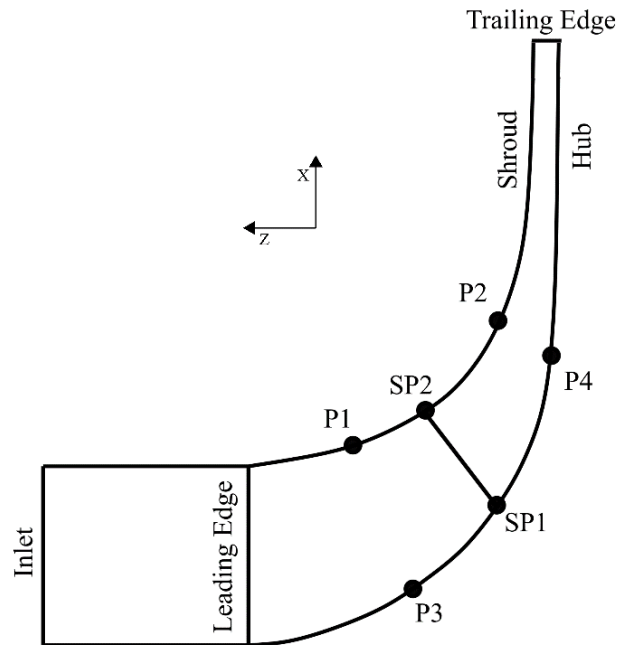
The last group of variables is related to the vaneless diffuser profile shown in Figure 24. Three points at shroud (S1, S2 and S3) and hub (H1, H2 and H3) are taken into only the Z-axis as the degree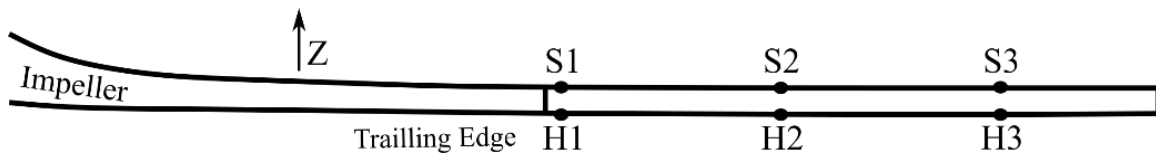 of freedom, resulting in 6 diffuser variables. At last, the blade-to-blade distance between the main blade and the splitter (POS) was taken for the analysis, completing the total amount of 25 geometry variables.

Figure 24 – Diffuser profile control points.

Source: Author.

The range of each variable is defined after a broad convergence study in which the CFD model was tested inside the sample space to identify the feasible range, as shown in Table 11.

Table 11 – Feasible range for each input variable

| Polar Angles			Meridional Profile			Diffuser		
Bounds	Lower	Upper	Bounds	Lower	Upper	Bounds	Lower	Upper
A1 [°]	-2	2	P1x [mm]	56.61	59.01	S1 [mm]	0.001	0.2
L1A2 [°]	-23.6	-21.6	P1z [mm]	12.27	14.67	S2 [mm]	2.68	4.73
L1A3 [°]	-43.3	-41.3	P2x [mm]	93.83	94.83	S3 [mm]	2.68	4.73
L2A2 [°]	-26.3	-24.3	P2z [mm]	4.05	5.05	H1 [mm]	0.001	0.2
L2A3 [°]	-45	-43	P3x [mm]	37.08	39.48	H2 [mm]	8.75	10.8
L3A2 [°]	-48.6	-46.6	P3z [mm]	6.79	9.19	H3 [mm]	8.75	10.8
L3A3 [°]	-45.3	-43.3	P4x [mm]	84.34	85.34	POS [%]	45	55
A4 [°]	-45	-42	P4z [mm]	0.12	1.12			
			SP1 [mm]	20.05	27.16			
			SP2 [mm]	23.42	25.63			

Source: Author.

The investigation of these groups of variables simultaneously, aims to understand their impact on one another (through SA) and on polytropic efficiency (through optimization). These variables are not present in the 1D model used to generate the original geometry. Therefore, there is an opportunity for improvement in these variables, the evaluation of Morris' SA methodology for a high number (25) of interacting variables, considering a CFD model of a centrifugal compressor of 3.4 pressure-ratio, low-flow coefficient, operating with s-CO2. The original CFD geometry is the last compression stage of an EOR system, a consequence of a 1D model that provided this preliminary geometry. The high-dimensional sequential SA combined with the 'entropy guided' phenomenology assessment can deliver important operational cost reductions to the EOR compression system, turning this CCUS technology even more advantageous.

2.3.2.1 Real Gas Properties (RGP) table resolution study and grid convergence index

The S&W EOS implemented from CoolProp library (BELL *et al*., 2014) was used to properly write a sCO_2 RGP file that could be read by Ansys CFX solver. Furthermore, a RGP Table resolution study was conducted to verify its influence on CFD results. Three different table resolutions were generated: 2K/0.2MPa; 1K/0.1Mpa; 0.5K/0.05MPa, within the same ranges (pressure from 1MPa to 101MPa and temperature from 240K to 1040K). No significant impacts on CFD results or processing time were noticed due to RGP Table resolution and, therefore, table resolution of 1K and 0.1 MPa was defined in further simulations.

Furthermore, the mesh of Figure 25 was submitted to an independent study using the Grid Convergence Index (GCI) methodology (CELIK *et al*., 2008) with wall functions to properly treat the near-wall fluid flow. As can be seen, the mesh refinement was focused mainly on walls (blade, splitter, hub, shroud and clearance gap).

Figure 25 – Finest mesh used for GCI and phenomenology assessment.
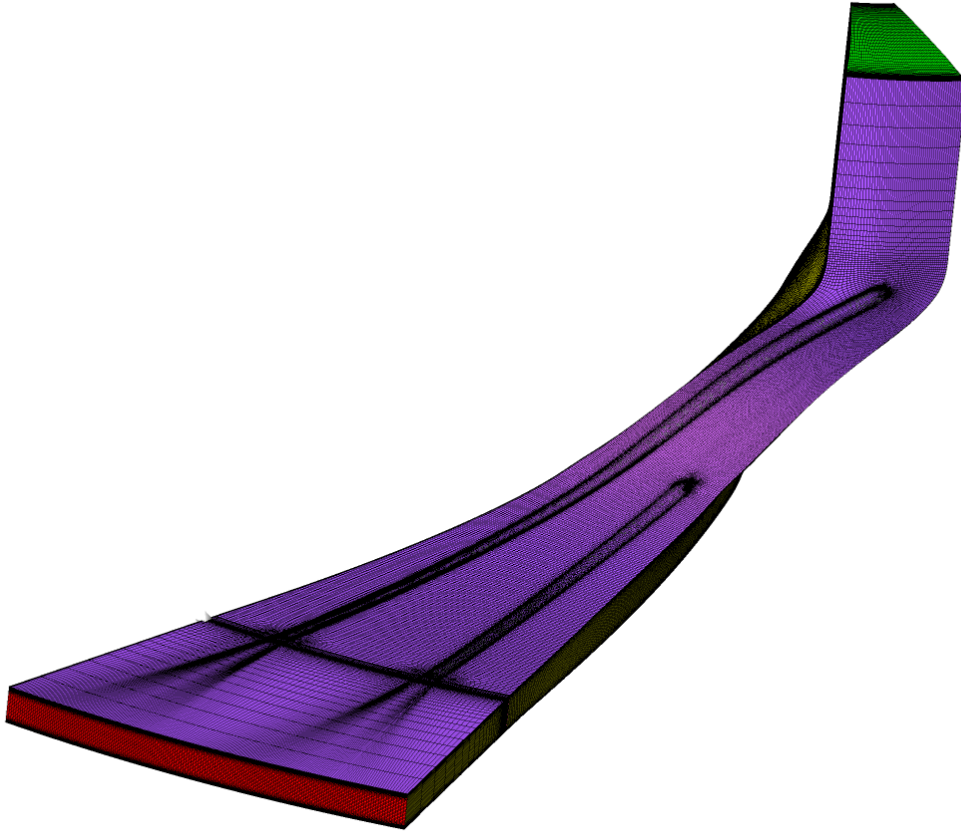
Source: Author.

Table 12 shows that the uncertainty due to grid density for the main output variables for the finest grid (GCI_{21}) is small enough for the present work. Of course, the meshes were refined through the global size factor of Ansys Turbogrid, ensuring well-distributed refinement.

Table 12 – Grid information and GCI results

Grid	Coarse	Medium	Fine	GCI_{32}	GCI_{21}
(Number of cells)	(702k)	(1640k)	(3709k)	(%)	(%)
Polytropic Efficiency (%)	82.73	82.80	82.84	0.263	0.093
Pressure Ratio	3.86	3.92	3.91	0.514	0.161
Power Required (MW)	3.83	3.80	3.84	0.369	0.216

Source: Author.

After ensuring CFD model quality for both centrifugal compression stages, different optimization goals were set. The first stage geometry was used to validate the strategy of using SA coupled with RS optimization while the fourth stage geometry was used to validate the design strategy of using the 1D model followed by the CFD analysis.

Finally, due to the lack of experimental results for s-CO_2 centrifugal compressors with the same operational conditions as the present work, the 1D code predictions are used for proper validation of the CFD model, as presented in Table 13. The 1D model used herein has already been validated using experimental measurements (WRIGHT *et al*., 2010). This approach was used since not enough geometrical information was available for direct CFD assessment of experimental compressors. The polytropic efficiency has shown a difference of only 0.3% and the model is considered validated, which is also valid for the 2% difference in PR since in absolute values it's a low difference (4 to 3.92). The almost 5% difference in required power is attributed to the better loss assessment of the CFD model since three-dimensional phenomena take into account a more complete physical model and also is considered suitable for the present work.

Table 13 – Validation of CFD model using 1D code

Variables	Polytropic Efficiency (Impeller)	%	Pressure Ratio (Impeller)	%	Power Required	%
1D Predictions	82.53 %	-	4.0	-	3.62 MW	-
CFD Results	82.80 %	**0.3**	3.92	**2.0**	3.80 MW	**4.97**

Source: Author.

2.4 Optimization strategy for one-dimensional s-CO2 EOR compression systems

The one-dimensional model implementation allowed a high number of variables to be inserted in the design procedure, which after a study of the whole compression system resulted in the 28 variables described in Table 14 with its respective ranges of variation. Overall, they can be divided in 4 operational variables (PR_i) and 24 geometrical variables. Of course, pressure ratios are essential for an optimization that aims to diminish the power required in the system. On the other hand, some geometrical variables may impact system performance through their influence

on fluid flow features that could turn the system unfeasible due to high Mach numbers, condensation or transcritical fluid behavior.

As matter of fact, the impeller variables as number of blades, splitter length, shroud radius and axial length should be investigated for their capacity to change fluid flow in the equipment's inlet and throat. Moreover, diffuser height was selected due to the possible flow recirculation on the impeller-diffuser interface. Finally, the volute sizing parameter was considered to complete the analysis since it's the most important variable for the last part of the machine that changes the flow direction.

Table 14 – Sensitivity analysis/optimization variables' ranges

Variables (i = 1—4)	First Stage		Second Stage		Third Stage		Fourth Stage	
	Lower	Upper	Lower	Upper	Lower	Upper	Lower	Upper
PR_i (Pressure Ratio)	1.8	3.7	1.8	3.7	1.8	3.5	1.8	4.4
$Z_{fb,I}$ (Number of Blades)	10	16	11	14	10	16	10	18
$L_{sf,I}$ (Splitter Length)	0.5	0.8	0.5	0.8	0.5	0.8	0.5	0.8
$r_{1s,i}$ [mm] (Shroud Radius)	160	192	96	120	66	72	43	48
$\Delta Z_{,i}$ [mm] (Axial Length)	90	310	86	110	38	66	28	44
$b_{4,i}$ [mm] (Diffuser Height)	12	45	6	40	4	20	1.2	6
$SP_{targ,I}$ (Volute Sizing)	1.01	1.5	1.01	1.5	1.01	1.5	1.01	1.5

Source: Author.

Evidently, these ranges are different for each variable due to 1D model feasibility, i.e., for a fixed specific diameter (D_s) and rotation (N_s), all variables were modified to obtain their minimum and maximum suitable values, which are defined by model convergence (PR, Z_{fb}, r_{1s}, ΔZ, b_4) or geometrical restrictions (L_{sf} and SP_{targ}). Therefore, the limits were set to respect physical instabilities predicted by the 1D model or space availability expected on the operational site. The shroud radius ranges for the third and fourth stages are much shorter than the first and second stages, which is due to the high impact of these variables on throat Mach number.

In order to decrease the optimization computational effort, the screening sensitivity analysis is conducted with factor fixing purposes to find non-important variables before the optimization procedure, which is detailed in Section 3. The SA methods were used to support the decision-making of factor fixing since the combination of several SA methods increases the robustness of

the factor-fixing task (GARCIA; AROSTEGUI; PRELLEZO, 2019). Therefore, only pressure ratios and shroud radius were considered in the optimization procedure.

The one-dimensional code for each compression stage was implemented in Python programming language, which allowed its scripts to be integrated with modeFRONTIER (mFR) software. mFR is a robust and powerful commercial software with several optimization methods.

2.4.1 *Optimization statement for the whole compression train*

Figure 26 shows the optimization workflow with those eight remaining variables defined by Sensitivity Analysis, its connections among stages, as well as the fluid flow constraints: Throat Mach number (M_{th}), Condensation (AMC) and Gas-like Behavior (GBM). The direct thermodynamic analysis of the compression system could lead to an unfeasible design since the condensation and significant changes in the fluid properties close to the Widom-line could not be modeled from the direct thermodynamic analysis. Thus, the inlet throat shockwaves and condensation gas-like behavior could be addressed by the optimization procedure which provides a completely feasible and reliable compression system.

Figure 26 – Optimization workflow applied to the compression train system.
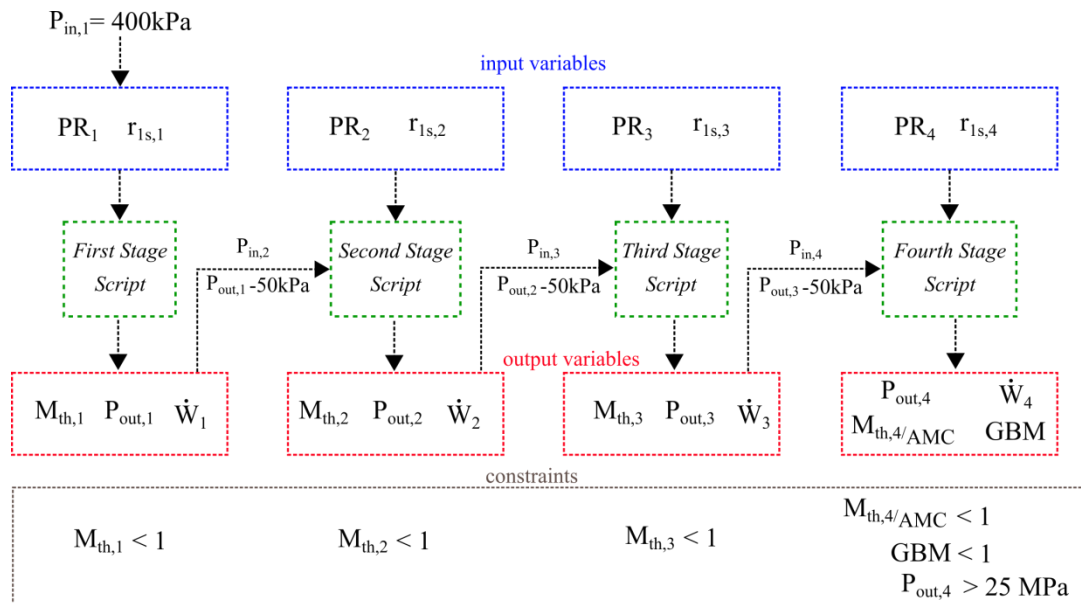
Source: Author.

The Non-Sorted Dominated Genetic Algorithm (NSGA-II)(DEB *et al.*, 2002) optimization method with a variable population size algorithm was used to minimize the total power consumption of the compression train. The crossover probability parameter is set by 0.9, which implicates that 90% of the new generation of design vectors are a result of the crossover process, that combines the old generation best fitted designs to create the offspring. Therefore, 9% of the new generation is result of the reproduction procedure, using the simple 'survival-of-the-fittest' principle. Moreover, the mutation probability is 0.01 which is responsible for ensuring random exploration of design vectors to accomplish a local search around the current solution using 1% of the offspring (RAO, 2009). Thus, the optimization statement of a single-objective function is defined as:

$$\text{Find } X = \begin{Bmatrix} PR_1 \\ PR_2 \\ PR_3 \\ PR_4 \\ r_{1s,1} \\ r_{1s,2} \\ r_{1s,3} \\ r_{1s,4} \end{Bmatrix} \text{ which minimizes } \sum_1^4 \dot{W}_i\,(X)$$

subjected to the constraints:

$$M_{th,1} < 1; M_{th,2} < 1; M_{th,3} < 1; \frac{M_{th,4}}{AMC} < 1; GBM < 1.$$

2.4.2 Optimization strategy of the CFD first-stage model through surrogate models

Two different approaches to CFD optimizations were utilized to evaluate the impact of factor fixing on the first stage of optimized design. First, an optimization procedure using eight blade polar angles as initial variables was performed, providing a comparison between the optimization considering only the blade polar angles identified as important. To be considered important, the input variable must be influential in at least one of the four interest outputs (polytropic efficiency, pressure ratio, outlet temperature, and power required). For instance, if a variable was identified as non-influential for pressure ratio calculations but important for polytropic efficiency, that variable was not excluded from the optimization procedure.

Despite the increase in computer capacities in the past few years, the optimization of large models could be prohibited due to high processing times and the number of input variables. To

overcome this problem, an approximation of the original model can be made with response surfaces (JENSEN; MAYORGA; PAPADIMITRIOU, 2015). This is achieved by performing only a few executions of the model and training a function that represents the original model. Optimization through RS has some advantages: faster realization of the model, less computer storage needed, and easier applicability to sensitivity analysis methodologies. However, some drawbacks reported are the inherent error from the original model and its incapacity to predict results outside its training/testing sets (VILLA-VIALANEIX *et al*., 2012). The validity and accuracy of a response surface should be assessed by the original model, evaluating the error of the training and test data.

2.4.2.1 Response surface methods (RSM) and Sequential sensitivity analysis for large models

For high-dimensional models, most efforts are spent on RS training. These efforts are generally dependent on the number of variables contained in the model. Besides, when the model itself is high-dimensional and the interactions among design variables are not negligible, the difficulty in achieving a well-fitted RS increases (GE; CIUFFO; MENENDEZ, 2014). The approach used for RS training is to take the simulations already performed to the quasi-optimal sampling DoE for screening analysis used in Morris' method, decreasing additional numerical simulation. The DoE size is dependent on the number of variables (k) and trajectories (r) in the sample space $(k+1) \times r$. This work has evaluated eight input variables (k = 8) and ten trajectories (r = 10) (SALTELLI *et al*., 2008), resulting in a total of 90 CFD simulations.

RS training was performed with the same DoE used for Morris' SA method, while the RS test was evaluated by 9 different CFD simulations (10% of the training cases) generated through ULHS (MCKAY; BECKMAN; CONOVER, 1979). The best-fitted RS for polytropic efficiency was achieved using the Stepwise Regression method, as shown in Table 15, in comparison with other well-fitted methods.

Table 15. Quality criteria of the response surface trained for polytropic efficiency

RS Method	R^2	Max. abs. error	Max. rel. error
Stepwise regression (RIGONI, 2014)	0.978	0.068	0.080
Radial basis function (RIGONI, 2007)	0.977	0.059	0.069
Smooth spline ANOVA (GU, 2002)	0.974	0.076	0.089
Kriging (RASMUSSEN; WILLIAMS, 2006)	0.959	0.069	0.081
Neural network (17 levels) (HAYKIN, 1999)	0.952	0.083	0.097

Source: Author.

Therefore, quasi-optimal sampling was responsible for the great accuracy of RS. The high-dimensional (more than 20 input variables) CFD model optimization of turbomachinery could become feasible if this sampling methodology was applied. Furthermore, Morris' method convergence study and SS-ANOVA method are only possible due to RS's great accuracy.

Table 16 shows the nominal, lower and upper values of the input variables. Several CFD model tests were conducted in order to determine the ranges of input variables. Many changes in polar angles were performed to assess the geometry/mesh generation and CFD model convergence. Thus, lower and upper limits were selected to ensure the geometry and mesh without errors as well as the CFD model convergence was properly achieved inside these limits.

Table 16 - Input variables range

Variable	Lower (degrees)	**Original (degrees)**	Upper (degrees)
L1A1	-1.25	**0**	1.25
L1A2	17.62	**17.98**	18.34
L1A3	32.71	**33.37**	34.04
L1A4	61.38	**61.69**	62.92
L2A1	-1.25	**0**	1.25
L2A2	25.23	**25.74**	26.26
L2A3	39.41	**40.21**	41.02
L2A4	54.60	**55.72**	56.83

Source: Author.

2.4.2.2 Optimization statement

After training the RS, an optimization approach was executed using the improved version of the non-dominated sorting genetic algorithm (NSGA-II) implemented in modeFRONTIER software, which is a computationally fast and elitist evolutionary algorithm that can maintain a good spread and convergence of solutions (DEB *et al.*, 2002; WANG *et al.*, 2011). The optimization statement is:

$$\text{Find } X = \begin{Bmatrix} L_1A_1 \\ L_1A_2 \\ L_1A_3 \\ L_1A_4 \\ L_2A_1 \\ L_2A_2 \\ L_2A_3 \\ L_2A_4 \end{Bmatrix} \text{ which maximizes polytropic efficiency } (X)$$

subject to the constraints:

$$Required\ power(X) \leq P_{Original} = 4.76MW$$
$$Temperature(X) \leq T_{Max} = 200°C$$
$$Pressure\ ratio(X) \geq PR_{Min} = 2.85$$

where L_1A_1 is the inlet polar angle at first layer (hub leading edge) and L_2A_4 is the trailing edge polar angle at shroud. $P_{Original}$ is the total power required by the original impeller, T_{Max} is the temperature limit so the intercooler between compression stages remains functional, and PR_{Min} is the pressure ratio, which is a requirement of the project.

2.4.3 Optimization strategy of the CFD fourth-stage model through surrogate models

The second approach of CFD optimization used the same SA strategy of the first-stage compressor but considering 25 variables to evaluate if interactions would impact the ability of SA to screen the sample space in such conditions. Furthermore, we seek to find an optimized solution at the gas-like side of the T-s diagram.

2.4.3.1 *Response surface methods (RSM) and Sequential sensitivity analysis for large and high-dimensional models*

The interesting output considered by the analysis was the polytropic efficiency of the equipment, which better represents the quality of the fluid flow inside the turbomachinery (AUNGIER, 2000). Table 17 presents the sampling strategy used to train the polytropic efficiency RS used for this high-dimensional problem, among the number of model realizations required and the RS method utilized with its quality measures. This work opted for combining a methodology of sequential screening SA (Salviano *et al.*, 2021) with Incremental Space Filler (ISF) sampling to provide well-fitted surrogate models for a set of 25 input variables, considering the impeller and vaneless diffuser, in which it became clear the Morris' method limitation in identifying interactions between variables properly.

Initially, 10 Quasi-Optimal Trajectories (Quasi-OT) were selected as it is common practice for Morris' method (SALTELLI *et al.*, 2008), which required 286 CFD simulations, including the test cases. Both, Morris' SA and RS training were performed with this initial assessment of the sample space. A sort of different RS methods was investigated without success in achieving good quality RS for proper model representation (the best fit was the Radial Basis Functions (RBF) presented in Table 17). In the attempt to improve RS quality, 6 extra Quasi-OT were added to the analysis, which required 172 extra CFD simulations. The SA and RS training procedure were repeated and no improvement in RS fitness was verified, as presented in Table 17, which demonstrates that increasing the Quasi-OT number does not improve the RS quality measures. This indicates an inability of Quasi-OT sampling to properly represent the sample space when a high number of interacting variables are present in the model, due to its one-at-a-time design of experiment nature (SALTELLI *et al.*, 2019).

Table 17 – Polytropic Efficiency RS training strategy and quality measures.

Sampling Strategy	CFD Model Runs	RS Methodology (Best fitted)	Regression Coefficient (R²)	Max. Abs. Error	Mean Rel. Error (%)
Quasi-OT Sampling (10)	260 + 26 ULHS (MCKAY; BECKMAN; CONOVER, 1979) for testing	Radial Basis Function	0.775	0.873	0.371
Quasi-OT Sampling (6)	156 + 16 ULHS(MCKAY; BECKMAN; CONOVER, 1979). for testing	Radial Basis Function	0.761	0.773	0.384
Incremental Space Filler	120 + 12 ULHS(MCKAY; BECKMAN; CONOVER, 1979) for testing	Evolutionary Algorithm	0.950	0.386	0.167
Total	**590**	**Evolutionary Algorithm**	**0.950**	**0.386**	**0.167**

Source: Author.

Therefore, an different sampling methodology was considered: the Incremental Space Filler (ISF), which added 132 additional CFD simulations and improved the RS training quality measures to acceptable values (MONTRONE *et al*., 2019), as evidenced in Table 2.15. Many efforts to develop and calibrate RS are dependent on the number of variables present in the model. High-dimensional models generally have interactions between variables, interfering with the achievement of a well-fitted RS (GE; CIUFFO; MENENDEZ, 2014). Therefore, the described approach that proposes to combine Quasi-OT and ISF can be a promising alternative to reduce significantly the number of cases required for good RS fitness, since only 24 model runs per parameter were necessary. Finally, the best-fitted method used for training the polytropic efficiency RS is known as Evolutionary Design (ED) (FILLON, 2008) was used and its quality criteria are also presented in Table 17.

Only a few executions of the model, with good sample space representation, could provide a function that represents the original model, grating faster realization, less computer storage needed and easier applicability to other sensitivity analyses. However, there is an inherent error in the original model and its incapacity to predict results outside its training/testing sample space (VILLA-VIALANEIX *et al.*, 2012). Once this well-fitted RS is properly trained, a variance-based SA method, the SS-ANOVA (GU, 2002) can be performed for interactions evaluation. This algorithm, based on classical analysis of variance, decomposes the main effects and the two-variable interactions, measuring the percentage of its contribution to the global variance (RIGONI; RICCO, 2011). The commonly estimated cost for this method is k^3, resulting in 15625 runs through the RS, which would be prohibitive to perform through the original CFD model. Moreover, the RS also permits to proceed with an optimization procedure. The validity and accuracy of the RS are assessed by the original model afterward.

2.4.3.2 Optimization statement

The optimization of large CFD models could be prohibited due to high processing time, which increases with a high number of input variables (k > 10). To surpass this issue, RS training was performed (JENSEN; MAYORGA; PAPADIMITRIOU, 2015). The optimization approach was executed using the improved version of the Non-dominated Sorting Genetic Algorithm (NSGA-II) implemented in software modeFRONTIER (DEB *et al.*, 2002), which is a computationally fast and elitist evolutionary algorithm that can maintain a good spread and convergence of solutions. The procedure used the variable population algorithm with crossover probability and mutation probability set in 0.9 and 0.01, respectively.

An unconstrained optimization procedure was considered since no prohibitive fluid flow phenomena were verified within the sample space, which is due to the 1D preliminary design predictions. Thus, the optimization statement was:

$$
\text{Find } X = \begin{Bmatrix}
A1 \\
L1A2 \\
L1A3 \\
L2A2 \\
L2A3 \\
L3A2 \\
L3A3 \\
A4 \\
P1x \\
P1z \\
P2x \\
P2z \\
P3x \\
P3z \\
P4x \\
P4z \\
SP1 \\
SP2 \\
S1 \\
S2 \\
S3 \\
H1 \\
H2 \\
H3 \\
POS
\end{Bmatrix} \text{ which maximizes the polytropic efficiency, } \eta_p(X)
$$

An initial DoE size test was performed to assess the influence on optimization final results, in which three sets of the initial population were generated through Uniform Latin Hypercube Sampling (ULHS) (MCKAY; BECKMAN; CONOVER, 1979): 60, 120 and 240 cases. Despite the differences in convergence speed, the maximum polytropic efficiency was the same for all.

3   RESULTS

The main results obtained by the presented methodology were discussed in three sections as described:

- One-dimensional optimization of the whole compression train subjected to the constraint herein elaborated 'Gas-like Behavior Margin' (GBM), which minimized the total drive power and ensured the feasibility of each centrifugal compressor.
- Implications of the adopted SA methodology for large CFD models applied to the first stage compressor, providing low-cost sample space screening and CFD modeling 'know-how' for centrifugal compressors.
- Results of low-cost RS training strategy for a high number of interacting variables on large CFD models and s-CO_2 phenomenology analysis approach for low-flow-coefficient centrifugal compressors.

3.1 Optimized One-Dimensional Compression Train and Fourth Stage S-Co2 Centrifugal Compressor Evaluation

The factor fixing performed using the 1D sensitivity analysis was based on the discussion of this chapter, which has decreased the optimization complexity and computational cost. Moreover, the optimized fourth stage of compression CFD model was built to assess the validity of 1D model predictions on the machine's performance. Particularly, the novel GBM constraint was investigated herein to evaluate its capacity to be a robust criterion to avoid transcritical regions in the compressor thermodynamic region.

The remaining variables choice of the optimization flowchart presented in Section 2.4.1 was due to the SA of this chapter. Figure 27 shows the main effects of Morris' method using only 290 simulations, while Figure 28 shows the results for the SS-ANOVA method considering main and interaction effects which required 25000 simulations (only possible due to the low computational cost of the 1D model – a few seconds each case) .

Figure 27 – Morris' screening method ranking of variables.
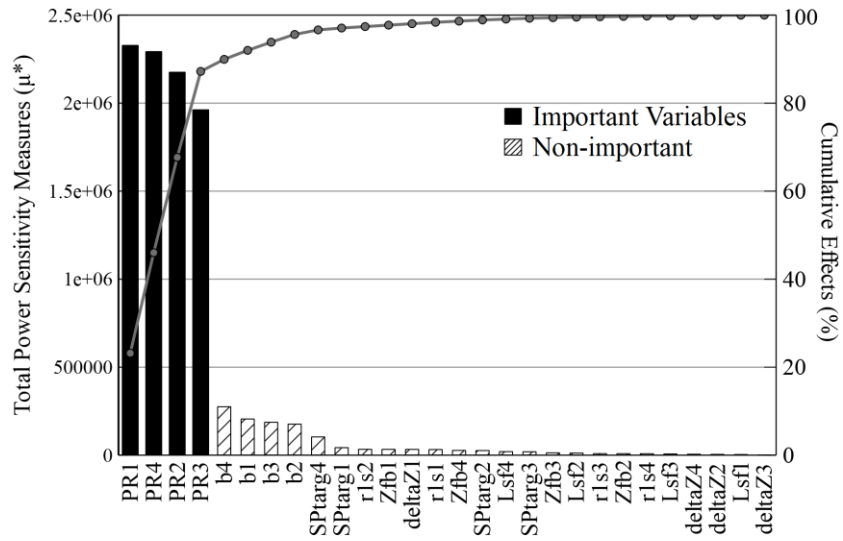
Figure 28 – SS-ANOVA method ranking of variables
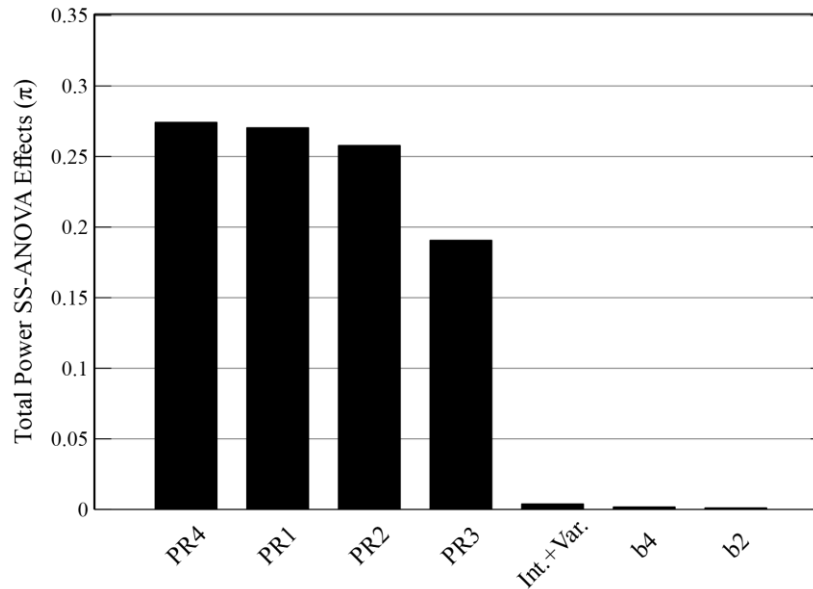
The comparison between Figure 27 and Figure 28 shows that both methods found the same important variables, meaning that Morris' method is reliable for factor fixing purposes for models that interaction effects are negligible, considering also that Morris' method required only 1.2% of the computational effort required by SS-ANOVA. Overall, the pressure ratios for all four stages are maintained as important variables for the next optimization procedure.

Furthermore, Morris' SA was also performed for the constraints defined for the optimization procedure, presented in Figure 29. In addition to the pressure ratios, already identified as important variables, the inlet shroud radius for all stages ($r_{1s,i}$) is included in the group of important design variables. Despite the low sensitivity measure values on the last two compressors, which is due to their narrower ranges, we have chosen to maintain these variables due to their potential to improve throat Mach number during the optimization procedure without changing the geometry of the centrifugal compressor significantly. Moreover, SS-ANOVA was also performed for the constraints and does not find interactions between variables, similar to the total power analysis.

Figure 29 – Morris' sensitivity measures of optimization constraints
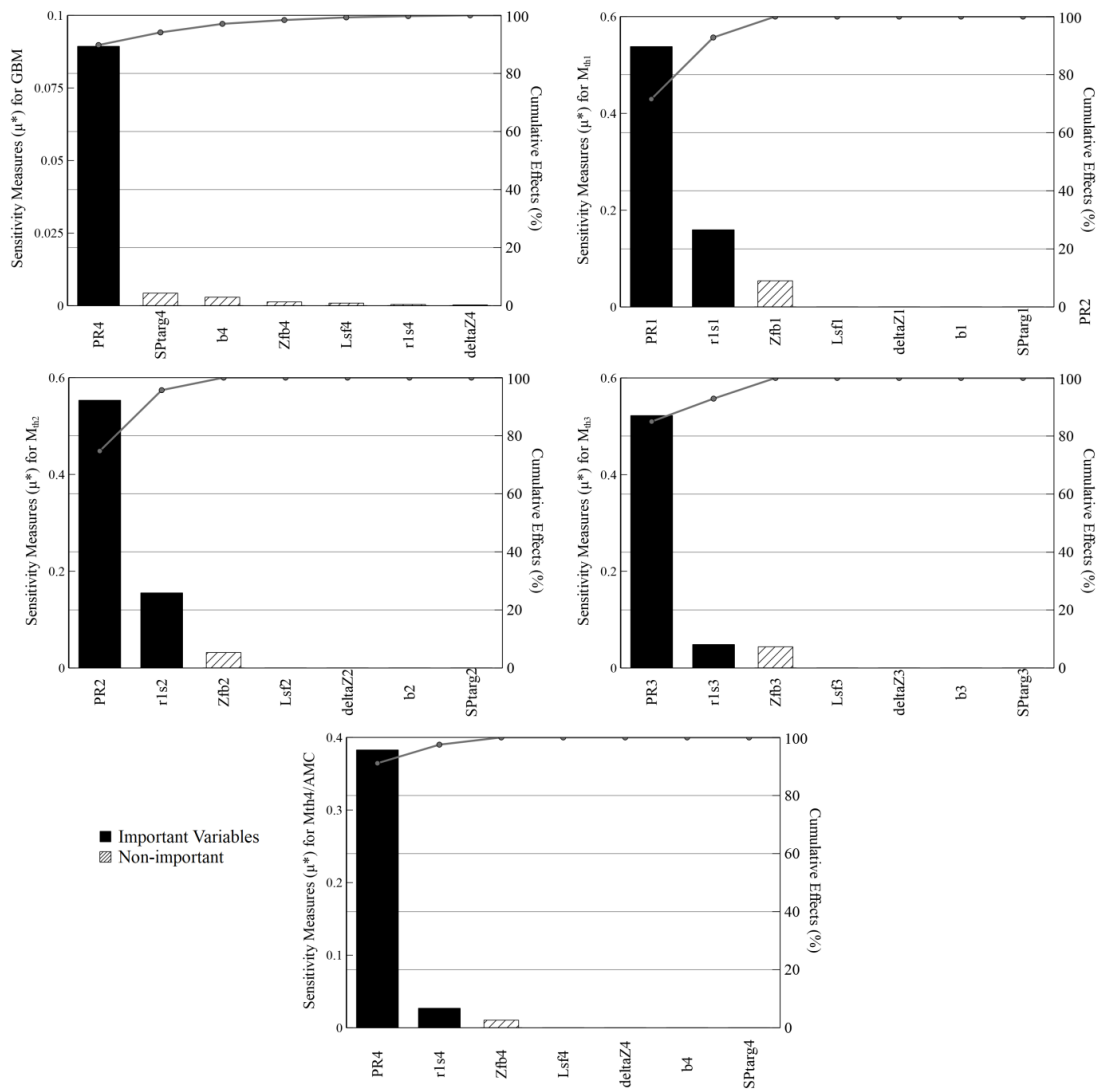
Source: Author.

The number of blades for each stage ($Z_{fb,i}$) demonstrated a small influence on constraints involving Mach number. Their sensitivity measures were similar to the inlet shroud radius in the third and fourth stages. Therefore, because of their low sensitivity measure values at the two first stages, we decide to fix them. Moreover, the remaining variables were not expected to have effects on the Mach number, as confirmed by the analysis. Splitter length ($L_{sf,i}$) and Axial Height ($\Delta Z_{,i}$) are geometric variables of the impeller but are not related to the throat sizing. The diffuser height ($b_{4,I}$) and volute sizing parameter ($SP_{targ,i}$) are too downstream and did not show any influence on the Mach number of the machine. As GBM is greatly influenced only by the fourth pressure ratio, the important variables group was set with the 8 already described variables (Pressure Ratios, PR_i, and Inlet Shroud Radius, $r_{1s,i}$).

3.1.1 *Optimized Compression Train*

The insertion of the constraints on the optimization procedure through 1D model was able to avoid several issues related to $s - CO_2$ centrifugal compressor train system such as shockwaves, condensation and also due to the crossing of the Widom-line during the last compression stage. Moreover, the initial population for genetic algorithms is usually from 2 to 4 times the number of variables and constraints in the model. However, to make sure the initial population is not influencing the optimization performance, an initial population study was performed using 78, 187 and 384 cases defined by the Uniform Latin Hypercube Sampling (ULHS)(MCKAY; BECKMAN; CONOVER, 1979), as presented in Table 18.

Table 18 – Initial population used for NSGA-II

Initial Population	Number of Generations	Minimum Power Achieved
78 cases	40	15.093 MW
187 cases	35	15.063 MW
384 cases	85	15.068 MW

Source: Author.

It is clear that the increase on initial population has low influence on the minimum power of the system, and if it is too large the number of generations for convergence can increase

significantly. Therefore, 187 cases were considered enough for the purpose of this work. For all optimization procedures, the crossover probability parameter is set by 0.9 and the mutation probability is 0.01, as it is common practice for genetic algorithms.

A baseline centrifugal compressor train system was arbitrarily defined based on fluid flow constraints and the desired outlet pressure, according to Table 19.

Table 19 – Baseline, optimized and constant compression systems power consumption

Variable	Baseline	Optimized	Constant
PR1	2.65	2.95	2.72
PR2	2.65	2.90	2.72
PR3	2.65	2.30	2.72
PR4	3.65	3.40	3.40
r1s,1	190 mm	188.9 mm	190 mm
r1s,2	118 mm	115.2 mm	118 mm
r1s,3	70 mm	71.2 mm	70 mm
r1s,4	48 mm	46.6 mm	48 mm
$\sum_{1}^{4} \dot{W}_i$	17.53 MW	15.06 MW **(-14.09%)**	15.14 MW **(-13.63%)**

Source: Author.

Moreover, an extra compression system is added for the comparison ('constant column') which means that the last compressor is fixed with the same pressure ratio as the optimized case and would shift the first three stages to a constant pressure ratio. This approach intends to demonstrate the impact of different pressure ratios, as suggested by the optimization procedure at the early compression stages on total power consumption.

Figure 30 shows the T-s diagram for the baseline and optimized configurations. The optimization procedure finds the optimized configuration of the compression system close to Widom-line (left side on the T-s diagram), consuming less power to increase the pressure to the desired level at the outlet of the 4ª stage compression.

Figure 30 – T-s diagram of baseline and optimized compression train system
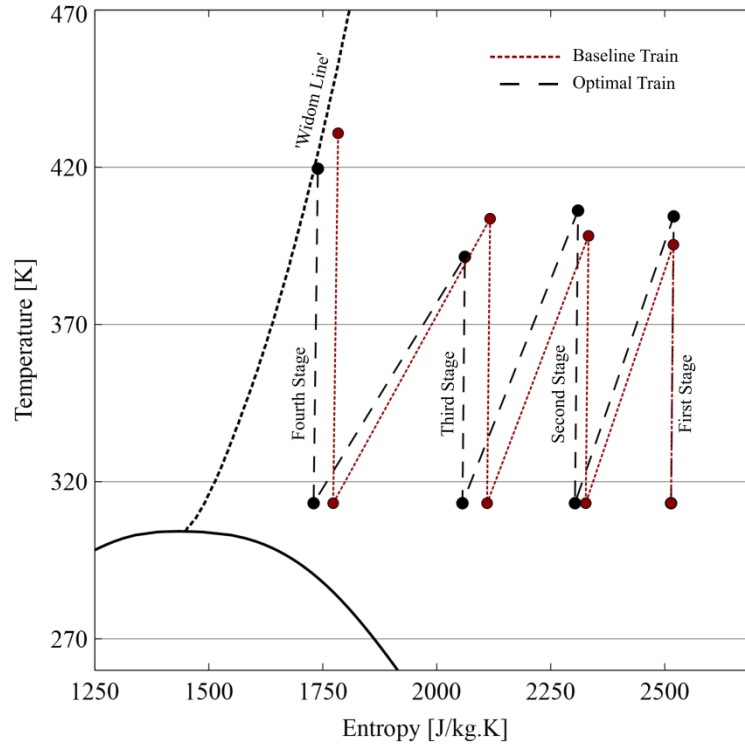
Source: Author.

The GBM constraint (GBM > 1) blocks the optimization procedure to crossing the Widom-line toward a liquid-like region which is undesired due to high sCO_2 thermodynamic properties variations. Table 19 shows that the optimized configuration of the compression train system reduced the required power by 14.09%.

The pressure ratio for the last stage is reduced as much as possible (PR = 3.40) since the Widom-line limits further decrease on the fourth stage pressure ratio to ensure feasible equipment. The same behavior is demonstrated in the third stage, which is reduced to the minimal pressure ratio that would still provide a feasible compressor to deliver the desired outlet pressure at the system exit (> 25MPa). On the other hand, the two early stages' pressure ratios are increased, which is necessary to ensure that the total pressure at the system exit is achieved. Moreover, the comparison with constant early stages configuration shows an advantage in diminishing the third stage pressure ratio to lower levels, as found by the optimizer, spending about 0.5% less energy to attend the same compression level.

The total power consumption for the optimized model is 14.09% lower than that of the baseline model. Of course, the baseline configuration was an arbitrary choice at the right side of

the Widom-line. However, the reduction of the fourth stage pressure ratio is responsible for most of the power consumption reduction at the compression train, since constant pressure ratios is only 0.5% higher than the optimized train.

3.1.2 Analysis of the dynamic flow

Finally, a CFD analysis was performed at the fourth stage of compression to verify the effectiveness of the one-dimensional design. First, no condensation was found since the comparison of the Mach number at the machine's throat with the AMC limit (Figure 31) provided mean values much lower than the AMC level. Evidently, condensation would not occur downstream in the impeller since the saturation dome is further away as the compression occurs.

Figure 31 – Absolute Mach number from CFD simulation for the 4st stage.
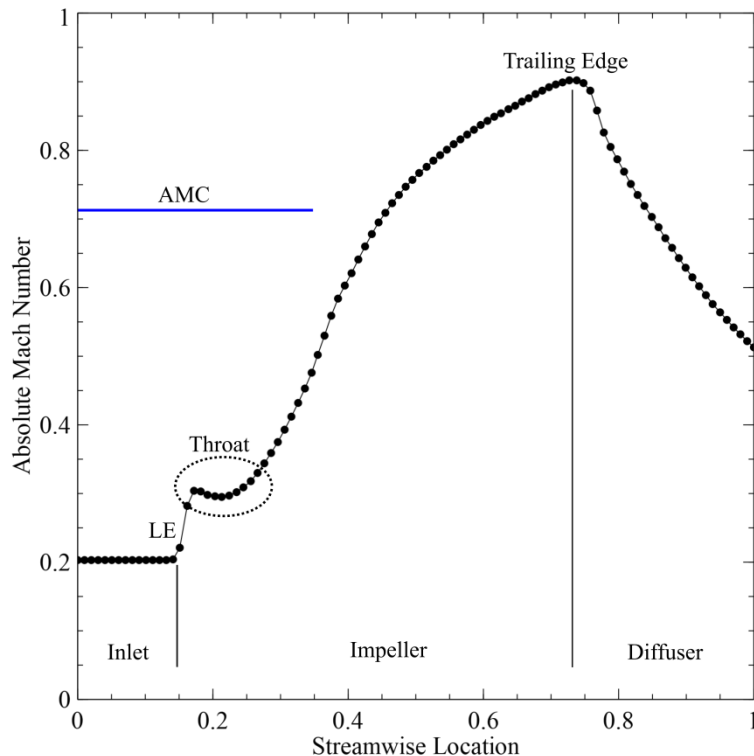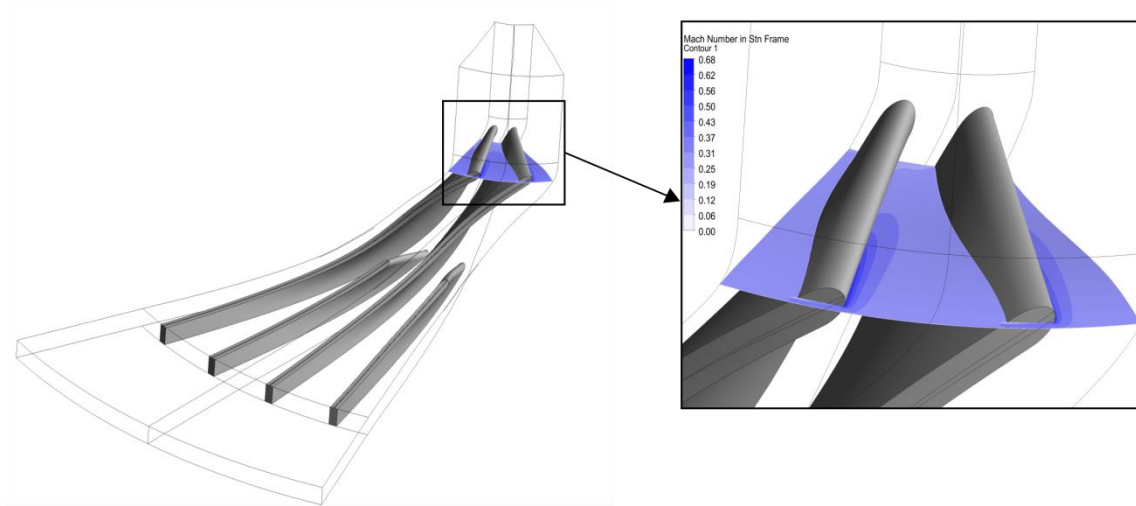

Source: Author.

The CFD phenomenology analysis of the compressor throat (Figure 32) also illustrates how the 1D code avoids condensation. The maximum Mach number at the throat estimated through

the 1D code is 0.69, which is corroborated by the CFD results that estimated a maximum value of 0.68 at the shroud. Since AMC value for this machine's inlet condition is 0.71, condensation is not expected to occur.

Figure 32 – Mach number distribution at the machine's throat.

Source: Author.

The preliminary geometry simulated from CFD approach is considered to verify the compressor configuration by 1D code. Therefore, the main interest outputs are compared in Table 20, i.e., isentropic efficiency, pressure ratio at impeller exit and total power consumption. These global output variables were evaluated since they are a consequence of the whole compressor simulation, being better to represent models' accuracy.

Table 20 – 1D model outputs verification.

| Variables	1D	CFD	Diff. (%)
Isentropic Efficiency (%)	82.13*	83.6**	1.75
Power Consumed	3.46 MW	3.64 MW	4.94
Impeller Pressure Ratio	3.86	3.90	1.02

Note: * At exit of the Volute.
** At the exit of the Impeller.
Source: Author.

The low differences between 1D and 3D approaches indicate that the methodology presented for the present work is able to design robust centrifugal compressors operating at the supercritical

state of the CO_2 while maintaining the gas-like behavior. Moreover, CFD models are able to better predict total power consumption than the 1D loss models since turbulence, recirculation and swirl are better addressed due to their tridimensional phenomena. The total power consumption found by CFD model is 4.94% higher than 1D model. Nevertheless, the 1D methodology remains an excellent tool to provide a start point for centrifugal compressors' design. Moreover, gas-like behavior is verified through the speed of sound values at the outlet of the CFD analysis, which is lower than the limit value at the Widom-line showing that the CO_2 state remains at the gas-like side. The maximum values for meridional velocity are presented at the axial to radial direction change region in the impeller, being reduced afterward at the end of the impeller channel and diffuser (Figure 33). A backflow recirculation is observed at the impeller/diffuser interface, which perhaps can be mitigated by a CFD model optimization procedure.

Figure 33 – Meridional velocity by CFD modeling for the 4st stage
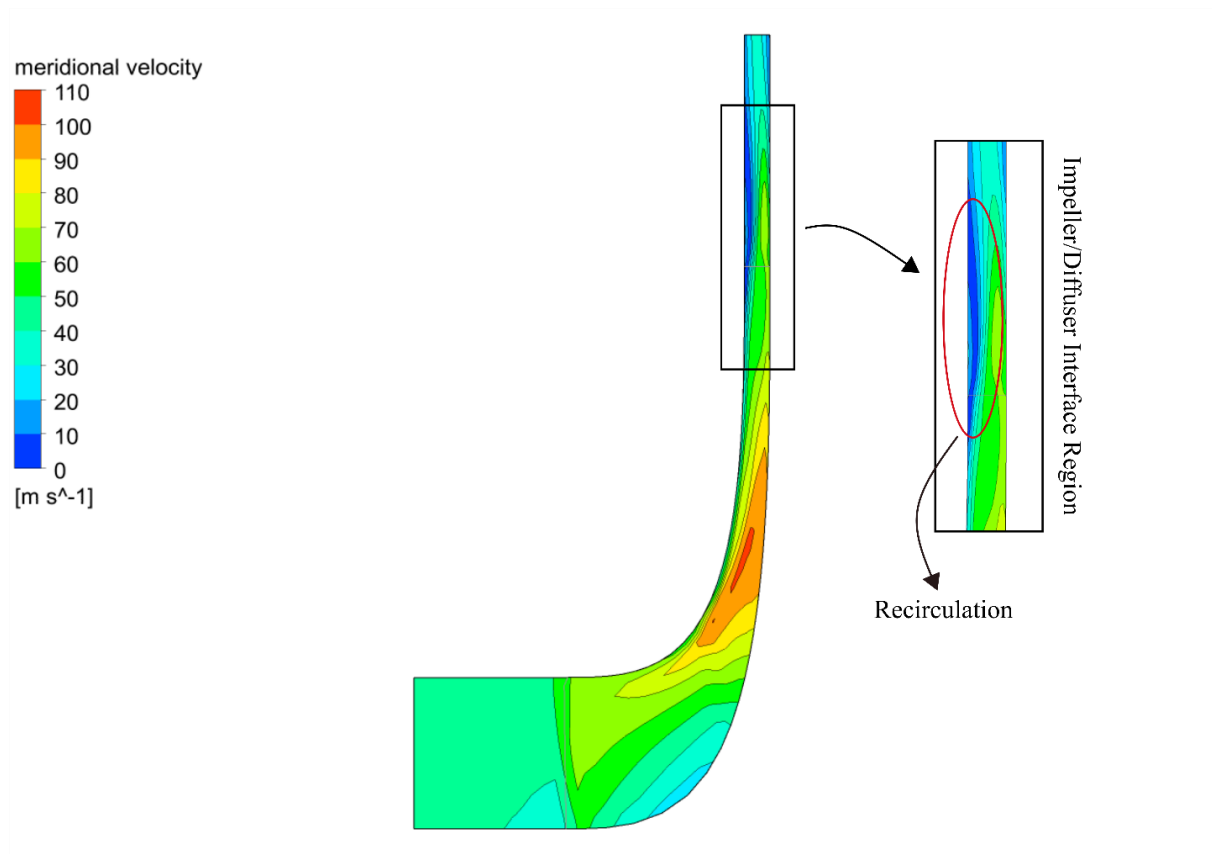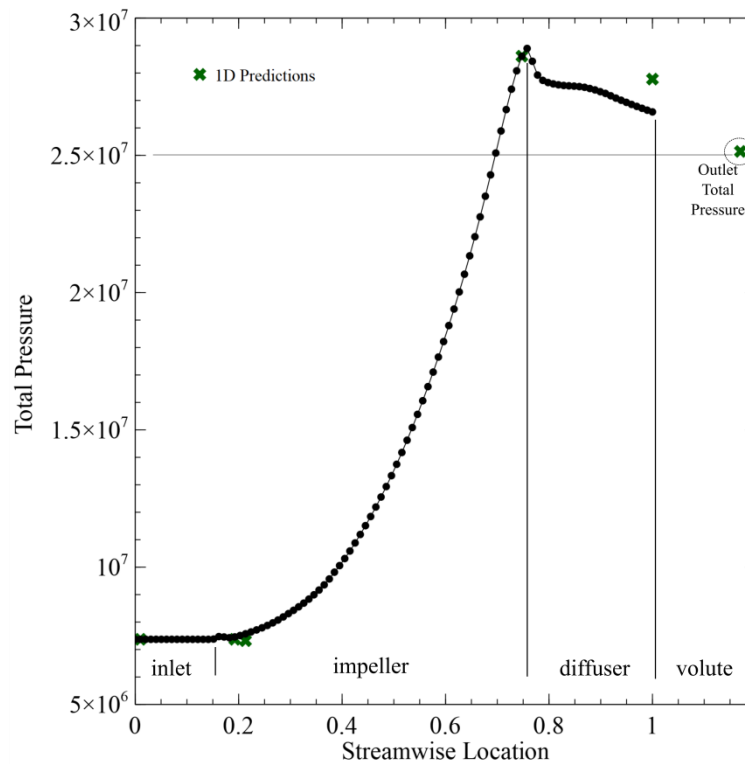

Source: Author.

The total pressure chart for the 1D model predictions and CFD model results is shown in Figure 34, indicating a good agreement between 1D and 3D approaches. In fact, the total pressure

difference between approaches is 1.03% at the impeller outlet and 3.97% at the diffuser outlet. Although the 3D modeling of the volute is not the main goal of the present work, this study can corroborate one-dimensional prediction for total pressure, ensuring that the total pressure goal is achieved by the equipment. Moreover, the CFD allows better understanding related to energy losses in the vaneless-diffuser due to friction, which becomes evident when compared to the losses predicted by the 1D, indicating a need for improvements in vaneless diffusers loss assessment.

Figure 34 – Total pressure comparison between 3D CFD and 1D model approaches.

Source: Author.

Summing up, a thorough optimization methodology for the supercritical centrifugal compressor train was developed considering fluid flow phenomena and thermodynamic conditions. A direct thermodynamic analysis is not enough for a complete design of supercritical centrifugal compressors train since they do not take into account fluid flow phenomena such as the high change in the fluid properties close to Widom-line. Therefore, the Gas-like Behavior Margin (GBM) developed is able to circumvent the uncertainties of operating on the transcritical region, ensuring suitable CFD convergence and physical analysis. Moreover, the calibration

procedure developed to adjust the preliminary geometry provided by the 1D method to the CFD outputs proved to be an effective strategy after numerical verification.

Furthermore, Morris' sensitivity analysis method has found the same important variables as the SS-ANOVA method, using only 1.2% of the clock time. Additionally, the optimizer reduced the total power consumed by 14.09%, with good agreement between CFD and 1D numerical approaches, ensuring that the 1D code is robust for preliminary geometries. Overall, the training of a function that represents de CFD model for the calibration procedure could complete the 1D methodology presented herein, turning it into a more suitable centrifugal compressor tool and a CFD sensitivity analysis and optimization of the fourth stage geometry would complete the thermal design of the equipment.

3.2 Sequential Sensitivity Analysis and Optimization Applied to the First Compression Stage Centrifugal Compressor

The first step of the proposed sequential SA was Morris' screening method, which aimed to fix non-important variables and find interaction effects, followed by a convergence analysis of its sensitivity measures to ensure robustness. The second step was the SS-ANOVA quantitative method, which was applied to verify the reliability of the Morris method. Afterward, a single-objective optimization using the input variables identified as important was performed. Polytropic efficiency was maximized under constraints defined by minimal pressure ratio, maximal temperature ratio, and required power. To ensure the quality of the factor-fixing methodology for the optimization procedure, the same single-objective optimization was conducted using the eight input variables of Table 16.

3.2.1 Morris' elementary effects

To assess the overall performance of a centrifugal compressor, four important design variables were considered: polytropic efficiency, pressure ratio, required power, and temperature ratio. A suitable compressor design should aim for the highest possible efficiency and pressure ratio with the lowest required power and temperature ratio. The histograms of Figure 35 show the

main effects of Morris' method for each interest output. Furthermore, a cumulative effect curve with points between the histogram bars is defined as 80% for the cut-off methodology.

Ranking histograms were achieved by running only 90 CFD cases (average of 4 hours for each case). Overall, the trailing-edge polar angles (L1A4, L2A4 and L2A3) were the most important in compressor performance, leaving the angles at the leading-edge position (L1A1, L1A2 and L2A1) with a lower influence. The physical mechanisms responsible for that are discussed in the next section. Table 21 summarizes the non-influential variables for each interest output, considering as important variables those responsible for more than 80% of the output cumulative effects.

Figure 35 - Main effects sensitivity measures of Morris screening method; (a) polytropic efficiency, (b) pressure ratio, (c) required power and (d) temperature ratio.
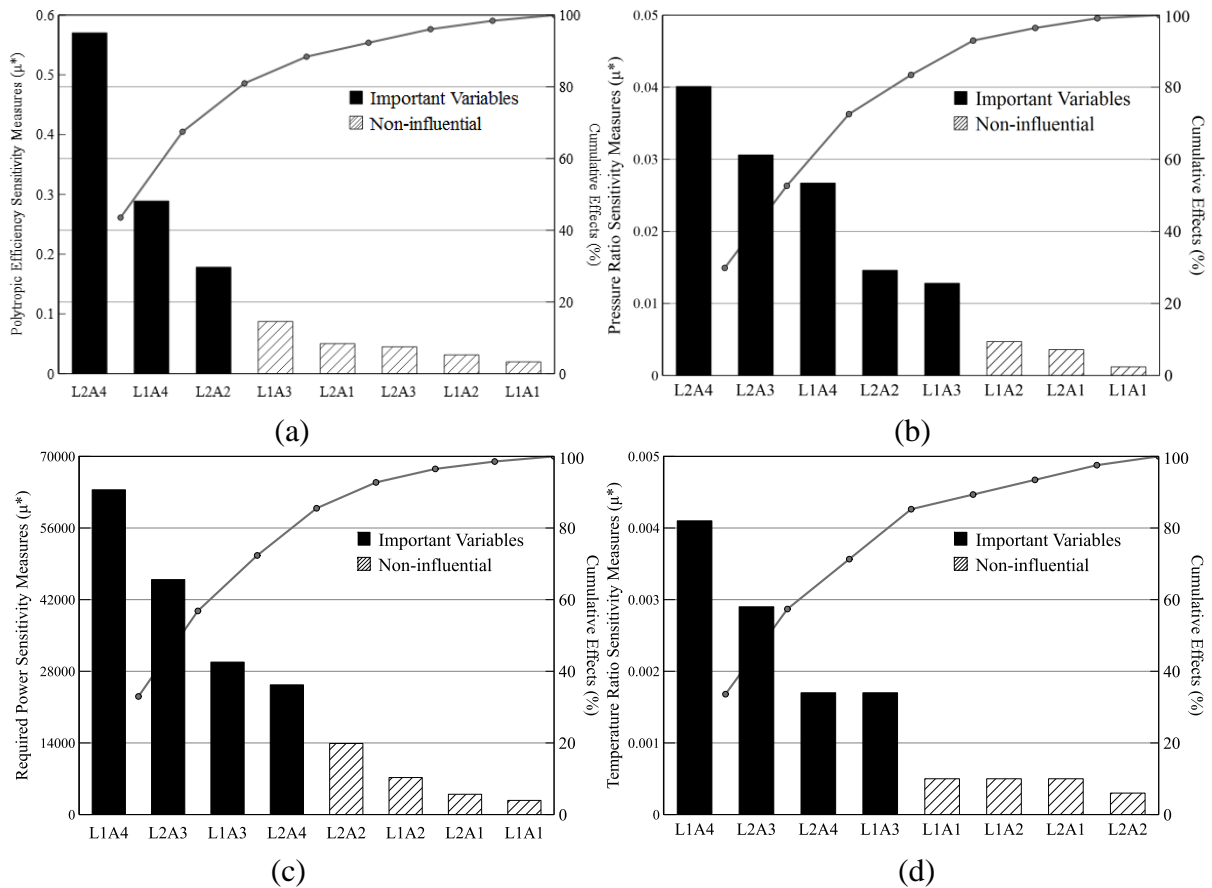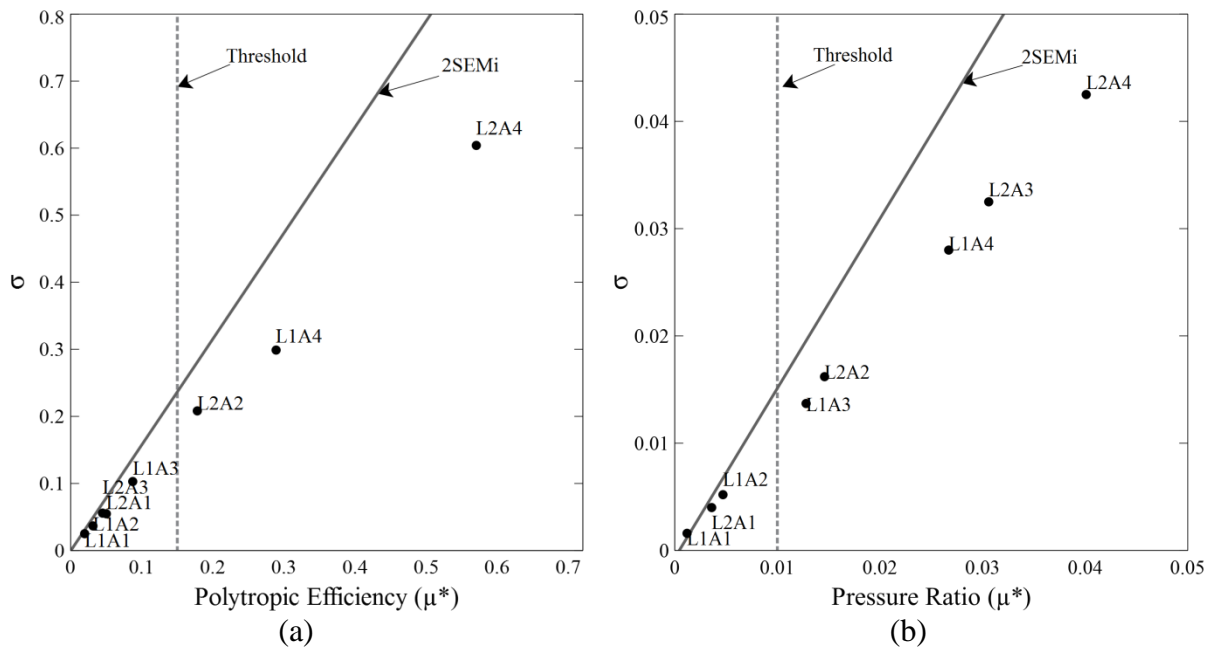

Source: Author.

Table 21 - Non-influential variables according to Morris' screening analysis.

Output	Non-influential variables					
Polytropic efficiency	L1A1	L1A2	L1A3	L2A1	-	L2A3
Pressure ratio	L1A1	L1A2	-	L2A1	-	-
Required power	L1A1	L1A2	-	L2A1	L2A2	-
Temperature ratio	L1A1	L1A2	-	L2A1	L2A2	-

Source: Author.

Variables L_1A_1, L_1A_2, and L_2A_1 are non-influential for all outputs evaluated by Morris' sensitivity analysis. Therefore, they can be fixed at their original value (Table 16) and excluded from the optimization procedure, with a slight impact on the overall results. Figure 36 shows that important angles are below the reference line 2SEMi, which means that their main effects are much greater than their interaction effects. In other words, interaction effects can be considered negligible.

Figure 36 - Interaction effects analysis of Morris' screening method; (a) polytropic efficiency, (b) pressure ratio, (c) required power, and (d) temperature ratio.
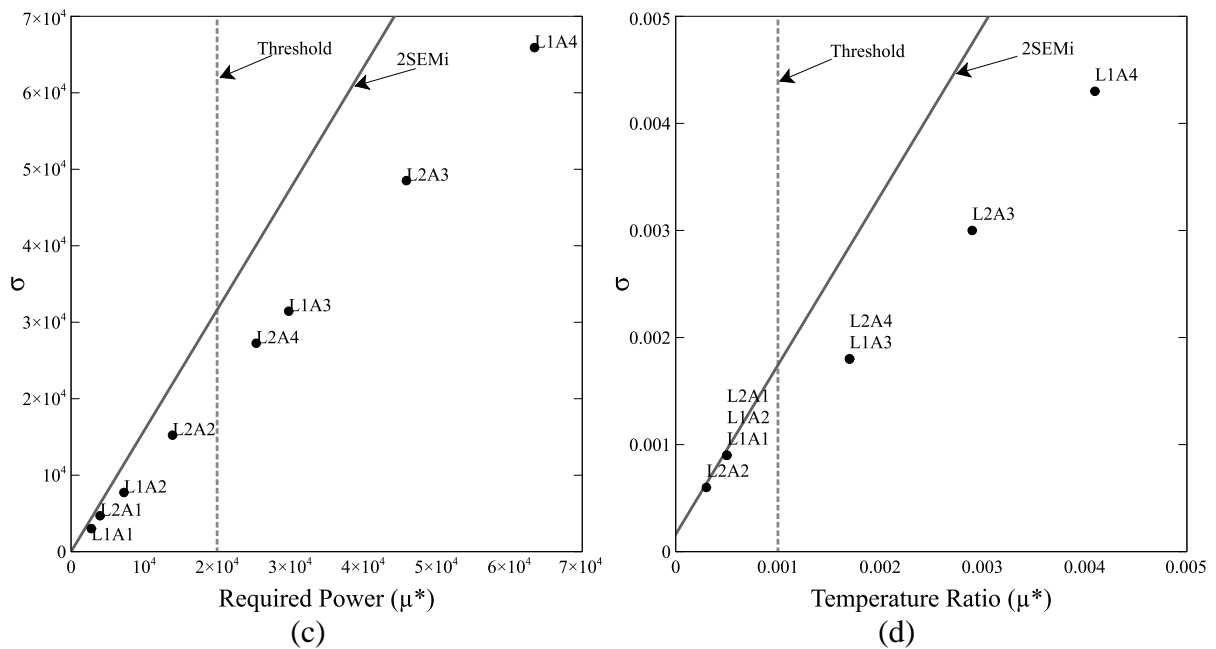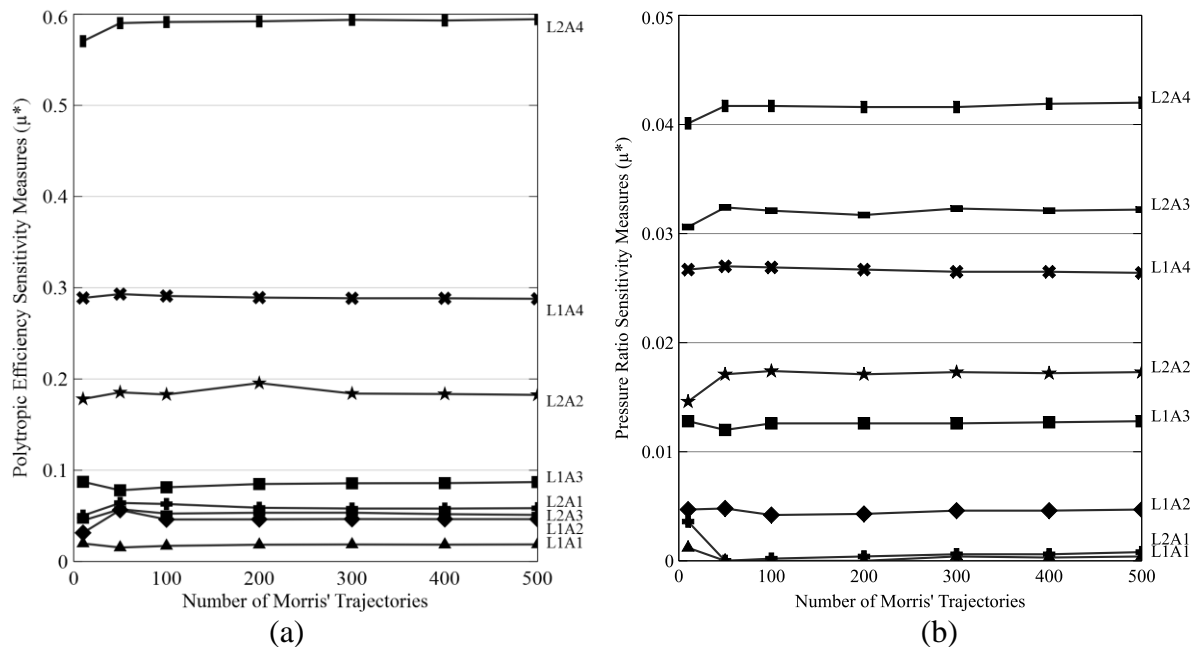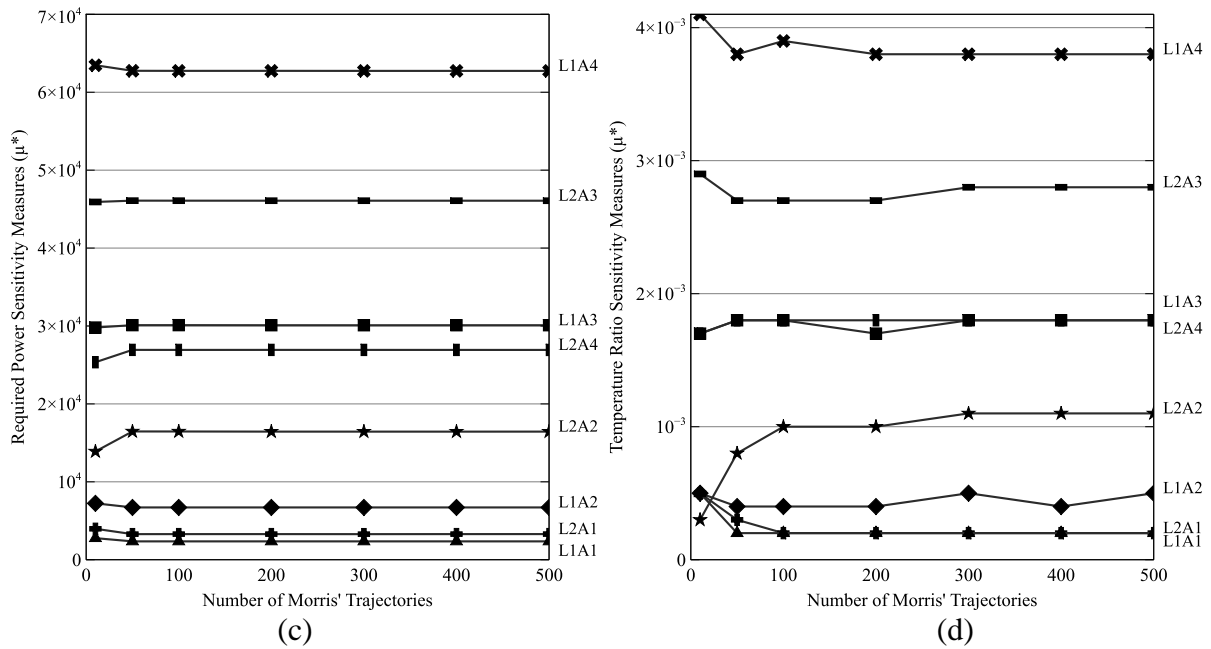
Source: Author.

Figure 37 shows the impact of the number of DoE trajectories on output variables, starting with the original DoE containing ten trajectories assessed by the CFD model (suggested in Saltelli *et al.* (2008)) up to 500 trajectories evaluated by the RS models.

Figure 37 - Morris' sensitivity measures convergence analysis, (a) polytropic efficiency, (b) pressure ratio, (c) required power and (d) temperature ratio

Source: Author.

As discussed, the number of trajectories is critical to ensure the Morris method's robustness (GE; CIUFFO; MENENDEZ, 2014)(GE; CIUFFO; MENENDEZ, 2014). Too many trajectories would needlessly increase computational efforts and insufficient trajectories would provide misleading sensitivity measures.

This extrapolation study corroborates the results found with ten trajectories of Figures 35 and 36, although the ranking slightly changed for temperature ratio. In other words, if we applied the same methodology for factor fixing using the 500 trajectories ranking, we would classify the same input variables as non-influential (L_1A_1, L_1A_2, and L_2A_1). Therefore, the use of only ten trajectories has proved appropriate for the factor fixing of non-influential input variables. Moreover, as suitable response surfaces were used to perform this convergence study, the results presented herein are subjected to minor discrepancies from the original CFD model and are only valid inside the input range presented in Table 16.

3.2.2 SS-ANOVA quantitative measures

The trained RS turned feasible the SS-ANOVA method (GU, 2002). This quantitative method can provide a variance-representative ranking of input variables as well as corroborate Morris' method for factor-fixing purposes. Using ModeFRONTIER software, ULHS (MCKAY;

BECKMAN; CONOVER, 1979) was built containing the total amount of 512 cases (k^3) evaluated by RS functions. This number of CFD simulations would be computationally expensive, making the analysis a prohibitive task, especially for analysis with several input variables. A second-order evaluation of SS-ANOVA sensitivity analysis was performed to assess the main and interaction effects between input variables.

Two quality design variables were used to ensure the method's robustness: R^2 and orthogonal quality (OQ), both were expected to be near unity (GU, 2002). The quality design variables of the four interest outputs had excellent regression results ($R^2 > 0.99$) and the maximum OQ was 1.11 for the required power output, which is acceptable. Figure 38 shows the rankings of the main effects through SS-ANOVA method and their summed interaction effects (INT).

Figure 38 - SS-ANOVA sensitivity analysis ranking, (a) polytropic efficiency, (b) pressure ratio, (c) required power, and (d) temperature ratio
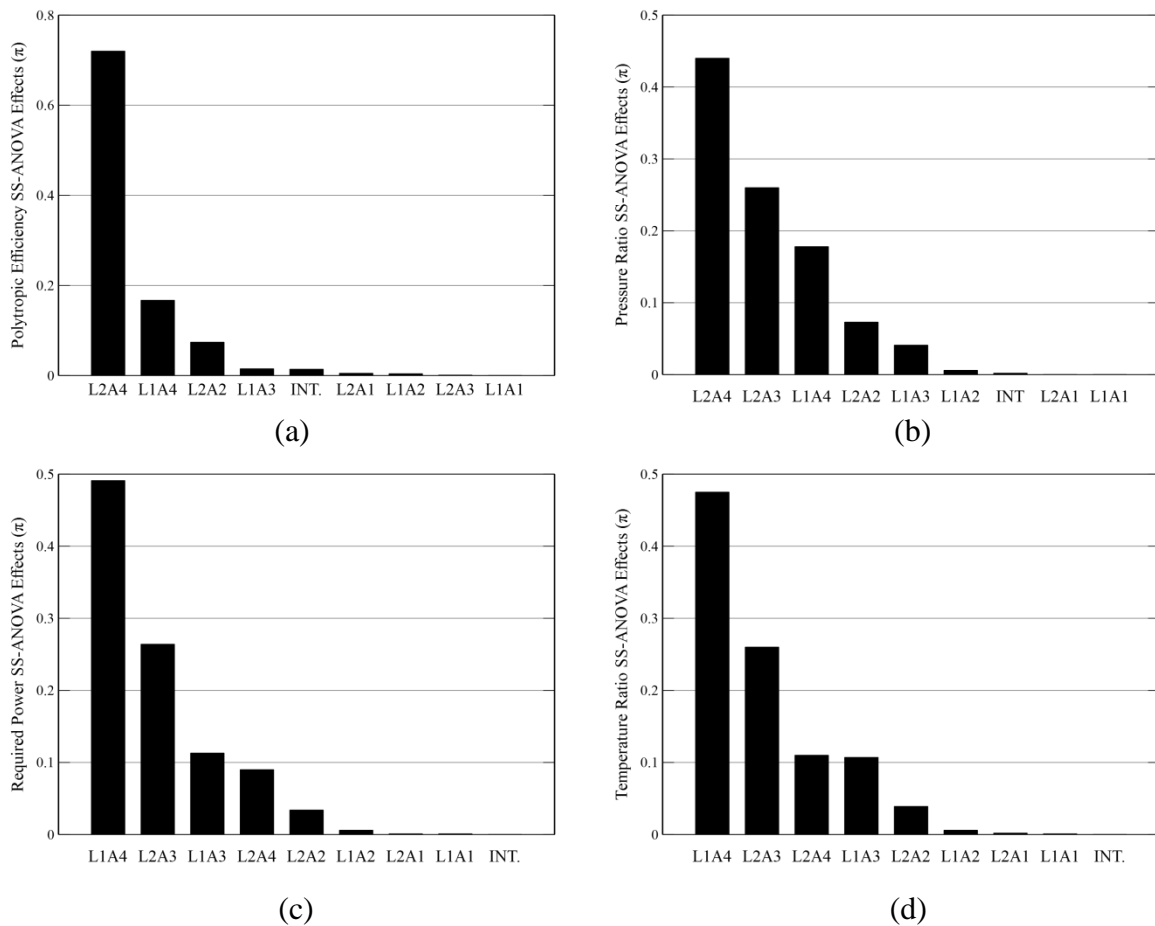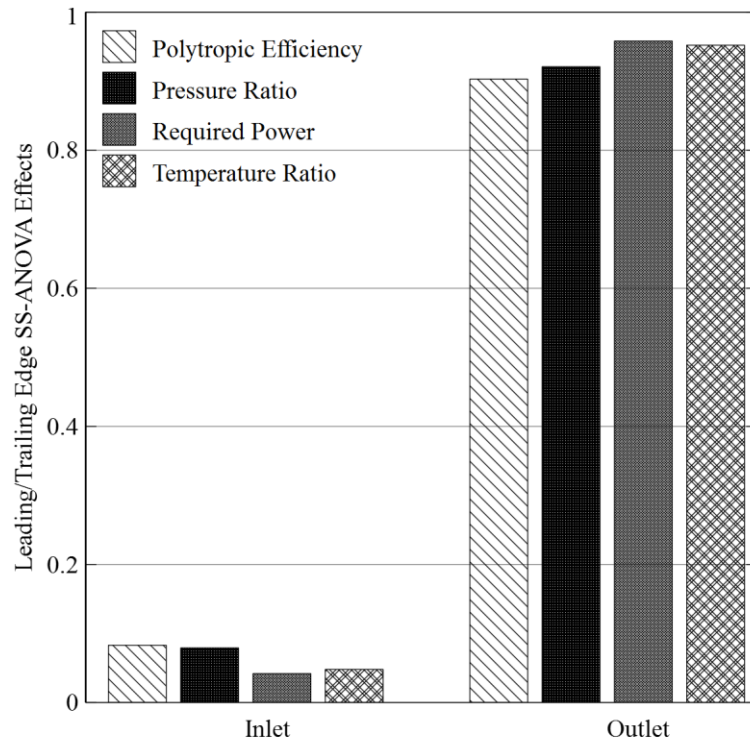

Source: Author.

The Morris' convergence study and SS-ANOVA analysis (Figures 37 and 38) provided the same variable ranking, corroborating the factor fixing reliability proposed by Morris' method (Figures 35 and 36), since each method uses different DoE to assess their effects on the outputs. These two SA methodologies can only be compared due to the good fitness achieved by the response surfaces shown in Table 15 since the deviations from CFD model can be expected due to RS inherent errors. However, such a small difference does not nullify the present results.

One could argue that more reliable factor fixing could be achieved by using the final converged Morris sensitivity measures. However, for factor fixing, it is already shown that non-influential variables would be the same. Moreover, Morris' method is more conservative than SS-ANOVA, i.e., using the same threshold of 80% of outputs variability cumulative effects, it would find fewer non-influential variables (SS-ANOVA added L2A2 as non-influential). Even though the methods have different types of normalized measures, they are both used for factor-fixing purposes in practice and the threshold of 80% of its cumulative effects would be used for that. Therefore, the objective here is not to compare the measures of each method but to identify the factors that should be fixed if we used different methods to analyze the same variables. Additionally, slight changes in the ranking between methods were verified only for variables considered unimportant. According to both SA methods, the interaction effects of input variables were negligible and the main effects were responsible for almost the entire outputs variability, meaning that the impeller polar angles of centrifugal compressors have an additive impact on machine performance. Figure 39 shows the effect of the polar angles on the outputs considering the summed effects of variables close to the leading edge and trailing edge.

Leading-edge polar angles are those identified as A1 and A2 whilst trailing-edge are identified as A3 and A4, for both layers (hub and shroud). According to SS-ANOVA analysis, more than 90% of all output variability was due to changes in trailing-edge polar angles, meaning that the polar angles of the leading-edge had a small influence on shockwaves present in Figure 40.

Figure 39 - Leading/trailing edge polar angles summed effects.
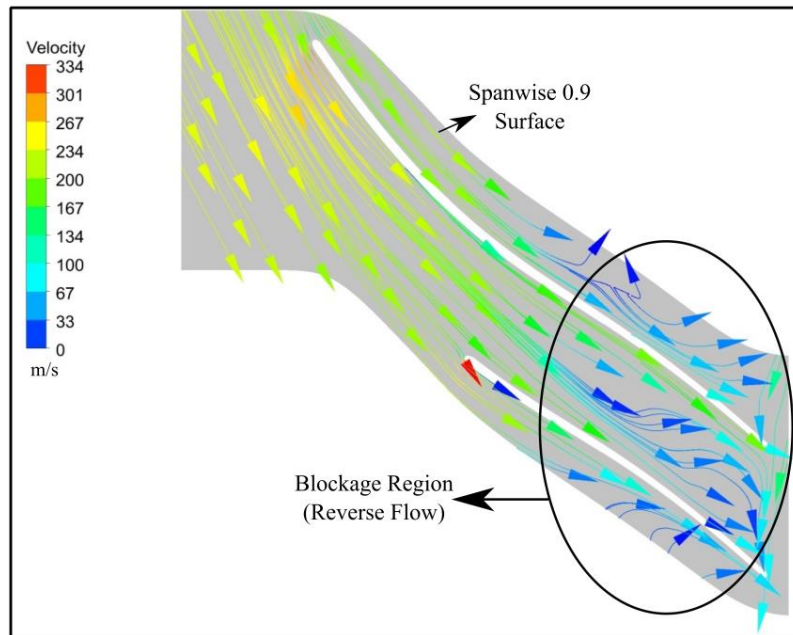

Source: Author.

Figure 40 - Spanwise view of relative Mach number on the original impeller
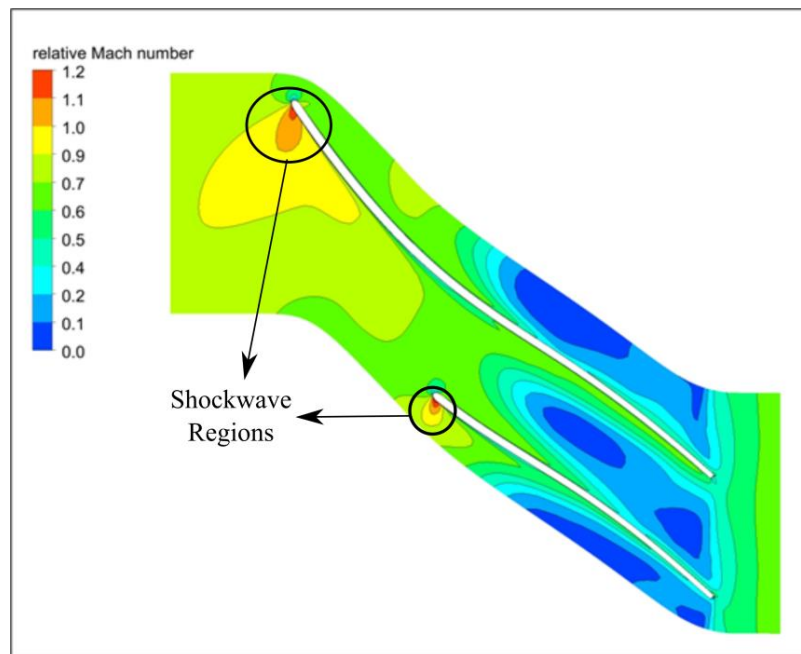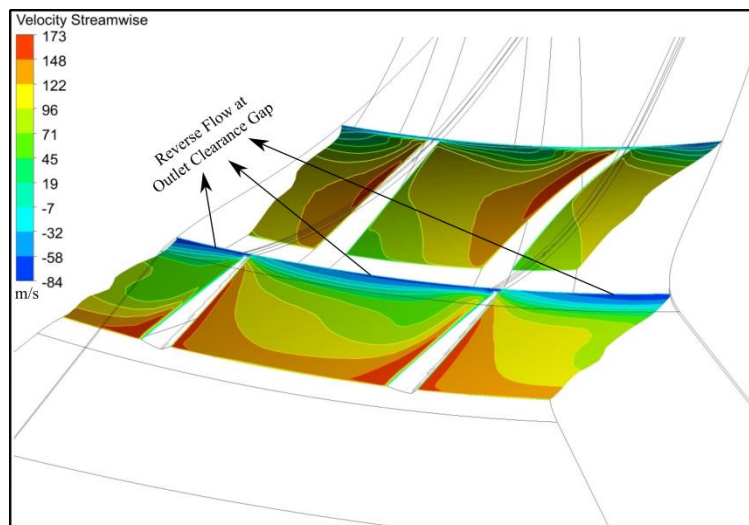

Source: Author.

Moreover, the polar angles were found very important in flow blockage caused by the reverse flow near the clearance gap at the trailing-edge (Figures 41 and 42).

Figure 41 - Streamwise view of streamlines on the original impeller
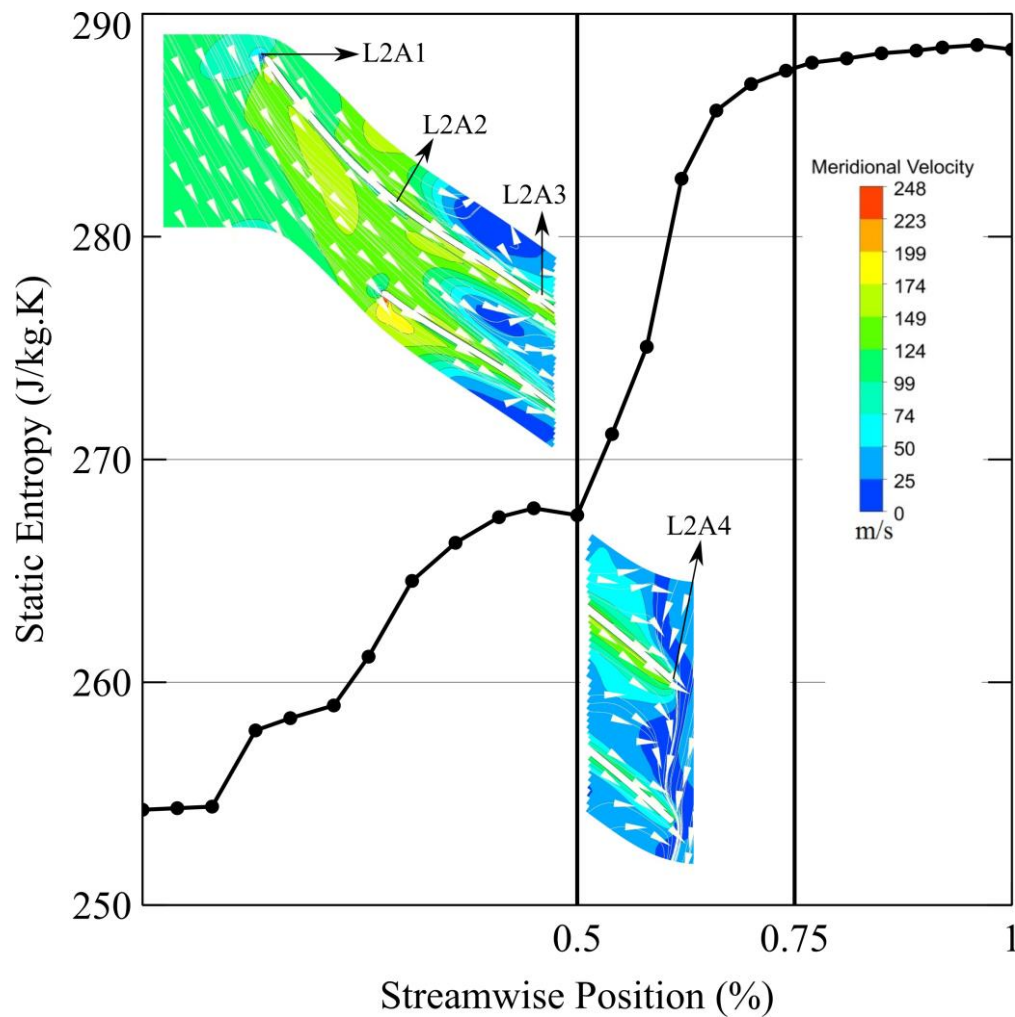

Source: Author.

Figure 42 - Spanwise view of velocity direction for the original impeller

Source: Author.

The SA indicated that polar angles at the impeller/diffuser interface region (trailing-edge) had a greater impact than those angles at the leading-edge. In fact, the reverse flow found at the clearance gap (Figure 42) was a significant source of loss, which can be verified by analysis of the entropy chart shown in Figure 43.

Figure 43 - Static entropy chart in spanwise view with velocity streamlines

Source: Author.

The impeller/diffuser interface region (streamwise position 0.5 to 0.75) represented 48% of entropy increase, due to flow blockage. This physical phenomenon assessment is in agreement with SA predictions, reinforcing that Morris' screening method is a robust and reliable methodology for turbomachinery CFD model analysis.

3.2.3   *Optimization results and phenomenology analysis*

An indirect and constrained single-objective optimization procedure is performed as the statement optimization shown in section 2.4.2, using the RS (section 2.4.2.1) and NSGA-II algorithms. In order to assess if the factor fixing found by Morris' method can be reliably used for diminishing variables on a direct optimization, two approaches were performed using the same constraints. The first approach considered only the important variables found by Morris' method for factor fixing (five input variables) and the second took all input variables into account to assess the impact of factor fixing on final optimization results. Original and optimized polar angles are summarized in Table 22. In addition, for classification as non-important by Morris' method regarding all output variables, these fixed inputs are not involved in any significant interactions with other variables, as shown in Figures 36 and 38, which demonstrates that the polar angles RS is additive towards the output variability.

Table 22 - Comparison between original and optimized input values

Input angles (º)	Original	Optimized (5 inputs)	Optimized (8 inputs)
L1A1	0	0 (fixed)	-1.25
L1A2	17.98	17.98 (fixed)	17.62
L1A3	33.37	32.71	32.71
L1A4	61.69	62.92	62.92
L2A1	0	0 (fixed)	-1.25
L2A2	25.74	25.23	25.23
L2A3	40.21	39.41	39.41
L2A4	55.71	56.83	56.83

Source: Author.

Both optimization approaches found similar optimized design variables, except for those input variables fixed by Morris' analysis. Table 23 shows the outputs for the original model and the two optimized cases. The four output design variables presented (polytropic efficiency,

pressure ratio, temperature ratio and power required) were about the same for both optimizations, indicating that the SA analysis methodology presented herein is robust for factor fixing.

Table 23 - Comparison between original and optimized case outputs

Case	Model	Polytropic efficiency (%)	Pressure ratio	Temperature ratio	Power Required (MW)
Original*	CFD	85.41	2.89	1.30	4.76
Optimized	RS	86.14	2.89	1.30	4.72
(8 inputs)	CFD	86.11	2.90	1.32	4.74
Optimized	RS	86.07	2.89	1.30	4.72
(5 inputs)	CFD	86.05	2.90	1.30	4.74

Note: * Geometry defined based on Casey and Robinson One-dimensional approach (ANSYS VISTA CCD).
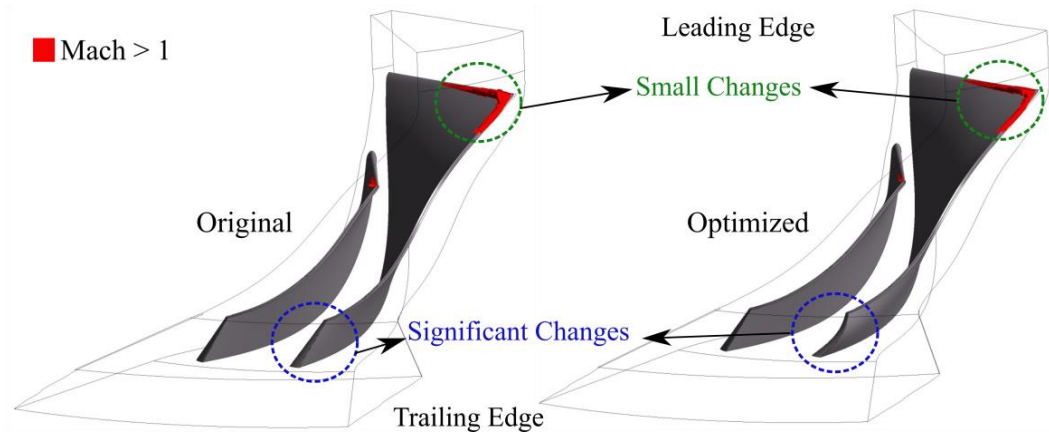Source: Author.

Results of the CFD model agreed with the optimized RS results since the absolute difference for polytropic efficiency was 0.03% considering eight input variables and 0.02% for five input variables. For all other output variables, the difference between CFD simulations and the results performed by RS were similar, showing that the RS trained, using the same DoE to evaluate Morris' sensitivity indices (quasi-optimal sampling), had an excellent fitting.

Moreover, polytropic efficiency increased by 0.7% and 0.64% considering eight and five input variables for optimization, respectively. These results reinforce the previous discussion that indicated the reliability of Morris' factor fixing of additive problems in the physical evaluation of centrifugal compressors. Moreover, Morris' method proved to be robust for fixing factors for a direct (and computationally expensive) optimization, causing minor losses in optimized design performance.

The literature review of parametric optimizations is in agreement with this order of magnitude for efficiency, which is considered relevant even though few input variables have been evaluated, indicating the potential of the present approach for high dimensional models. Furthermore, the original geometry presents an already high polytropic efficiency of 85.41%, considering that the streamline sizing method (CASEY; ROBINSON, 2008b) is a robust method to define initial geometry. As turbomachinery requires computationally expensive models, Morris' method with quasi-optimal sampling could be recommended as a relatively cheap and robust SA approach for

screening. Therefore, the following benefits could be highlighted: previous physical phenomena knowledge before running an optimization procedure, cheap and excellent fitted RS, and reliable factor fixing for diminishing the cost of high-dimensional problems, allowing the insertion of several variables that would not be part of the analysis otherwise. Furthermore, the RS optimization using NSGA-II evaluated about 2700 cases to achieve optimized point, which is assessed in less than 5 minutes after the response surface was trained (costing about 20 days to run the 90 CFD models used for training the RS). A direct optimization using the CFD model would take much more time (unfeasible if using NSGA-II). To assess the improvement at the leading-edge related to shockwaves, the percentage number of elements with a Mach number greater than 1 was computed and shown in Figure 44.

Figure 44 - Leading-edge elements with Mach number greater than one for original and optimized cases
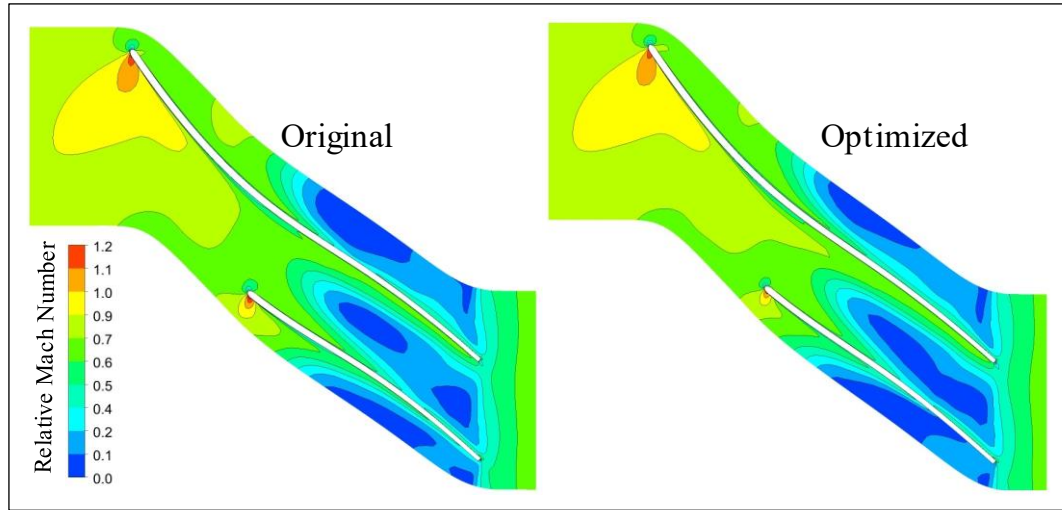

Source: Author.

The original and optimized geometries have around 7.47% and 7.09%, respectively, of elements highlighted. As already found by SA analysis and discussed in detail, the polar angles near the leading-edge have a small influence on the shockwaves, which can be verified on the slightly cambered shape at the leading-edge. On the other hand, significant changes are noted in the trailing-edge blade shape, which is responsible for the reduction in flow blockage.

The blockage caused by the reverse flow at the trailing edge is one of the main sources of loss in centrifugal compressor performance. Figures 45 and 46 show that the low-velocity region at

the trailing-edge is smoothed due to the new blade shape found by the optimized geometry, which reduces the flow blockage between the impeller and vaneless-diffuser.

Figure 45 - Spanwise view of Mach number contours on the original (ANSYS VISTA CCD) and optimized impellers

Source: Author.

Figure 46 - Spanwise view of streamlines on the original (ANSYS VISTA CCD) and optimized impellers
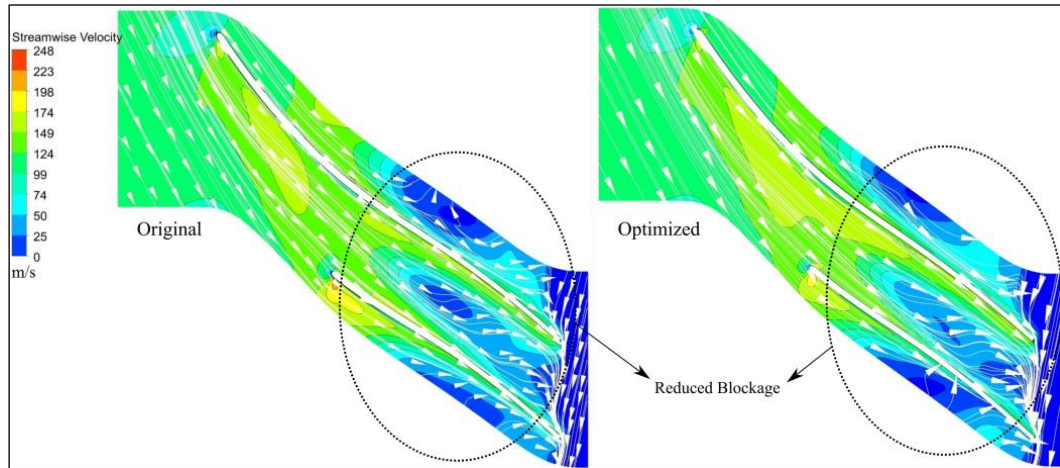
Source: Author.

To evaluate the robustness of an optimized centrifugal compressor found from the numerical methodology proposed in this paper, a Speedline displacement study was conducted to investigate the impact of different mass flow rates on polytropic efficiency, pressure ratio, and required power around an operating point, as shown in Figure 47. Figure 47a shows that the polytropic efficiency of the optimized centrifugal compressor is higher than the original

centrifugal compressor (from ANSYS VISTA CCD) for the whole mass flow rate investigated, showing that optimized geometry can be applied to a large mass flow rate range. Moreover, the pressure ratio (Figure 47b) and required power (Figure 47c) showed slight improvements, as they were only constraints in the optimization procedure. Thus, the optimized performance related to the optimized angles at the leading-edge and trailing-edge of the impeller is ensured not only at the operating point but also for different mass flows.

Figure 47 - Speedline displacement study (a) polytropic efficiency, (b) pressure ratio, (c) required power

(a)

(b)

(c)
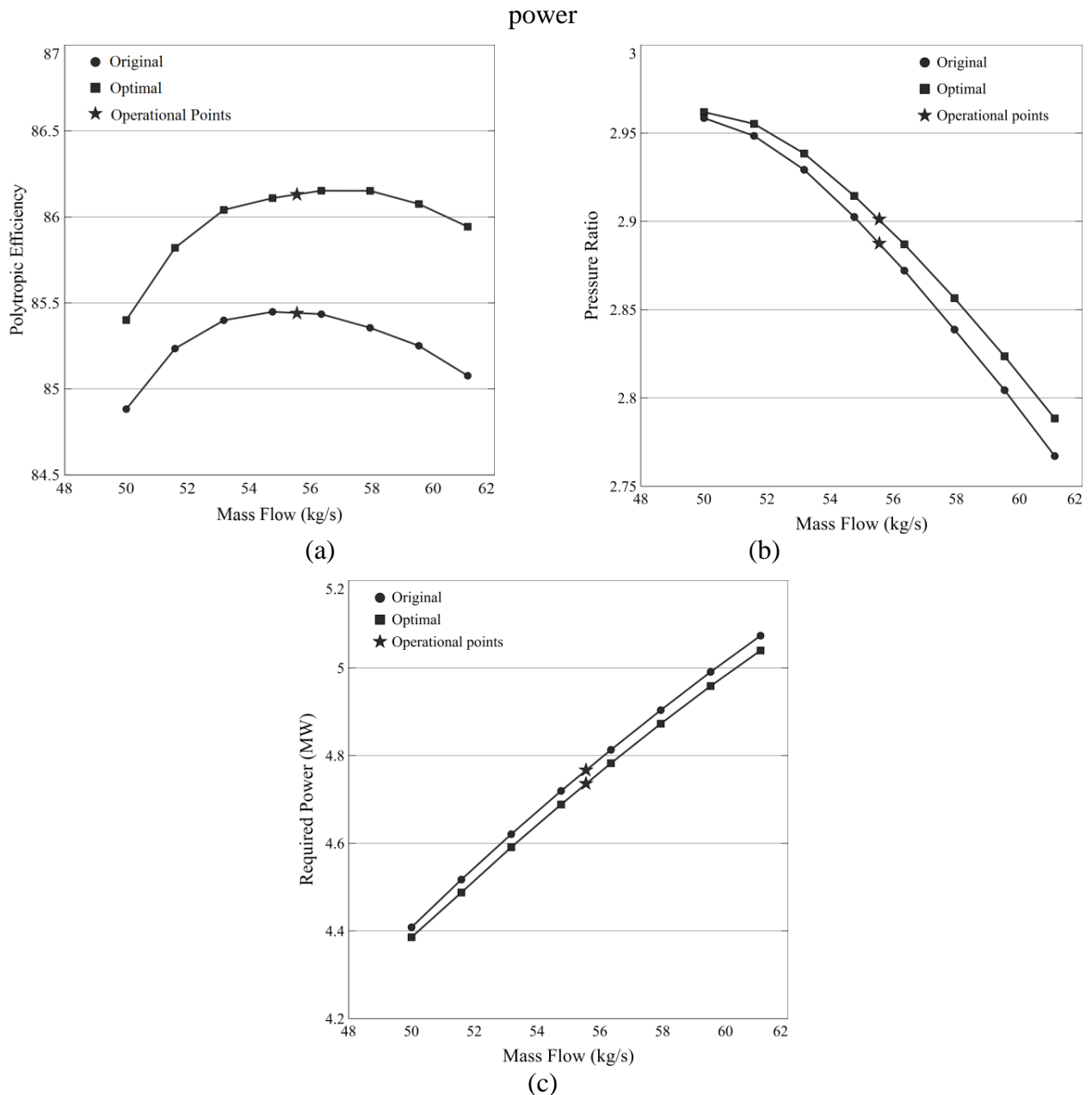
Source: Author.

For example, the cost savings regarding power consumption between optimized and original geometries in practical applications can be assessed by a simplified economic scenario. According to ANEEL (Agência Nacional de Energia Elétrica) (BRASIL, 2021), National Agency of Electrical Energy in Brazil, the country's average price of 1MWh is about US$100.00 (ANEEL, 2020). The optimized geometry has decreased the power required by 0.42% (0.02MW). Accounting for this saving in power consumption and considering that the compressor operates for a year (365 days), the cost savings potential is estimated by US$17,600.00 for each compressor. As well known, an oil exploration platform has many compressors which can make this saving even more relevant.

In short, centrifugal compressors performance is dependent on the number of geometric variables taken into account for turbomachinery design. The considerable increase in input variables could make 3D CFD analysis prohibitive as the computational time for sensitivity analysis and optimizations is huge. This work considered the intermediate polar angles, which are not optimized in Casey and Robinson's one-dimensional sizing method, have a significant impact on CO_2 centrifugal compressor polytropic efficiency, especially the angles near the trailing-edge. The optimized shape of the impeller reduced the flow blockage caused by the reverse flow, increasing the polytropic efficiency of 0.7%.

Moreover, Morris' screening method was applied for the first time to turbomachinery devices and showed that it is very reliable for factor-fixing purposes, even though few trajectories were initially used. This relatively cheap SA method agreed with the SS-ANOVA quantitative method, which needs huge computational resources. The use of Morris' method in turbomachinery is a promising tool that can effectively increase the number of design variables of a design allowing the simultaneous study of their impact on the equipment performance. Of course, the quasi-optimal sampling method used for generating Morris' method DoE ensured the excellent spreading of the sample space, which was adequate in RS training, reducing the need for new CFD simulations. This sampling can be applied to high-dimensional 3D CFD models, such as turbomachinery, to fit response surfaces with reduced computational costs.

Finally, phenomenological analysis of the dynamic flow found a significant source of losses at the leading-edge due to shockwaves and at the trailing-edge due to flow blockage. Morris' factor fixing predicted that polar angles had a greater influence on trailing-edge region phenomena, which was corroborated by the optimization results that eliminated leading-edge angles from the optimization procedure and increased polytropic efficiency of 0.64%. Considering all polar angles, the polytropic efficiency increased by 0.7%. The optimized centrifugal compressor was tested with different mass flow rates ensuring that the overall performance for the optimized angles of the trailing-edge and leading-edge of the impeller was higher than the original compressor for the whole operating speed line evaluated.

3.3 Sequential Sensitivity Analysis and Optimization Applied To the Fourth Compression Stage Centrifugal Compressor

This section presents the SA ranking of importance of the 25 variables for both Morris and SS-ANOVA methods, the CFD verification of the optimization through RS and the phenomenology analysis performed between original and optimized cases of the fourth stage compressor.

3.3.1 Sensitivity Analysis

Both DoE generated through the Quasi-OT sampling for RS training (containing 10 and 6 trajectories) were also used to assess the elementary effects of Morris' method on polytropic efficiency as shown in Figures 48 and 49. The strategy of increasing the number of trajectories using the Quasi-OT sampling was not adequate for RS training purposes and caused minor changes in variables ranking. Therefore, despite the good initial sample space screening provided by the original set of 10 trajectories, the authors recommend the usage of another sampling strategy (as ISF) to increase RS training quality, since the additional 6 Quasi-OT did not improve the RS training or Morris' variable ranking.

Figure 48 – Morris' elementary effects on polytropic efficiency (10 trajectories).
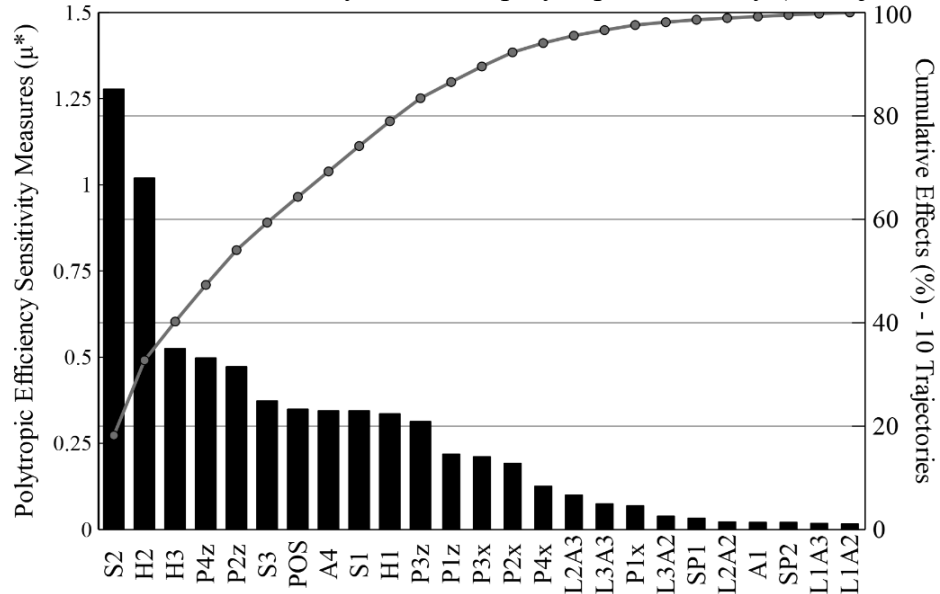
Source: Author.

Figure 49 – Morris' elementary effects on polytropic efficiency (16 trajectories).
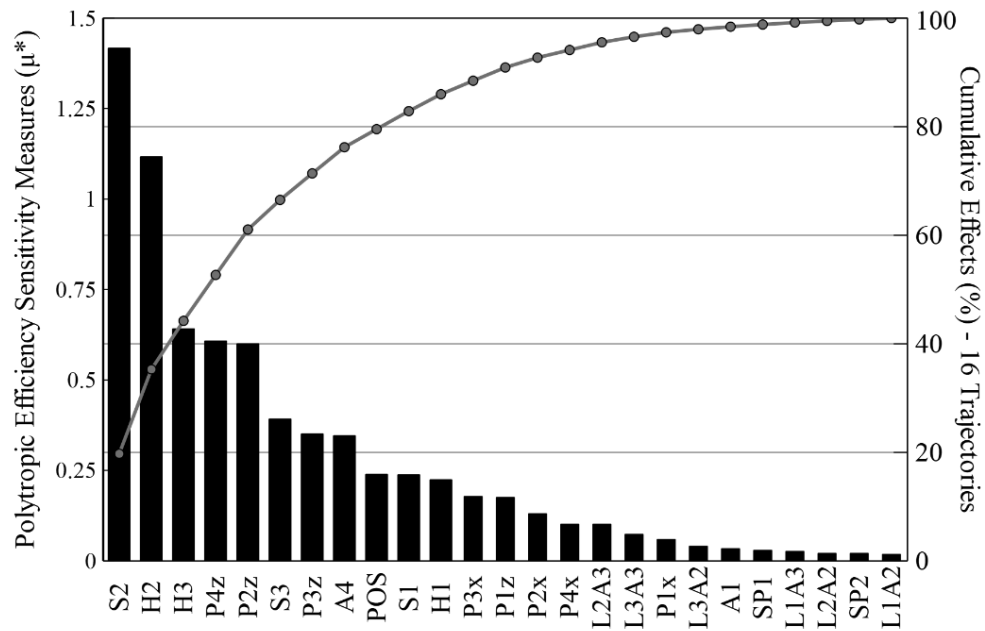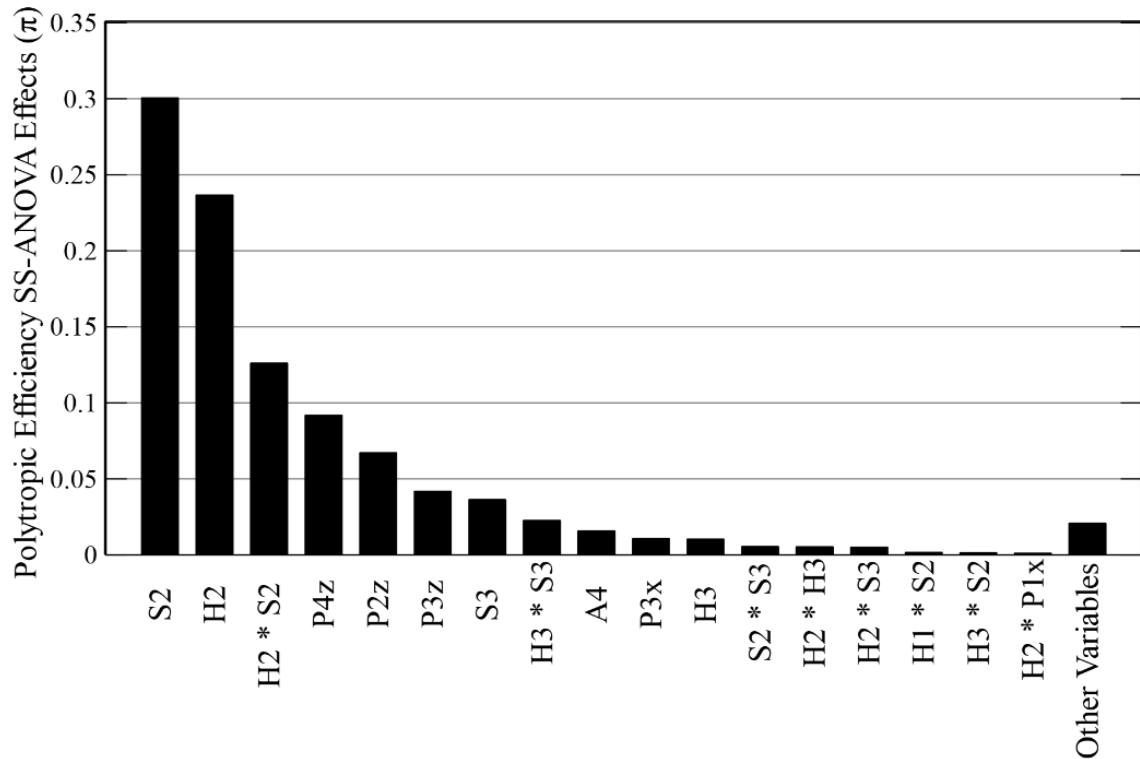

Source: Author.

Overall, Morris' method indicates that the variables positioned near the impeller trailing edge (P4z, P2z, A4) and at the diffuser (S1, H1, S2, H2, H3, and S3) are responsible for more than 75% of the accumulated main effects, which is better understood through phenomenology analysis, since these variables mitigate the flow recirculation identified at impeller/diffuser

interface. On the other hand, the polar angles along the blade (L1A2, L1A3, L2A2, L2A3, L3A2, L3A3 and A1) and leading-edge position of the splitter (SP1 and SP2) are negligible on polytropic efficiency main effects. Moreover, the meridional profile of the impeller beginning (P3x, P1x and P3x) and the blade-to-blade splitter position (POS) are variables without influence.

The SS-ANOVA method was also applied through the trained RS in order to identify interactions between variables, as presented in the histogram of Figure 50. Despite the RS inherent errors, both SA methods have found almost the same most the important variables (S2, H2, P4z, P2z, P3z, S3, A4, P3x and H3), with Morris' method also classifying POS, S1 and H1 as important variables, since it is a more conservative SA method than SS-ANOVA.

Figure 50 – SS-ANOVA histogram with interaction effects

Source: Author.

In summary, both SA methods indicate that the polar angles on the initial part of the impeller are not influent on polytropic efficiency, identifying only A4 (polar angle of trailing edge) as influential. The optimization of impeller blade angles alone did not achieve great improvement in isentropic efficiency in literature (EKRADI; MADADI, 2020; HILDEBRANDT; CEYROWSKY, 2019). On the other hand, the most important variables are present at the impeller/diffuser interface, which leads to the evaluation of the physical phenomena changes in

that region. Moreover, a thorough 'entropy-guided' phenomenon assessment is performed in the whole equipment to corroborate SA insights (Section 3.3).

Finally, the sequential SA conducted herein exposes that interactions between variables are not properly identified by Morris' method due to its 'one-at-a-time' DoE behavior provided by the Quasi-OT sampling, which also explains why the increase in the number of trajectories did not help the RS training. Moreover, the SS-ANOVA identified the interactions between variables H2/S2 and H2/S3 as more influential than the main effects of some design variables, reaffirming the importance of performing more than one SA method in high-dimensional models to have better insights into the model (SALTELLI *et al.*, 2019).

3.3.2 *Optimization*

The optimization procedure through trained RS considered all 25 variables and its nominal and optimized values are presented in Table 23 The number of cases necessary for achieving the convergence was 6000, which would be unfeasible using a direct approach through the expensive CFD model.

Table 23 – Variables' nominal and optimized values

Polar Angles			Meridional Profile			Diffuser		
Variable	Nom.	Opt.	Variable	Nom.	Opt.	Variable	Nom.	Opt.
A1 [°]	0	2	P1x [mm]	38.68	39.48	S1 [mm]	0	0.2
L1A2 [°]	-22.64	-21.6	P1z [mm]	8.38	9.19	S2 [mm]	3.48	3.08
L1A3 [°]	-42.37	-41.3	P2x [mm]	85.04	85.34	S3 [mm]	3.48	4.73
L2A2 [°]	-25.34	-24.3	P2z [mm]	0.82	0.16	H1 [mm]	0	0.2
L2A3 [°]	-44	-43	P3x [mm]	57.41	59.01	H2 [mm]	10	9.81
L3A2 [°]	-47.64	-46.6	P3z [mm]	13.07	14.67	H3 [mm]	10	10.22
L3A3 [°]	-44.34	-43.3	P4x [mm]	94.13	94.83	POS [%]	50	55
A4 [°]	-45	-45	P4z [mm]	4.35	5.05			
			SP1 [mm]	20.89	27.16			
			SP2 [mm]	24.41	25.63			

Source: Author.

The maximum polytropic efficiency indicated by the RS optimization was 83.34%, as presented in Table 24. In order to verify the efficiency improvement conceived by the RS strategy, the optimized geometry found was modeled by CFD and a verification analysis was performed. A polytropic efficiency of 82.93% was obtained with a numerical difference of 0.41% in comparison with the RS optimized geometry. Therefore, a significant increase of 1.19% in the polytropic efficiency is reached by comparing optimized and original geometries, since the mesh uncertainty for that variable was only 0.106%.

Table 24 – Polytropic efficiency of original and optimized geometries

| Model	Polytropic Efficiency	Improvement (%)
CFD Original Geometry	81.74 %	-
Response Surface Optimized Geometry	83.34 %	1.60%
CFD Optimized Geometry	82.93 %	1.19%

Source: Author.

Of course, the high number of variables present in the model has limited their range of variation and, therefore, the reach of an optimization procedure improvement in polytropic efficiency. However, it allowed the Morris' SA method evaluation for a high number of interacting variables (Section 3.3) and elucidated the advantages of using 'factor fixing' tools on large CFD models, since less variables would allow a larger range of variation on the most important variables.

The main differences between original and optimized geometries can be seen in Figure 51. The vaneless diffuser inlet was narrowed and the main passage channel between blade and splitter was larger. Also, the meridional profile has been enlarged in the transition from axial to the radial direction, which makes the flow smoother in this region.

The original geometry provided by the 1D method is already high-performance equipment. Therefore, the polytropic efficiency gain is a significant improvement which is demonstrated by the phenomenology analysis. Furthermore, the high number of variables (25) stickle to find optimized configurations since it limits the ranges of variation of the inputs, jeopardizing the

possibility of greater geometry modification. Thus, multiple optimization procedures contemplating smaller groups of variables with larger ranges of variations should be tested to assess even better improvements.

Figure 51 - Original and optimized geometries
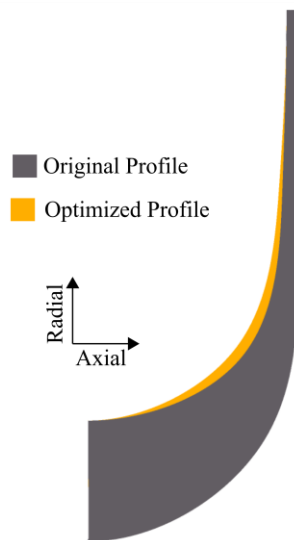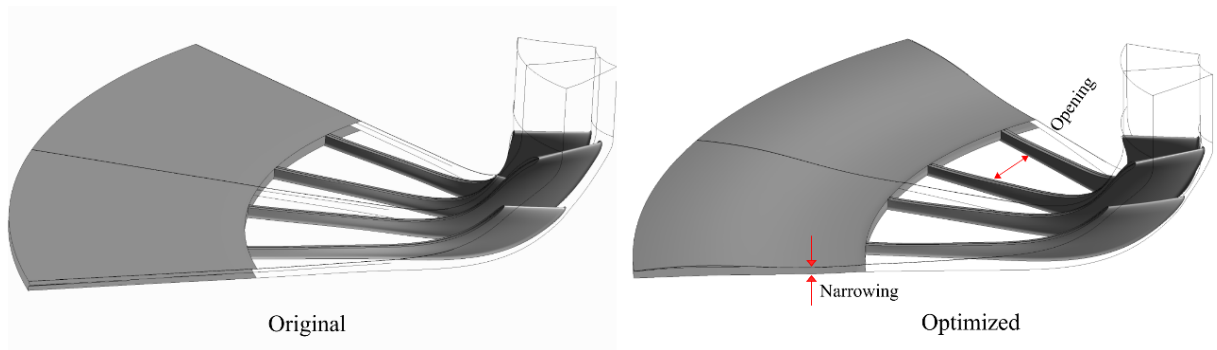
Source: Author.

Moreover, to corroborate the SA insights about the physical model, the computational symmetric domain was divided into 20 regions equally spaced along the streamwise direction as shown in Figure 52. The average entropy was performed at each hub-to-shroud section, allowing

to identify those physical phenomena responsible for efficiency losses. Overall, an entropy generation total reduction of 8.5% was found between original and optimized geometries. Thus, the entropy gain shown in Figure 3.26 indicates that the impeller/diffuser interface region was responsible for almost 75% of all entropy increases in the domain, according to SA results. Therefore, a phenomenology analysis can bring a better understanding of the changes in the physical mechanisms presented by the original and optimized geometries in that region.

Figure 52 – Computational symmetric domain regions and the entropy gain histogram
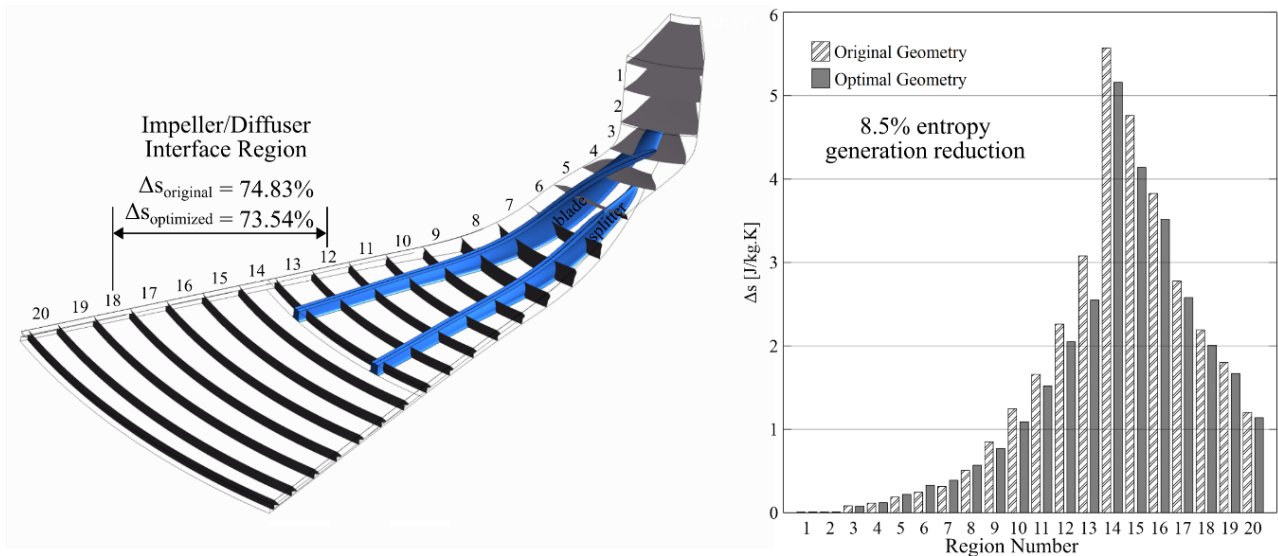
Source: Author.

3.3.3 Phenomenology Analysis

The phenomenology analysis initially focused on the impeller/diffuser interface region, since the entropy histogram discussed in Figure 52 indicated larger differences in that region. In fact, a backflow recirculation was identified, which increases fluid friction losses and causes a flow blockage near the impeller trailing edge, as evidenced by the streamlines on constant polar angle surfaces present at the original compressor in Figure 53.

Figure 53 – Surface streamlines on constant polar angle surfaces of the original geometry
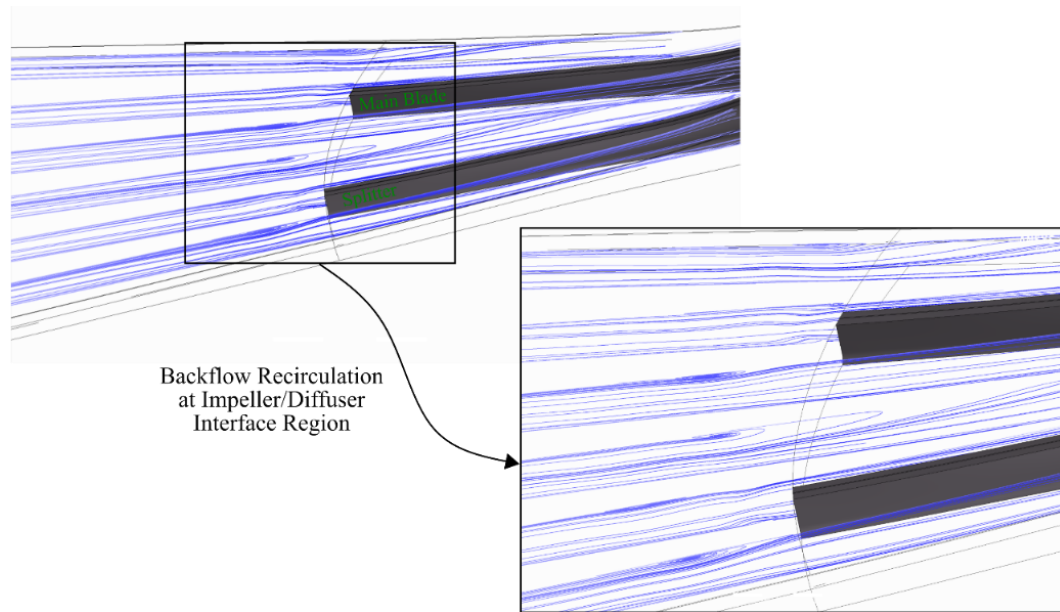
The CFD model investigation performed at the same region for the optimized geometry demonstrated the dissipation of the backflow recirculation present in the original model, as presented in Figure 54. The narrowing of the diffuser right after the trailing edge is responsible for smoothing the fluid flow in this region.

Figure 54 – Backflow recirculation dissipation at the optimized impeller/diffuser region
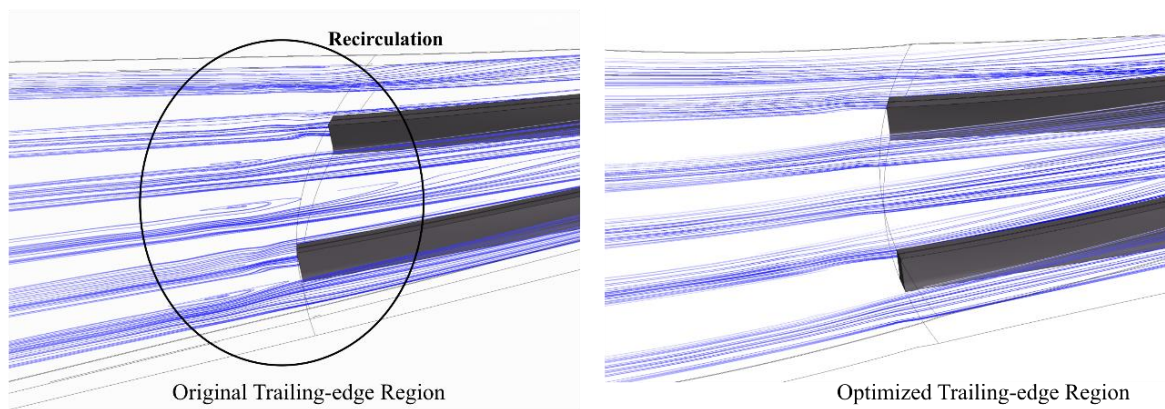
Furthermore, the flow blockage near the shroud caused by the recirculation was reduced by the optimization procedure as illustrated on the spanwise surfaces at 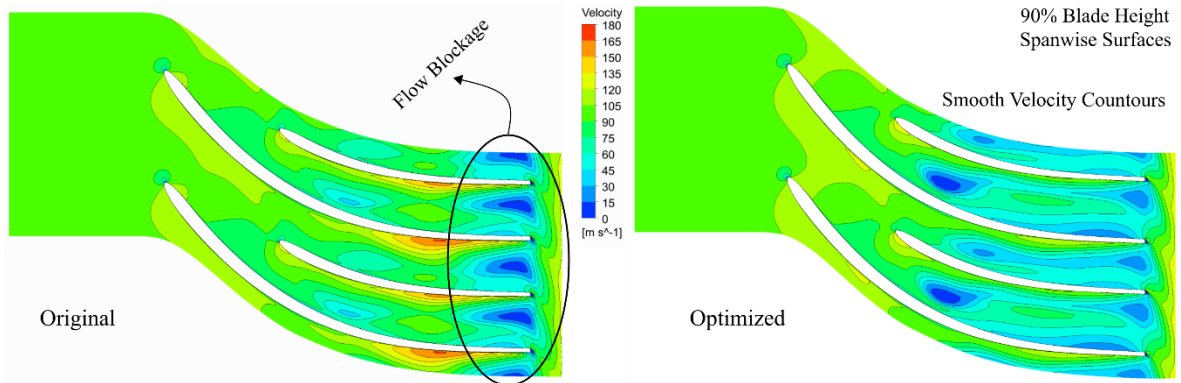90% of blade height in Figure 55. These fluid flow modifications decrease the entropy generation and, consequently, increase the polytropic efficiency.

Figure 55 – Velocity intensity near shroud for original and optimized geometries

Source: Author.

Moreover, significant differences are noticed in entropy generation inside the impeller, indicating that other loss mechanisms are present in this region. The flow structures known as swirls were identified after the change in the flow direction (from axial to radial) and propagated along the main channel (Figure 56), increasing their intensity until near the impeller trailing edge.

Figure 56 – Original geometry swirl structures and rotational direction in the main channel.
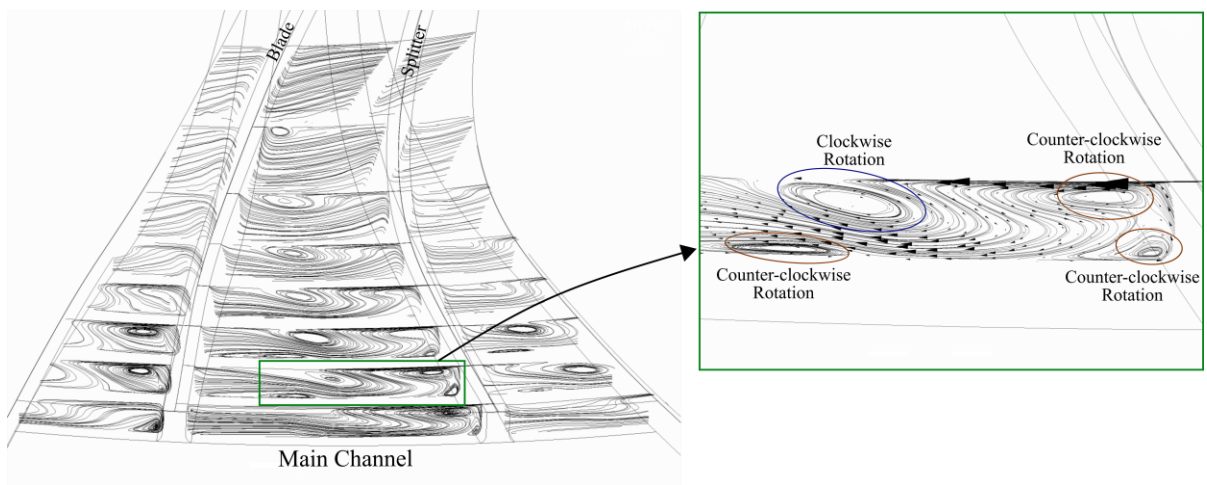
Source: Author.

The swirl structures in the main channel, highlighted in Figure 56, have opposite directions which indicates that the interaction between the main and corner vortex increases losses. Also, the same behavior was found in the secondary channels shown in Figure 57.

Figure 57 – Original geometry swirl structures and rotational direction in the secondary channel
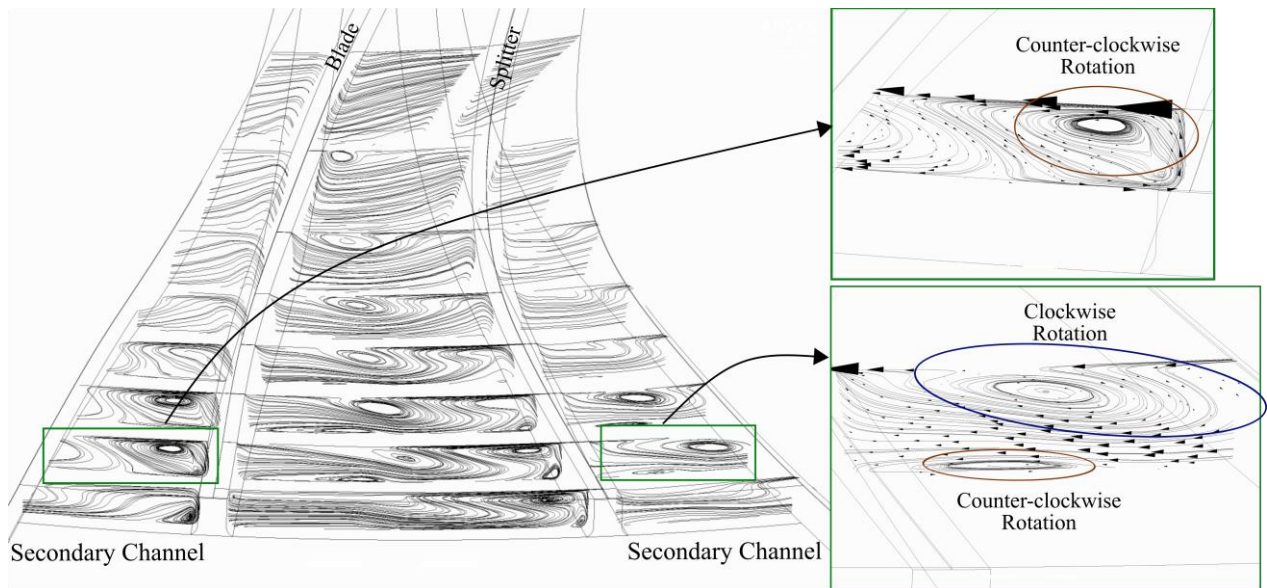
Source: Author.

In order to assess the impact of the optimization on this phenomenon, a comparison between original and optimized geometries is presented in Figure 58. A displacement of the main swirl structures was identified, which releases the flow restriction caused by the swirl near the trailing edge. Moreover, the secondary swirl structures were smoothed as well, which may be due to the splitter displacement indicated by the optimization.

Figure 58 – Swirl structures in the original and optimized geometry
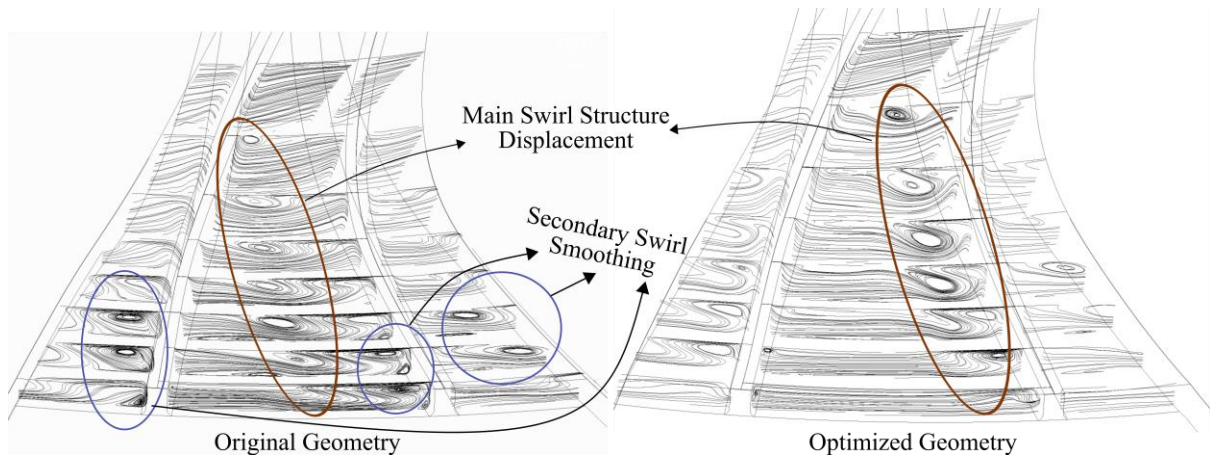
Source: Author.

Finally, a vortical structure was found at the impeller using the Q-Criterion (ZHANG *et al*., 2018) near the leading edge of the main blade, as shown in Figure 59. The vortex structure is formed next to the blade tip, stretching over the leading edge of the splitter. Although the polytropic efficiency has been increased by an optimization procedure, the optimized geometry was not able to extinguish this vortex since the main blade leading edge has a low-pressure suction region inherent to the rotational movement of the compressor and the clearance gap (DOMBARD *et al*., 2018).

Figure 59 – Vortical structure and low-pressure region on the original geometry
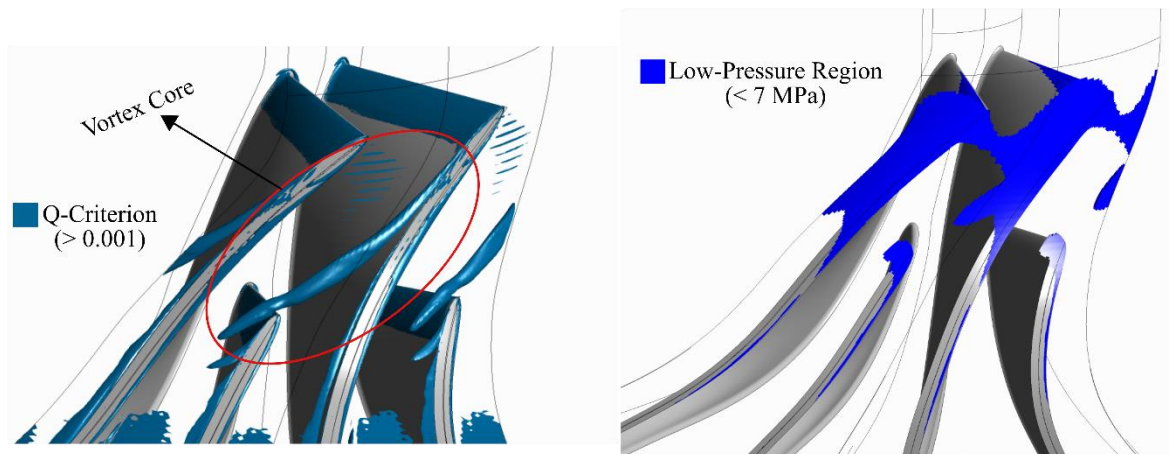
Source: Author.

4   CONCLUSIONS

A robust EOR compression system's design procedure has been developed in the present work. The 1D model of the whole system can provide high-performance preliminary geometries to the designer and CFD SA and optimization can deliver further improvements in the machine's fluid flow. The main conclusions of this thesis can be highlighted.

From the 1D optimization procedure:

- Direct thermodynamic analysis is not enough for a complete design of supercritical centrifugal compressors train since they do not take into account fluid flow phenomena such as the high change in the fluid properties close to Widom-line, throat Mach number and condensation. Therefore, the implemented 1D model and the Gas-like Behavior Margin (GBM) are able to circumvent the uncertainties of operating on the supercritical transitional region, ensuring suitable CFD convergence and physical analysis;

- The 1D calibration procedure was developed to adjust the preliminary geometry provided by the 1D method to the CFD outputs, which proved to be an effective strategy after numerical verification;

- The optimizer found a compression train system on the gas-like side, decreasing the total power consumed by 14.09%. The total power consumed by CFD modeling is higher than the 1D predictions due to three-dimensional loss phenomena. Nevertheless, a good agreement between numerical approaches is still verified, ensuring that the 1D code is robust for providing preliminary geometries;

From the first-stage CFD model SA and optimization procedure:

- The quasi-optimal sampling method used for generating Morris' method DoE ensured the excellent spreading of the sample space, which was adequate in RS training of additive models, reducing the need for new CFD simulations. This sampling can be applied to high-dimensional 3D CFD models, such as turbomachinery, to fit response surfaces with reduced computational costs;

- Morris' SA method was applied for the first time in turbomachinery devices and has proven to be a reliable tool to rank the main effects for factor fixing purposes. From this method, only 1.2% of SS-ANOVA clock time is used. Moreover, Morris' method is more conservative than SS-ANOVA methodology since it classifies less variables as non-important. The use of Morris' method in turbomachinery is a promising tool that can effectively increase the number of design variables of a design allowing the simultaneous study of their impact on the equipment performance;

From the fourth-stage CFD model SA and optimization procedure:

- An optimized design of a low-flow coefficient s-CO_2 centrifugal compressor (Φ = 0.01) with PR = 3.4 was obtained. The innovative strategy developed herein used a high-dimensional (25 variables) CFD model that was submitted to an indirect optimization procedure using a surrogate model, which has improved the polytropic efficiency of the equipment by 1.19%. This performance gain is able to increase even further the optimization performed using the previous 1D model. Moreover, a reduction of 8.5% in total entropy generation was achieved. This optimized machine can deliver significant reductions on EOR compression system's operational costs.
- The Morris' SA method was used to obtain insight of the variables' impact on polytropic efficiency and for screening the sample space, in order to train a RS that could properly represent the CFD model. However, the Quasi-OT sampling of Morris' method had to be combined with Incremental Space Filler (ISF) for proper RS training, exposing Morris' method limitation to properly screen a sample space containing interacting variables, which was accomplished by using the ISF sampling methodology, which still is indicated as a cheap combination of sampling strategies for RS training of large CFD models. Moreover, SS-ANOVA method identified interactions between variables that could not be assessed by Morris' SA due to its one-at-a-time DoE.
- A deep 'entropy-guided' phenomenological analysis of the main flow features for the optimized geometry has been carried out through streamlines and entropy behavior. This strategy identified the locations on the computational domain where the sources of losses were reduced, especially at the impeller/diffuser interface reducing the flow

recirculation present in the original geometry. Moreover, swirls were displaced and smoothed in the impeller. This phenomenology assessment strategy has speeded up the analysis of fluid flow behavior.

REFERENCES

AGRAWAL, N.; BHATTACHARYYA, S.; SARKAR, J. Optimization of two-stage transcritical carbon dioxide heat pump cycles. **International Journal of Thermal Sciences**, Issy les Moulineaux Cedex, v. 46, n. 2, p. 180–187, 2007.

AHN, Y. *et al*. Review of supercritical CO2 power cycle technology and current status of research and development. **Nuclear Engineering and Technology**, Daejeon, v. 47, n. 6, p. 647–661, 2015.

ALLAHYARZADEH-BIDGOLI, A. *et al*. FPSO fuel consumption and hydrocarbon liquids recovery optimization over the lifetime of a deep-water oil field. **Energy**, London, v. 181, p. 927–942, 2019a.

ALLAHYARZADEH-BIDGOLI, A. *et al*. Lifetime sensitivity analysis of FPSO operating parameters on energy consumption and overall oil production in a pre-salt oil field. **Chemical Engineering Communications**, New York, v. 207, n. 11, p. 1483–1507, 2019b.

ALLAHYARZADEH-BIDGOLI, A. *et al*. Thermodynamic analysis and optimization of a multi-stage compression system for CO2 injection unit: NSGA-II and gradient-based methods. **Journal of the Brazilian Society of Mechanical Sciences and Engineering**, Heidelberg, v. 43, n. 10, p. 458, 14 out. 2021.

ALLISON, T. C. *et al*. Experimental validation of a wide-range centrifugal compressor stage for supercritical CO 2 power cycles. **Journal of Engineering for Gas Turbines and Power**, New York, v. 141, n. 6, p. 1–11, 2019.

AMELI, A. *et al*. Effects of Real Gas Model Accuracy and Operating Conditions on Supercritical CO 2 Compressor Performance and Flow Field. **Journal of Engineering for Gas Turbines and Power**, New York, v. 140, n. 6, p. 062603, 2017.

AMELI, A. *et al*. Compressor design method in the supercritical CO2 applications. *In*: INTERNATIONAL SYMPOSIUM - SUPERCRITICAL CO2 POWER CYCLES, 6yh., 2018, Pittsburgh. **Proceedings** […] [*S. l.: s. n*.], 2018.

AMELI, A. *et al*. Centrifugal compressor design for near-critical point applications. **Journal of Engineering for Gas Turbines and Power**, New York, v. 141, n. 3, 2019.

AMELI, A.; TURUNEN-SAARESTI, T.; BACKMAN, J. Numerical Investigation of the Flow Behavior Inside a Supercritical CO 2 Centrifugal Compressor . **Journal of Engineering for Gas Turbines and Power**, New York, v. 140, n. 12, p. 122604, 2018.

AUNGIER, R. H. A fast, accurate real gas equation of state for fluid dynamic analysis applications. **Journal of Fluids Engineering**, New York, v. 117, n. 2, p. 277–281, 1995.

AUNGIER, R. H. **Centrifugal compressors**: a strategy for aerodynamic design and analysis.

New York: ASME, 2000. v. 53.

AZIZIFAR, S.; BANOONI, S. Modeling and optimization of industrial multistage compressed air system using actual variable effectiveness in hot regions. **Advances in Mechanical Engineering**, London, v. 8, n. 5, p. 1–10, 2016.

BAE, S. J. *et al*. Comparison of gas system analysis code GAMMA+ to S-CO2 compressor test data. *In*: TURBINE TECHNICAL CONFERENCE AND EXPOSITION, 2015. **Proceedings** [...] [*S. l.*]: American Society of Mechanical Engineers, 2015, [*s. l.*]. Disponível em: https://asmedigitalcollection.asme.org/GT/proceedings/GT2015/56802/Montreal, Quebec, Canada/238348.

BALJE, O. E. Aerodynamic and Geometric Design Criteria for the Performance of Low Powered Vehicular Gas Turbines. **Gas Turbine and Power**, [*s. l.*], v. 103, p. 158–167, 1981.

BALTADJIEV, N.; LETTIERI, C.; SPAKOVSZKY, Z. An Investigation of Real Gas Effects in Supercritical CO 2 Centrifugal Compressors. **Journal of Turbomachinery**, New York, v. 137, n. September, p. 13, 2014.

BELL, I. H. *et al*. Pure and pseudo-pure fluid thermophysical property evaluation and the open-source thermophysical property library coolprop. **Industrial and Engineering Chemistry Research**, Washington, v. 53, n. 6, p. 2498–2508, 2014.

BENEDICT, R. P.; CARLUCCI, N. A.; SWETZ, S. D. Flow Losses in Abrupt Enlargements and Contractions. **Journal of Engineering for Power**, New York, p. 73–81, 1966.

BENINI, E.; TOFFOLO, A.; LAZZARETTO, A. Experimental and numerical analyses to enhance the performance of a microturbine diffuser. **Experimental Thermal and Fluid Science**, Philadelphia, v. 30, n. 5, p. 427–440, 2006.

BILAL, N. Implementation of Sobol ' s method of global sensitivity analysis to a compressor simulation model. *In*: INTERNATIONAL COMPRESSOR ENGINEERING CONFERENCE, 2014, [s. l.]. **Anais** [...] Purdue: [*s. n*], 2014.

BLANCHETTE, L. *et al*. Two types of analytical methods for a centrifugal compressor impeller for supercritical CO2 Power Cycles. *In*: INTERNATIONAL ENERGY CONVERSION ENGINEERING CONFERENCE AIAA, 14th, 2016, [*s. l.*]. **Proceedings** ... Salt Lake City: American Institute of Aeronautics and Astronautics, 2016

BOURGEOIS, J. A. *et al*. Assessment of turbulence model predictions for an aero-engine centrifugal compressor. **Journal of Turbomachinery**, New York, v. 133, n. 1, p. 1–15, 2011.

BRASIL. Agência Nacional de Energia Elétrica - ANAEEL. **Ranking nacional de tarifas**. Brasília, DF, 2023. Disponível em: https://www.aneel.gov.br/ranking-das-tarifas.

CALADO, P. A. Modeling and design synthesis of a CCS compression train system via MINLP optimization. **Tecnico Lisboa**, n. October, p. 1–122, 2012.

CAMPOLONGO, F.; CARIBONI, J.; SALTELLI, A. An effective screening design for sensitivity analysis of large models. **Environmental Modelling and Software**, Oxford, v. 22, n. 10, p. 1509–1518, 2007.

CAMPOLONGO, F.; SALTELLI, A.; CARIBONI, J. From screening to quantitative sensitivity analysis. A unified approach. **Computer Physics Communications**, Amsterdam, v. 182, n. 4, p. 978–988, 2011.

CASEY, M.; ROBINSON, C. A new streamline curvature throughflow method for radial turbomachinery. *In*: ASME TURBO EXPO, 2006, [*s. l.*]. **Anais** [...] [*S. l.: s. n.*], 2008a.

CASEY, M.; ROBINSON, C. A new streamline curvature throughflow method for radial turbomachinery. *In*: TURBO EXPO. **Anais [**...] Berlim: ASME, 2008b.

CASEY, M.; ROBINSON, C. A Method to Estimate the Performance Map of a Centrifugal Compressor Stage. **Journal of Turbomachinery**, New York, v. 135, n. 2, p. 1–10, 2013.

CELIK, I. B. *et al*. Procedure for Estimation and Reporting of Uncertainty Due to Discretization in CFD Applications. **Journal of Fluids Engineering**, New York, v. 130, n. 7, p. 1–4, 2008.

CHA, J. E. *et al*. 500 kW supercritical CO2 power generation system for waste heat recovery: System design and compressor performance test results. **Applied Thermal Engineering**, Oxford, v. 194, 25 jul. 2021.

CHEN, L. *et al*. Design efficiency optimization of one-dimensional multi-stage axial-flow compressor. **Applied Energy**, v. 85, n. 7, p. 625–633, 2008.

CHO, S. K. *et al*. Optimum loss models for performance prediction of supercritical CO2 centrifugal compressor. **Applied Thermal Engineering**, Oxford, v. 184, n. May 2020, p. 116255, 2021.

CIUFFO, B. *et al*. Gaussian Process Metamodels for Sensitivity Analysis of Traffic Simulation Models. **Journal of the Transportation Research Board**, [*s. l.*], v. 2390, n. 1, p. 87–98, 2013.

DEB, K. *et al*. A fast and elitist multiobjective genetic algorithm: NSGA-II. **IEEE Transactions on Evolutionary Computation**, Piscataway, v. 6, n. 2, p. 182–197, 2002.

DEZAN, D. J. *et al*. Parametric investigation of heat transfer enhancement and pressure loss in louvered fins with longitudinal vortex generators. **International Journal of Thermal Sciences**, Issy les Moulineaux Cedex, v. 135, p. 533–545, 2018.

DOMBARD, J. *et al*. Large eddy simulations in a transonic centrifugal compressor. *In*: ASME TURBO EXPO, 2018, [*s. l.*]. **Anais [**...] Oslo, Norway: ASME, 2018.

DU, Y. *et al*. Design and performance analysis of compressor and turbine in supercritical CO2 power cycle based on system-component coupled optimization. **Energy Conversion and**

Management, London, v. 221, n. July, p. 113179, 2020.

DU, Y. *et al*. One-dimensional optimisation design and off-design operation strategy of centrifugal compressor for supercritical carbon dioxide Brayton cycle. **Applied Thermal Engineering**, Oxford, v. 196, n. June, p. 117318, 2021.

EKRADI, K.; MADADI, A. Performance improvement of a transonic centrifugal compressor impeller with splitter blade by three-dimensional optimization. **Energy**, London, v. 201, p. 117582, 2020.

FILLON, C. **New strategies for efficient and practical genetic programming**. [*S. l.*]: Università degli Studi di Trieste, 2008.

FULLER, R.; PREUSS, J.; NOALL, J. Turbomachinery For Supercritical CO2 Power Cycles. *In*: ASME TURBO EXPO, 2012, [*s. l.*]. **Anais** [...] Copenhagen, Denmark: ASME, 2012.

GARCIA, D.; AROSTEGUI, I.; PRELLEZO, R. Robust combination of the Morris and Sobol methods in complex multidimensional models. **Environmental Modelling and Software**, Oxford, v. 122, n. September, p. 104517, 2019.

GE, Q.; CIUFFO, B.; MENENDEZ, M. Combining screening and metamodel-based methods: An efficient sequential approach for the sensitivity analysis of model outputs. **Reliability Engineering and System Safety**, London, v. 134, p. 334–344, 2014.

GODEC, M. *et al*. CO2 storage in depleted oil fields: The worldwide potential for carbon dioxide enhanced oil recovery. **Energy Procedia**, Amsterdam, v. 4, p. 2162–2169, 2011.

GODOI, J. M. A.; DOS SANTOS MATAI, P. H. L. Enhanced oil recovery with carbon dioxide geosequestration: first steps at Pre-salt in Brazil. **Journal of Petroleum Exploration and Production**, Heidelberg, v. 11, n. 3, p. 1429–1441, 2021.

GU, C. **Smoothing Spline ANOVA Models**. New York: Springer-Verlag, 2002.

HAYKIN, S. **Neural networks**: a comprehensive foundation. Hamilton, Canada: Pearson Education, 1999.

HE, Q. *et al*. Thermodynamic analysis of a novel supercritical compressed carbon dioxide energy storage system through advanced exergy analysis. **Renewable Energy**, Oxford, v. 127, p. 835–849, 2018.

HEINRICH, M. **Genetic optimization of the volute of a centrifugal compressor**. [*S. l: s. n.*], 2016.

HILDEBRANDT, A.; CEYROWSKY, T. One-dimensional and three- dimensional design strategies for pressure slope optimization of high-flow transonic centrifugal compressor impellers. **Journal of Turbomachinery**, New York, v. 141, n. 5, 2019.

HOSANGADI, A. *et al*. Numerical Simulations of CO 2 Compressors at Near-Critical and Sub-Critical Inlet Conditions . n. May, p. V009T38A002, 2018.

IBARAKI, S. *et al*. Aerodynamics of a transonic centrifugal compressor impeller. *In*: TURBO EXPO, 2002, [*s. l.*]. **Anais** [...] Amsterdam: ASME, 2002.

IBARAKI, S. *et al*. Vortical flow structure and loss generation process in a transonic centrifugal compressor impeller. *In*: ASME TURBO EXPO, 2007, [*s. l.*]. **Proceedings** […] Canada: [*s. n.*], 2007.

JAVED, A.; PECNIK, R.; VAN BUIJTENEN, J. P. Optimization of a Centrifugal Compressor Impeller for Robustness to Manufacturing Uncertainties. **Journal of Engineering for Gas Turbines and Power**, New York, v. 138, n. 11, p. 1–11, 2016.

JENSEN, H. A.; MAYORGA, F.; PAPADIMITRIOU, C. Reliability sensitivity analysis of stochastic finite element models. **Computer Methods in Applied Mechanics and Engineering**, Amsterdam, v. 296, p. 327–351, 2015.

KIM, J. H. *et al*. Multi-objective optimization of a centrifugal compressor impeller through evolutionary algorithms. **Journal of Power and Energy**, London, v. 224, n. 5, p. 711–721, 2010.

KIM, Y. J.; GU, C. Smoothing spline Gaussian regression: more scalable computation via efficient approximation. **Journal of the Royal Statistical Society**, [*s. l.*], v. 66, n. 2, p. 337–356, 2004.

KLAUSNER, E.; GAMPE, U. Evaluation and enhancement of a one-dimensional performance analysis method for centrifugal compressors. *In*: ASME TURBO EXPO, 2014, [*s. l.*]. **Proceedings** […] [*S. l.*]: ASME, 2014.

KLEIJNEN, J. P. C. Sensitivity Analysis of Simulation Models. **CentER Discussion Paper**, [*s. l.*], v. 2009–11, p. 1–14, 2009.

KNOPP, T.; ALRUTZ, T.; SCHWAMBORN, D. A grid and flow adaptive wall-function method for RANS turbulence modelling. **Journal of Computational Physics**, Maryland Heights, v. 220, n. 1, p. 19–40, 2006.

KOOHESTANIAN, E. *et al*. Sensitivity analysis and multi-objective optimization of CO2CPU process using response surface methodology. **Energy**, London, v. 122, p. 570–578, 2017.

KULKARNI, S.; BEACH, T. A.; SKOCH, G. J. Computational Study of the CC3 Impeller and Vaneless Diffuser Experiment. *In*: AIAA/ASME/SAE/ASEE Joint Propulsion Conference, 49th, 2013, [*s. l.*]. **Proceedings** […] [*S. l.*]: American Institute of Aeronautics and Astronautics, 2013.

LEE, J. *et al*. Issues in performance measurement of CO2 compressor near the critical point. **Applied Thermal Engineering**, Oxford, v. 94, p. 111–121, 2016.

LETTIERI, C. *et al*. Low-Flow-Coefficient Centrifugal Compressor Design for Supercritical CO2. **Journal of Turbomachinery**, New York, v. 136, n. 8, p. 1–9, 1 ago. 2014.

LETTIERI, C.; YANG, D.; SPAKOVSZKY, Z. An investigation of condensation effects in supercritical carbon dioxide compressors. **Journal of Engineering for Gas Turbines and Power**, New York, v. 137, n. 8, p. 1–8, 2015.

LI, X.; ZHAO, Y.; LIU, Z. A novel global optimization algorithm and data-mining methods for turbomachinery design. **Structural and Multidisciplinary Optimization**, Heidelberg, v. 60, n. 2, p. 581–612, 2019.

LIU, Y.; WANG, Y.; HUANG, D. Supercritical CO2 Brayton cycle: A state-of-the-art review. **Energy**, London,v. 189, p. 115900, 2019.

LOEWENTHAL, H. **Design of power-transmitting shafts**. Cleveland: [*s. n.*], 1984.

LUO, X. *et al*. Modelling study, efficiency analysis and optimisation of large-scale Adiabatic Compressed Air Energy Storage systems with low-temperature thermal storage. **Applied Energy**, Oxford, v. 162, p. 589–600, 2016.

MARCONCINI, M. *et al*. Numerical investigation of a transonic centrifugal compressor. **Journal of Turbomachinery ASME**, [*s. l.*], v. 130, n. January, p. 1005–1012, 2008.

MARTYNOV, S. B. *et al*. Impact of stream impurities on compressor power requirements for CO2 pipeline transportation. **International Journal of Greenhouse Gas Control**, London, v. 54, p. 652–661, 2016.

MCKAY, M. D.; BECKMAN, R. J.; CONOVER, W. J. Comparison of three methods for selecting values of input variables in the analysis of output from a computer code. **Technometrics**, Philadelphia, v. 21, n. 2, p. 239–245, 1979.

MENTER, F. R. Two-equation eddy-viscosity turbulence models for engineering applications. **AIAA Journal**, Reston, v. 32, n. 8, p. 1598–1605, 1994.

MENTER, F. R. Review of the shear-stress transport turbulence model experience from an industrial perspective. **International Journal of Computational Fluid Dynamics**, Abingdon, v. 23, n. 4, p. 305–316, 2009.

MERONI, A. *et al*. Design of centrifugal compressors for heat pump systems. **Applied Energy**, Oxford, v. 232, n. September, p. 139–156, 2018.

MODEKURTI, S. *et al*. Design, dynamic modeling, and control of a multistage CO2 compression system. **International Journal of Greenhouse Gas Control**, London, v. 62, p. 31–45, 2017.

MONJE, B. *et al*. A Design Strategy for Supercritical CO2 Compressors. *In*: ASME TURBO EXPO, 2014, [*s. l.*]. **Proceedings** […] Dusseldorf: ASME, 2014.

MONTRONE, T. *et al*. **New greedy incremental space filler in mf 2019**: benchmark tests. [*S. l: s. n.*], 2019.

MORRIS, M. D. Factorial Sampling Plans for Preliminary Computational Experiments. **Technometrics**, Philadelphia, v. 33, p. 161–174, 1991.

NIMTZ, M. *et al*. Modelling of the CO2 process- and transport chain in CCS systems—Examination of transport and storage processes. **Chemie der Erde**, [*s. l.*], v. 70, n. suppl. 3, p. 185–192, 2010.

OH, H. W.; YOON, E. S.; CHUNG, M. K. An optimum set of loss models for performance prediction of centrifugal compressors. **Proceedings of the Institution of Mechanical Engineers, Part A: Journal of Power and Energy**, London, v. 2011, n. 4, 1997.

OKEZUE, C.; KUVSHINOV, D. Effect of Chemical Impurities on Centrifugal Machine Performance: Implications for Compressor Sizing in A CO2 Transport Pipeline. **Energy Procedia**, Amsterdam, v. 142, p. 3675–3682, 2017.

PARK, J. H.; CHA, J. E.; LEE, S. W. Experimental investigation on performance test of 150-kW-class supercritical CO2 centrifugal compressor. **Applied Thermal Engineering**, Oxford, v. 210, n. 1, p. 118310, jun. 2022.

R.SPAN; W.WAGNER. A New Equation of State for Carbon Dioxide Covering the Fluid Region from the Triple-Point Temperature to 1100 K Pressures up to 800 MPa. **Jornal of Chemical**, [*s. l.*], v. 25, n. 6, 1994.

RAO, S. S. **Engineering optimization**: theory and practice. 4th. ed. [*S. l: s. n.*], 2009.

RASMUSSEN, C. E.; WILLIAMS, C. K. I. **Gaussian processes for machine learning**. Massachusetts: The MIT, 2006. v. 7.

RATTO, M.; PAGANO, A. Using recursive algorithms for the efficient identification of smoothing spline ANOVA models. **Advances in Statistical Analysis**, [*s. l.*], v. 94, n. 4, p. 367–388, 2010.

RIGONI, E. **Technical report of radial basis functions response surfaces**. Italy: ESTECO, 2007.

RIGONI, E. **Technical Report of Stepwise Regression RSM**. Italy: ESTECO, 2014.

RIGONI, E.; RICCO, L. **Technical Report of Smoothing Spline ANOVA for Variable Screening**. Italy: ESTECO, 2011.

ROBINSON, C. *et al*. Impeller-diffuser interaction in centrifugal compressors. *In*: TURBO EXPO, 2012, [*s. l.*]. **Proceedings** […] Copenhagen, Denmark: ASME, 2012.

ROCKETT, G. C. *et al*. CO2 storage capacity of Campos Basin's oil fields, Brazil. **Energy Procedia**, Amsterdam, v. 37, p. 5124–5133, 2013.

RODGERS, C. Development of a High-Specific- Speed Centrifugal Compressor. **Journal of Turbomachinery**, New York, v. 1, n. July, p. 1–5, 1997.

ROMEI, A.; GAETANI, P.; PERSICO, G. Computational fluid-dynamic investigation of a centrifugal compressor with inlet guide vanes for supercritical carbon dioxide power systems. **Energy**, London, v. 255, p. 124469, 2022.

SALTELLI, A. *et al*. **Global sensitivity analysis**: the primer. Chichester: John Wiley & Sons, 2008.

SALTELLI, A. *et al*. Why so many published sensitivity analyses are false: A systematic review of sensitivity analysis practices. **Environmental Modelling and Software**, Oxford, v. 114, n. March 2018, p. 29–39, 2019.

SALVIANO, L. O. *et al*. Sensitivity analysis and optimization of a CO2 centrifugal compressor impeller with a vaneless diffuser. **Structural and Multidisciplinary Optimization**, Heidelberg, n. 2008, 2021.

SCHLICHTING, H. **Boundary layer theory**. 7th. ed. [*S. l: s.n.*], 1979.

SHAO, W. *et al*. Design parameters exploration for supercritical co2 centrifugal compressors under multiple constraints. *In*: ASME Turbo Expo. **Proceedings** […] Seoul, South Korea: ASME, 2016.

SIMEONI, G. G. *et al*. The Widom line as the crossover between liquid-like and gas-like behaviour in supercritical fluids. **Nature Physics**, London, v. 6, n. 7, p. 503–507, 2010.

STANITZ, J. D. **One-dimensional compressible flow in vaneless diffusers of radial- and mixed-flow centrifugal compressors, including effects of friction, heat transfer and area changenational advisory committee for aeronautics**. Cleveland, Ohio: [*s. n.*], 1952.

SUN, L. *et al*. Assessment of CO2 storage potential and carbon capture, utilization and storage prospect in China. **Journal of the Energy Institute**, Kidlington, v. 91, n. 6, p. 970–977, 2018.

SUNDSTRÖM, E.; SEMLITSCH, B.; MIHĂESCU, M. Generation Mechanisms of Rotating Stall and Surge in Centrifugal Compressors. **Flow, Turbulence and Combustion**, Dordrecht, v. 100, n. 3, p. 705–719, 2018.

VANROLLEGHEM, P. A. *et al*. Global sensitivity analysis for urban water quality modelling: Terminology, convergence and comparison of different methods. **Journal of Hydrology**, Amsterdam, v. 522, p. 339–352, 2015.

VILLA-VIALANEIX, N. *et al*. A comparison of eight metamodeling techniques for the simulation of N2O fluxes and N leaching from corn crops. **Environmental Modelling and Software**, Oxford, v. 34, p. 51–66, 2012.

WANG, X. D. *et al*. Multi-objective optimization of turbomachinery using improved NSGA-II and approximation model. **Computer Methods in Applied Mechanics and Engineering**, Amsterdam, v. 200, n. 9–12, p. 883–895, 2011.

WIESNER, F. J. A Review of Slip Factors for Centrifugal Impellers. **Journal of Engineering for Power**, New York, v. 89, n. 4, p. 558–566, 1967.

WRIGHT, S. *et al*. **Operation and analysis of a supercritical CO2 Brayton cycle.Sandia National Laboratories**. Livermore: [*s. n.*], 2010. Disponível em: https://www.osti.gov/servlets/purl/984129. Accessed March 1.

XIA, W. *et al*. Aerodynamic design and multi-dimensional performance optimization of supercritical CO2 centrifugal compressor. **Energy Conversion and Management**, London, v. 248, n. 28, p. 114810, 2021.

XU, L. *et al*. Sensitivity analysis method for model with correlated inputs and multivariate output and its application to aircraft structure. **Computer Methods in Applied Mechanics and Engineering**, Amsterdam, v. 355, p. 373–404, 2019.

XU, M. *et al*. Preliminary design and performance assessment of compressed supercritical carbon dioxide energy storage system. **Applied Thermal Engineering**, Oxford, v. 183, n. p1, p. 116153, 2021.

YANG, J. *et al*. Stator re-stagger optimization in multistage axial compressor. **Propulsion and Power Research**, Reston, v. 10, n. 2, p. 107–117, 2021.

ZHANG, Y. *et al*. A review of methods for vortex identification in hydroturbines. **Renewable and Sustainable Energy Reviews**, Oxford, v. 81, n. May 2017, p. 1269–1285, 2018.

ZHU, Y. *et al*. Experimental Study on a Supercritical CO2 Centrifugal Compressor Used in a MWe Scale Power Cycle. **Applied Sciences**, Basel, v. 13, n. 1, 1 jan. 2023.

Research Prospecting

Finally, some future investigations and comments that appeared during the conducted research are worth mentioning:

- Morris' SA method is not able to predict the interactions between variables alone. Therefore, the implementation of other SA screening (cheap) methods that can identify interactions to precede the Morris' method is under consideration (Fractional Factorial Sampling)
- Application of novel RS regression methods could improve functions training quality.
- The 1D model needs to be improved to admit mixtures, as the widely employed in oil industry: CO_2/CH_4.
- Function training for 1D/CFD calibration procedure can complement the 1D model and speed-up the preliminary geometry generation.
- The high number of variables in a model has limited their range of variation. Demonstrating the advantages of using 'factor fixing' tools in order to perform an optimization with less variables and wider ranges of variation.
- The vortices' structure responsible for decreasing the machine's performance are created at the leading-edge and its shape from hub-to-shroud or the insertion of protuberances on blade walls are going to be considered in further studies.
- The operational range of centrifugal compressors is delimited by surge and choke lines, we intend to evaluate the impact of geometrical changes on these lines.
- Transient modeling for better understanding of phenomenological improvements provided by the optimization. Also, so compressors with vaned diffuser can be properly studied.

OUTCOMES

- **Title:** Constrained optimization of sCO2 compression train system through 1D approach under a new gas-like behavior constraint
Authors: Elóy Gasparin; Vitor Mattos; Gustavo Gonçalves; Fabio Saltara; Paulo Mello; Daniel Dezan; Jurandir Yanagihara; Leandro Salviano.
Journal: The Journal of Supercritical Fluids (2023) - JCR 2021 = 4.514
Status: Published.

- **Title:** High-dimensional CFD optimization of a low-flow coefficient S-CO2 centrifugal compressor for enhanced oil recovery systems
Authors: Elóy Gasparin; Vitor Mattos; Fabio Saltara; Paulo Mello; Daniel Dezan; Leandro Salviano; Jurandir Yanagihara.
Journal: Geoenergy Science and Engineering (2023) - Former Journal of Petroleum Science and Engineering - JCR 2021 = 5.168
Status: Published.

- **Title:** Sensitivity Analysis and Optimization of a CO2 Centrifugal Compressor Impeller with a Vaneless Diffuser
Authors: Leandro Salviano; Elóy Gasparin; Vitor Mattos; Bruno Barbizan; Fabio Saltara; Paulo Mello; Daniel Dezan; Jurandir Yanagihara.
Journal: Structural and Multidisciplinary Optimization (2021) – JCR 2021 = 4.279
Status: Published.

- **Title:** Low-Cost Identification of Two-Factor Interactions Through Fractional Factorial Method Applied to 1D Model of a s-CO2 Centrifugal Compressor
Authors: Elóy Gasparin; Gabriel Silva; Daniel Dezan; Paulo Mello; Fábio Saltara; Jurandir Yanagihara; Leandro Salviano.
Conference: Brazilian Congress of Thermal Sciences and Engineering - ENCIT (2022)
Status: Published.

- **Title:** Sensitivity Analysis Based on Morris Screening Method for Blade Design of a Centrifugal Compressor
Authors: Vitor Mattos; Elóy Gasparin; Paulo Mello; Fábio Saltara; Daniel Dezan; Jurandir Yanagihara; Leandro Salviano.
Conference: Ibero-Latin American Congress on Computational Methods in Engineering - CILAMCE (2019)
Status: Published.

- **Title:** Improved Preliminary Geometry for SCO2 Centrifugal Compressors Through Full 1D Modelling
Authors: Gustavo Gonçalves; Elóy Gasparin; Vitor Mattos; Paulo Mello; Fábio Saltara; Daniel Dezan; Jurandir Yanagihara; Leandro Salviano.
Conference: International Congress of Mechanical Engineering - COBEM (2021)
Status: Published.

- **Title:** Parametric optimization applied to design a high-performance vaneless-diffuser for CO2 centrifugal compressor
Authors: Vitor Mattos; Elóy Gasparin; Fabio Saltara; Paulo Mello; Daniel Dezan; Jurandir Yanagihara; Leandro Salviano.
Journal: Energy Sources, Part A: Recovery, Utilization, and Environmental Effects – JCR 2021 = 2.902
Status: First Review in Progress.